ATOMIC WEAPONS RESEARCH ESTABLISHMENT

AWRE REPORT NO. 010/86

P Seismograms Recorded at Eskdalemuir, Scotland from Explosions in Nevada, USA

N S Lyman
A Douglas
P D Marshall
J B Young

Approved for issue by

B L Elphick, Head of Division

ISBN 0 85518174 5

CONTENTS

SUMMARY

The report presents the P seismograms recorded at the array station at Eskdalemuir (EKA) Scotland from 39 Nevada explosions. Of the 39 explosions, 38 were fired at the Nevada Test Site and one (FAULTLESS) at Hot Creek Valley, Nevada. Five types of seismogram are shown for each explosion: the short-period (SP) array sum; the SP seismogram corrected for anelastic attenuation using a t* (ratio of travel time to specific quality factor, Q) of 0.2 s; the broad band (BB) P seismogram; and BB seismogram corrected for attenuation using t* values of 0.2 s and 0.35 s. By correcting for a t* of 0.2 s and comparing the resulting seismograms with the uncorrected it is possible to study the effects of the increased attenuation on paths out of Nevada relative to paths out of E Kazakh. The seismograms corrected using a t* of 0.35 s are assumed to be fully corrected for the effects of anelastic attenuation on the Nevada-EKA path.

For each explosion, estimates are given of the body-wave magnitudes and the rise times of the initial P pulse both before and after correction for attenuation, the pP-P times, and $\Psi^{c}(\infty)$, where $\Psi^{c}(\infty)$ is the long term level of the reduced displacement potential; all these estimates being derived from the EKA seismograms. Plotting $\Psi^{c}(\infty)$ (for the few explosions for which the yield has been published) against yield suggests that $\Psi^{c}(\infty)$ may be a better estimator of yield than body wave magnitude. The rise times measured on the BB seismograms when fully corrected for the effects of attenuation should be an estimate of the source rise time. Using magnitude as a measure of yield the results obtained here show that the rise times are roughly proportional to the cube root of the yield which is in agreement with simple theory. As in many other studies most of the estimated pP-P times are larger than predicted from the depth of firing of the explosion and the measured P-wave speed in the overburden.

Many of the BB seismograms show a P pulse, an apparent pP and a third arrival of significant amplitude (A_s) following immediately after pP. The A_s arrival is equivalent to that which others attribute to the effects of spalling at the free surface. Some of the seismograms also show arrivals of significant amplitude in the coda which are interpreted as the signals from aftershocks triggered by the explosion.

1. INTRODUCTION

Gibbs and Blamey (1) and Marshall (2) show short-period (SP) seismograms of the P waves from Nevada Test Site (NTS) explosions recorded at the array station at Eskdalemuir (EKA) Scotland. As well as the SP seismograms Marshall (2) shows the deconvolved records derived by removing some of the filtering effects of the SP recording systems and compensating for losses due to anelastic attenuation on the NTS-EKA path. In correcting for the effects of anelasticity it is necessary to assume a value for t*, where t* is the ratio of the travel time to the average quality factor on the path between source and receiver. Marshall (2) uses a value of t* of 1.0 s. Since Marshall's (2) work was published, evidence has accumulated that t* for many paths through the earth is significantly less than 1.0 s (for estimates of t* from NTS to Europe see Frasier and Filson (3) and Douglas (4)) so that in deconvolving the NTS seismograms Marshall (2) has probably overcorrected for the effects of anelasticity. In this report we present both the SP P seismograms recorded at EKA and the deconvolved seismograms for 39 Nevada explosions including the explosions studied by Gibbs and Blamey (1) and Marshall (2). The deconvolved seismograms were derived using a maximum value of t* of 0.35 s. Of the 39 explosions, 38 were fired at the NTS and one (FAULTLESS) in Hot Creek Valley (HCV) Nevada. Figure 1 shows maps of the NTS with the epicentres of the 38 explosions at this site. The NTS explosions form two main groups; those fired beneath Yucca Flats and those fired beneath Pahute Mesa. One NTS explosion does not fit into these groups, that is PILE DRIVER which was fired in a granite stock to the north of Yucca Flats. Most of the Yucca Flats and Pahute Mesa explosions were fired in tuff. Table 1 gives the distances and azimuths between the explosion sites and EKA. Table 2 lists hypocentre and other information for the explosions.

Ideally many of the results presented in this report would be displayed plotted against explosion yield. However, the yield has been published for only a very small number of the explosions studied (see table 2) so for some of the graphs the maximum-likelihood estimate of the body wave magnitude (m_b^{ML}) is used as a measure of the explosion size. The data used for the estimation of m_b^{ML} is from the Bulletin of the International Seismological Centre and the method of estimation is described by Marshall, Lilwall and Farthing (5). The m_b^{ML} estimates (table 2) should be a more consistent measure of magnitude than the standard m_b because station corrections are applied and allowance is made for the detection threshold of the stations.

The purpose of the report is: (i) to provide a catalogue of EKA seismograms from explosions in Nevada; and (ii) to demonstrate the advantages of deconvolved seismograms over SP P seismograms.

2. PROCESSING METHODS

All the seismograms presented in this report are array sums: the individual SP channels have been time shifted to correct for the differences in the arrival time of the signals at each seismometer of the array and the shifted channels added together. (The layout of the array is shown in figure 2). The deconvolved seismograms are derived from the array sums. To remove most of the filtering effects of the SP recording instrument an estimate is made of the seismogram as it would have been recorded on a broad band (BB) instrument that has constant magnification from about 0.05 Hz to about 10 Hz. The BB seismograms are obtained by passing the SP seismograms through a filter with a response as a function of frequency (ω) of $|a_2(\omega)|/a_1(\omega)$ where $a_1(\omega)$ is the instrument response of the SP instrument and $a_2(\omega)$ the response of the BB instrument. The amplitude spectra of $a_2(\omega)$ and $a_1(\omega)$ are shown in figure 3. By using $|a_2(\omega)|$ rather than $a_2(\omega)$ in converting to the BB instrument, phase shifts due to the recording system are removed - the seismogram produced is effectively that which would have been recorded with a "phaseless" seismograph. Such seismograms cannot be produced in real time - the impulse response of $|a_2(\omega)|/a_1(\omega)$ is non-causal - they can only be produced with recorded data. The main advantage of such phaseless seismograms is that they show source pulses with less instrument distortion than standard seismograms (see Stewart and Douglas (6) for further discussion).

Usually the principal effect of widening the pass band from SP to BB is to amplify the low-frequency noise (both system and seismic noise) so that the signal-to-noise ratio is much reduced compared to that on the SP seismogram. Very-low-frequency noise can be removed without significant distortion to the signal by simple high-pass filtering. High frequency noise can also be a problem particularly on the BB seismograms corrected for attenuation. All the BB seismograms have therefore been filtered with a low pass filter cutting-off at 4.5 Hz. To suppress the noise at frequencies around the signal frequency we use Wiener frequency filtering (for further discussion see Douglas and Young (7)). The filters are designed using the noise amplitude spectrum measured ahead of the onset of the signal and a theoretical signal spectrum derived by making some simple assumptions. Applying these filters gives a least squares estimate of the BB ground displacement.

To apply corrections for the effect of anelastic attenuation (given a value of t*) the seismograms are passed through a filter with a response $\{b(\omega)\}^{-1}$, where $b(\omega)$ is the response as a function of frequency of an attenuation operator. In this report we use the attenuation operator of Carpenter (8), where $|b(\omega)|$ is $\exp(-\omega t^*/2)$ and the phase spectrum is specified using the theory of Futterman (9). We present here seismograms corrected for two values of t*: 0.2 s and 0.35 s. The reasons for using these values are given below.

There is much evidence that for paths out of NTS to long range t* is on average 0.2 s greater than on paths from the E Kazakh sites. This difference in attenuation implies that the average magnitude of an NTS explosion (with predominant frequency around 1 Hz) should be about 0.3 magnitude units (m u) less than that of an E Kazakh explosion of the same yield; assuming the coupling is the same for the two explosions. By correcting for a t* of 0.2 s and comparing the resulting seismograms with the uncorrected it is possible to study the effect of the increased attenuation on the paths out of NTS relative to those out of E Kazakh.

The seismograms corrected using a t* of 0.35 s are assumed to be fully corrected for the effects of anelastic attenuation; 0.35 s being the assumed absolute value for t* on the NTS-EKA path. Some evidence has been published that t* may be as large as 0.5 s (3, 4) but more recent studies (10, 11) suggest that this is probably an over estimate.

It is usual to define the source function of an explosion by the reduced displacement potential $\Psi(t)$. The radiated P pulse is then proportional to $d\Psi(t)/dt$. For t greater than a second or two $\Psi(t)$ rapidly approaches $\Psi(\infty)$ and this is usually assumed to be proportional to yield. An estimate of $\Psi(\infty)$ can be obtained from the BB seismograms corrected for attenuation by taking the area under the P pulse and multiplying by $\{2G(\Delta)\}^{-1}$, where $G(\Delta)$ allows for the loss of amplitude due to geometrical spreading of the wave front in propagating from the source to distance Δ. $G(\Delta)$ is given by Carpenter (12).

There are two main difficulties in estimating $\Psi(\infty)$ in this way. These are: (i) pP may interfere with direct P so that the complete pulse is not observed; and (ii) the presence of low frequency noise may introduce significant errors into the estimates. Here it is assumed that the separation time pP-P is so large that the effect of pP interference can be neglected. At large signal-to-noise ratios a horizontal line is drawn through the onset of the pulse and the area above this line of the (first) positive pulse is the area used to compute $\Psi(\infty)$. At low signal-to-noise ratios an attempt is made to allow for the effects of the noise by choosing by eye what seems to be the most suitable baseline. In fact here two estimates of $\Psi(\infty)$ are given (table 2) for each explosion: for the first a horizontal baseline is assumed, for the second a baseline is chosen that makes some allowance for the effects of the noise. The two estimates are referred to as $\Psi^o(\infty)$ and $\Psi^c(\infty)$ respectively.

3. RESULTS

Five types of seismogram are shown for each explosion: the SP array sum; the SP seismogram corrected for a t* of 0.2 s; the BB seismogram; and the BB seismograms corrected for attenuation using t*'s of 0.2 s and 0.35 s. (In what follows the BB seismogram corrected for attenuation using a t* of 0.35 s is referred to as the deconvolved BB seismogram). Figures 4 and 5 show the seismograms for FAULTLESS and PILE DRIVER respectively; figures 6 to 18 the seismograms for the Yucca Flats explosions and figures 19 to 42 those for the Pahute Mesa explosions. Figure 43 shows all the SP seismograms for the Yucca Flats explosions arranged in order of depth of firing and figure 44 those for the Pahute Mesa explosions. Figures 45 and 46 show the BB seismograms for the Yucca Flats and Pahute Mesa explosions again arranged in order of depth of firing.

The seismograms for each explosion are annotated to show the predicted arrival time of PcP, the amplitudes and periods measured to compute magnitudes and the area used to estimate $\Psi^c(\infty)$. The P phase and where observed the phases A_{pP}, A_s and A_q are marked: A_{pP} is the apparent p^P, A_s a possible arrival from the impact of the spall (slapdown) that is assumed to be observed sometimes a second or two after detonation (see Springer (13)); and A_q marks a possible arrival from an earthquake aftershock (of the type noted by Douglas (4) and Douglas et al (14)) in the coda of the P seismogram.

Body wave magnitudes measured from both the observed SP ($m_b{}^o$) and attenuation corrected SP seismograms ($m_b{}^c$) are listed in table 2. The amplitudes and periods used in computing the magnitudes are given in table 3. As expected the attenuation corrected magnitudes are significantly larger than the normal magnitudes. The differences range from 0.13 m u for KASSERI (T = 1.4 s) to 0.49 m u for PILE DRIVER (T = 0.6 s) illustrating how the attenuation effect varies with the predominant frequency of the signal. Note however, that the period of the attenuation corrected seismograms are little different from those of the uncorrected showing that the period of an SP signal is not sensitive to differences in t* of around 0.2 s. As in general the larger the yield the larger the magnitude and the larger the observed period then there should be a systematic decrease in the difference between $m_b{}^o$ and $m_b{}^c$ with increasing magnitude and this is in fact shown in figure 47 where $m_b{}^c$ is plotted against $m_b{}^o$. The change in $m_b{}^o$ - $m_b{}^c$ with magnitude also implies what is obvious from theoretical considerations that the slope of m_b- yield curves depends on the anelastic attenuation on the paths between the test site and the recording stations: the greater the attenuation the greater the slope.

Figure 48a shows the estimates of $\Psi^c(\infty)$ plotted against yield for the few explosions for which the yield has been published. Estimates of $\Psi^c(\infty)$ obtained by Douglas et al (15) for explosions at the Amchitka test sites are also shown for comparison. There is a clear correlation between $\Psi^c(\infty)$ and yield. Figure 48b shows the plot of $\log^A/T$ against yield for the same explosions as shown in figure 48a. (The epicentral distance of Amchitka Island from EKA is about 73.5^o that of the NTS about 71.5^o so the effect on $\log^A/T$ of differences in distance between the two test sites and EKA should be negligible). It is clear that the scatter in $\Psi^c(\infty)$ is much less than for $\log^A/T$, in particular the $\log^A/T$ values show a very large systematic bias in the NTS results relative to the Amchitka Island results which is not seen in the $\Psi^c(\infty)$ estimates. However, this is perhaps not a fair comparison of the relative merits of $\log^A/T$ and $\Psi^c(\infty)$ for estimating yield. The anelastic attenuation beneath NTS appears to be greater than beneath the Amchitka site and so corrections should be applied to the observed amplitudes to allow for these differences. The attraction of using $\Psi^c(\infty)$ is that it should be insensitive to differences in attenuation. Figure 49 shows the estimates of $\Psi^o(\infty)$ and $\Psi^c(\infty)$ plotted against the maximum likelihood magnitude for the explosions. There is a clear correlation between $\Psi(\infty)$ and magnitude.

Table 2 lists for each explosion the rise time of the initial P pulse as seen on the BB seismogram uncorrected for attenuation and on the deconvolved BB seismogram. For a positive pulse the rise time τ, is defined following Gladwin and Stacey (16) as $u_{max}/(du/dt)_{max}$ where u_{max} is the maximum height of the pulse and $(du/dt)_{max}$ is the maximum gradient of its leading edge. The rise time after correction for attenuation (τ_c) should be an estimate of the rise times of the source pulses. Simple theoretical models of the explosion source predict that rise times will be proportional to $W^{1/3}$, where W is the yield. Taking m_b^{ML} (table 2) as a measure of log W it can be seen from figure 50 that $\log \tau_c$ does vary roughly linearly with log W and that the slope is around 1/3. In fact the variation in $\log \tau_c$ predicted by Haskell (17) for explosions in tuff is in rough agreement with the observed variation. The widely accepted Mueller and Murphy (18) model of the explosion source on the other hand predicts both shorter rise times and a slower variation with yield than shown by the observed times presented here. However, because the BB seismograms have been low-pass filtered the estimated rise time will in general be larger than the true value. Also because the seismograms are digitised at 20 samples/s there is obviously a lower limit to the estimated rise time of 0.05 s. But most of the observed rise times are 0.2 s or greater so the effect of these measurement errors is perhaps not important. There do, however, seem to be factors other than yield influencing the rise time - possibly rock type, rock strength and water content. GREELEY for example has a lower yield than HANDLEY but has a longer rise time. That there are differences in the rise times of the two explosions is evident even from the SP seismogram, particularly the seismogram corrected for t*, (see figures 20 and 27) where the first motion of HANDLEY is relatively larger than for GREELEY.

As can be seen from table 2 the effect on the rise time of correcting for attenuation varies from explosion to explosion; in general applying the correction produces a reduction in rise time but the amount by which the rise time changes varies with m_b (and hence presumably yield) and pulse shape.

The changes in rise time can be roughly understood using the results of Stewart (19). By convolving an attenuation operator with some simple pulse shapes Stewart (17) shows how the rise time of the pulse varies with t*. Thus for impulse-like pulses with initial rise times of τ_0, the rise time is proportional to 0.5 t* provided t* > 2 τ_0. For t* less than τ_0 the rise time initially decreases slightly and then increases with t*. Similarly for step-like pulses (with initial rise time τ_0) the rise time of the step is proportional to 1.7 t* provided t* > τ_0/1.7. For values of t* < τ_0/1.7 the rise time again decreases slightly before increasing.

The rise times presented here show that the effects of applying the attenuation correction are roughly consistent with what is expected from the results of Stewart (19). Thus consider PILE DRIVER which has an impulse-like source with an estimated initial rise time of 0.18 s. On a path with t* = 0.35 s ($\simeq$ 2 τ_0) the differences between initial and observed rise time should not differ greatly - which is in fact observed. For CHIBERTA which has a step-like P pulse and an initial rise time of 0.28 s then on a path with t* = 0.35 s the rise time should be somewhat less than 0.60 s (= 1.7 t*); the measured value is in fact 0.48 s. At magnitudes of m_b6.0 and greater where the initial rise times are around 0.45 s little difference is expected between the rise time before and after correction for attenuation and again this is seen. For FONTINA for example, correction for attenuation only reduces the rise times from 0.48 to 0.45 s and the explosion MUENSTER does in fact show a rise time that increases in applying the correction for attenuation (changing from 0.43 to 0.48 s) - an effect predicted by the results of Stewart (19).

For PILE DRIVER the BB seismogram after correction for a t* of 0.35 s shows apparently P and pP clearly separated. Taking A_{pP} (figure 5) as pP gives a pP-P time of about 0.7 s. However, the predicted pP-P time is about 0.2 s (table 2) and the measured time from the shot point to the free surface is 0.12 s (Springer (13)) which implies a pP-P time of 0.24 s. It is a common feature of explosion seismograms that what appears to be the pP-P time is longer than predicted. No satisfactory explanation of this has yet been given and this problem will be considered elsewhere. Some of the explosions other than PILE DRIVER also seem to show a clear onset to pP but again these onsets tend to be later than predicted. If it is assumed that P and pP pulses have the same shape and do not interfere signicantly then the pP-P time can be measured in a consistent manner from the deconvolved BB seismograms by taking the time difference between the first peak and the first trough. Table 2 lists these time differences and also the predicted time calculated from the depth of firing and the wave speed in the overburden. Figure 51 shows the measured times plotted against the predicted time. There is a weak correlation between the two but on average the measured times seem to be about 0.2 s greater than predicted.

Inspection of the seismograms from the Yucca Flats explosions shows that they roughly fall into three groups. One group consists of CREWLINE, LOWBALL, HEARTS and KEELSON. The deconvolved BB seismograms for these explosions show a sharp front for P and a sharp trailing edge to A_{pP} which merges into a prominent A_s phase. On the SP seismogram the two sharp positive-going deflections seen on the BB produce two nearly identical wavelets of the same polarity rather than the two wavelets (P and pP) of opposite polarity that would be expected from an explosion. On these seismograms it is P and A_s that control the form of the SP seismogram.

The second group consists of the seismograms from the three explosions MIZZEN, FARALLONES and ATRISCO. The SP seismograms from these explosions have their largest amplitudes in the first wavelet (first 1½ cycles) whereas all the other Yucca Flats seismograms have their largest amplitudes in the second wavelet. The most characteristic feature of the BB seismograms from this group is the absence of a prominent A_s phase.

The remaining explosions at the Yucca Flats (BILBY, COMMODORE, TOPGALLANT, CHIBERTA, STRAIT and MARSILLY) make up the third group. The deconvolved BB seismograms for this group show little or no A_s. Further, P tends to be a broader pulse than A_{pP}. On the SP seismograms the step-like form of the leading edge of P produces a smaller amplitude wavelet than the more impulse like A_{pP} thus giving the SP seismograms their characteristic shape.

No attempt is made here to account for the differences in seismogram shape shown by the different explosion groups. There is some correlation of shape with depth. Thus the first group all have depths of 640 m or less. The third group have depths of 690 m or more and the second group have depths that very nearly (637 to 668 m) lie between 640 and 690 m. So depth may be an important feature controlling the form of the radiated pulses and hence of the observed seismograms. However, the division into three groups is not as clear cut as suggested here, so for example, the BILBY explosion here classed as group 3 has seismograms that show similarities to those of the explosions in group 1 and the MIZZEN explosion here classed in group 2 has seismograms that are similar to those of the explosions in group 3.

Turning to the Pahute Mesa explosions it can be seen that most of the BB seismograms show a prominent A_s arrival. On the SP seismograms A_s extends the initial large amplitude arrivals up to 2½ cycles. Where A_s is completely absent and the trailing edge of A_{pP} is less steep than the leading edge - which for the explosions studied here is only true for PIPKIN - the initial P wavelet shows only about 1½ cycles. Note that for the explosion SLED A_s (and A_{pP}) are much larger than P.

Several of the explosions show evidence of possible earthquake aftershocks (A_q) contributing to the coda of P seismograms. Douglas (4) discusses the evidence for interpreting arrivals in the coda of the EKA seismograms of the GREELEY explosion as aftershocks and Douglas et al (14) report evidence of similar arrivals from aftershocks in the EKA seismograms of several other explosions, (BENHAM, BOXCAR and CAMEMBERT in particular). Other Pahute Mesa seismograms that clearly show possible aftershocks include MAST and KASSERI (figures 31 and 33 respectively). The most prominent example of possible aftershocks is shown for the explosion PURSE where the coda shows a sinusoidal arrival lasting about 10 s and having a maximum amplitude almost as large as the amplitude of the P arrival from the explosion. Of the Yucca Flats explosions considered here only the seismograms from the explosion BILBY show a clear arrival that might be from an earthquake aftershock (A_q, figure 6) although the CREWLINE and LOWBALL seismograms show possible arrivals at about the same time after onset. Note that the FAULTLESS seismograms also show evidence of possible arrivals from earthquake aftershocks.

The principal reason for attributing the A_q arrivals to earthquake aftershocks is that they (the arrivals) have relatively more high frequency energy than the initial P and A_{pP} arrivals from the explosion which shows that the A_q arrivals are not generated simply by reflection and refraction of explosion source pulses. That the A_q arrivals have relatively more high frequency than the initial pulses in the seismogram can be seen by comparing the relative amplitudes of P and A_q seen on the SP seismogram corrected for attenuation (on which the high frequencies are enhanced relative to the low) with that seen on the BB seismograms - the A_q arrivals are as expected largest relative to P on the SP seismogram (see for example the BOXCAR seismogram, figure 22). Note that as Douglas et al (14) point out, some of the seismograms show pairs of arrivals that appear to be of opposite polarity (for example see the seismograms for BOXCAR (figure 22) and KASSERI (figure 33)) which suggest they are P and pP from earthquakes at depths of a few kilometres.

Here arrivals from possible aftershocks in the coda of the explosion are identified as such because they contain relatively more high frequency energy than the first P arrival. One or two of the seismograms presented show evidence of possible low frequency arrivals in the coda. The seismograms from the explosion FARALLONES for example (figure 15), show a low frequency arrival A_{LF} which looks as though it is not simply low frequency noise but is part of the body wave seismogram. To decide on the origin of A_{LF} and similar arrivals requires further study but the possibility cannot be ruled out that some of the low frequency arrivals as well as the high frequency arrivals in the coda of the seismograms are due to aftershocks triggered by the explosion.

There is of course always the possibility that the large coda amplitudes are not associated with the explosion and it is only fortuitous that they arrive just after the P signal from the explosion. A study of signals from other stations needs to be made to check that the large amplitude arrivals in the coda of the seismogram from the explosion such as that seen from the explosion PURSE are from sources with epicentres close to the explosion epicentre. Note that the large amplitude arrivals in the coda of the seismogram from the explosion CHESHIRE are from an earthquake unassociated with the explosion - in this particular example the earthquake has an epicentre in the Philippines.

The core reflection PcP is predicted to arrive at around 20 s after onset of the seismograms presented here. Examination of the seismograms shows that the observed amplitudes of PcP relative to P is very variable and for many of the seismograms it is difficult to identify confidently any PcP phase. The best examples of PcP are shown on the seismograms from the FAULTLESS (figure 4), FARALLONES (figure 15) and ESTUARY (figure 38) explosions. Where PcP appears to be clearly seen (eg, figures 15 and 38) the observed onset seems to be about 0.7 s ahead of the predicted arrival time. Note that the seismograms for both FAULTLESS and FARALLONES show evidence of possible arrivals from aftershocks following P. Similar arrivals are seen following PcP suggesting these may be PcP from the aftershocks.

4. ACKNOWLEDGMENTS

We wish to thank the staff at the Eskdalemuir array for their conscientious work over many years, which has produced a large library of high quality recordings from which the seismograms presented here are taken.

REFERENCES

1. P G Gibbs and C Blamey: "Some Seismic Results of 12 Underground Nuclear Explosions at the Nevada Test Site, USA". AWRE Report 032/72 (1972)

2. P D Marshall: "Some Seismic Results from a World Wide Sample of Large Underground Explosions". AWRE Report 049/72 (1972)

3. C W Frasier and J Filson: "A Direct Measurement of the Earths Short-Period Attenuation ALong a Teleseismic Ray Path". J Geophys Res, 77, 3782-3787 (1972)

4. A Douglas: "Teleseismic Observations of Aftershocks Immediately Following an Underground Explosion". Geophys J R Astr Soc, 77, 503-515 (1984)

5. P D Marshall, R C Lilwall and J Farthing: "Body Wave Magnitudes and Locations of Underground Nuclear Explosions at the Nevada Test Site". AWRE Report 021/86 (1986) (to be issued)

6. R C Stewart and A Douglas: "Seismograms from Phaseless Seismographs". Geophys J R Astr Soc, 72, 517-521 (1983)

7. A Douglas and J B Young: "The Estimation of Seismic Body Wave Signals in the Presence of Oceanic Microseisms". AWRE Report 014/81 (1981)

8. E W Carpenter: "Absorption of Elastic Waves - An Operator for a Constant Q Mechanism". AWRE Report 043/66 (1966)

9. W I Futterman: "Dispersive Body Waves". J Geophys Res, 67, 5279-5291 (1962)

10. T Lay and D V Helmberger: "Body Wave Amplitude Patterns and Upper Mantle Attenuation Variations Across North America". Geophys J R Astr Soc, 66, 691-726 (1981)

11. Z A Der, T McElfresh, R Wagner and J Burnetti: "Spectral Characteristics of P Waves from Nuclear Explosions and Yield Estimation". Bull Seism Soc Am, 75, 379-390 (1985) and "Errata". Bull Seism Soc Am, 75, 1222

12. E W Carpenter: "A Quantitative Evaluation of Teleseismic Explosion Records". Proc Roy Soc A, 290, 396-407 (1966)

13. D L Springer: "Secondary Sources of Seismic Waves from Underground Nuclear Explosions". Bull Seism Soc Am, 64, 581-594 (1974)

14. A Douglas, J B Young and N S Lyman: "Comments on a Paper and a Reply to a Note by T C Wallace, D V Helmberger and T Lay". Bull Seism Soc Am, 76, 305-311 (1986)

15. A Douglas, P D Marshall and J B Young: "The P Waves from the Amchitka Island Explosions". Geophys J R Astr Soc (submitted)

16. M T Gladwin and F D Stacey: "Anelastic Degradation of Acoustic Pulses in Rock:. Phys Earth Planet Int, 8, 332-336 (1974)

17. N A Haskell: "Analytical Approximation for the Elastic Radiation from a Contained Underground Explosion". J Geophys Res, 72, 2583-2587 (1967)

18. R A Mueller and J R Murphy: "Seismic Characteristics of Underground Nuclear Detonations: Part I Seismic Spectrum Scaling:. Bull Seism Soc Am, 61, 1675-1692 (1971)

19. R C Stewart: "Q and the Rise and Fall of a Seismic Pulse". Geophys J R Astr Soc, 76, 793-805 (1984)

20. US Department of Energy: "Announced United States Nuclear Tests: July 1945 through December 1984". Report NVO-209 (Rev 5). Office of Public Affairs, US Department of Energy, Nevada Operations Office, US Department of Energy, Nevada Operations Office (1985)

21. R R Blandford, M F Tillman and D P Racine: "Empirical m_b:M_s Relations at the Nevada Test with Applications to m_b-Yield Relations". Report SDAC-TR-76-14, Teledyne Geotech (1977)

22. D L Springer and R L Kinnaman: "Seismic Source Summary for US Underground Nuclear Explosions 1961-1970". Bull Seism Soc Am, 61, 1073-1098 (1971)

23. D L Springer and R L Kinnaman: "Seismic Source Summary for US Underground Nuclear Explosions 1971-1973". Bull Seism Soc Am, 65, 343-349 (1975)

24. D von Seggern and R Blandford: "Source Time Functions and Spectra for Underground Nuclear Explosions". Geophys J Astr Soc, 31, 83-97 (1972)

TABLE 1

Distances, Backbearings and Azimuths of Eskdalemuir from the Nevada Test Areas

Test Area	Latitude (°N)	Longitude (°N)	Dist(°)	BB(°)	Az(°)
Faultless	38.63	116.22	70.43	310.1	33.9
Pile Driver	37.23	116.06	71.52	309.2	33.7
Pahute Mesa (Kasseri epicentre)	37.29	116.41	71.63	309.5	33.6
Yucca Flat (Crewline epicentre)	37.10	116.04	71.62	309.1	33.7

TABLE 2

Hypocentres, Magnitudes and Other Data for the Nevada Explosions

Code	Date	Name	Lat N°	Long W°	Depth (m)	Origin Time	m_b	m_b^{ML}	M_s	m_b^o	m_b^c	$\psi^o(\infty)$	$\psi^c(\infty)$	Yield #1	Firing Medium#2	Apparent pP-P time (s)	Predicted pP-P time#3 (s)	P wave speed in over-burden#4 (km/s)	Rise time obs. (s)	Rise time corr. (s)
HCV	19.01.68	FAULTLESS	38.63	116.22	975	18.15	6.3	6.43	4.88	6.22	6.38	4.7 E4	3.9 E4	200-1000	Tuff	0.7	0.71(0.80)	2.75	0.45	0.47
GS1	02.06.66	PILE DRIVER	37.23	116.06	463	15.30	5.6	5.56	3.86	5.13	5.62	3.0 E3	3.0 E3	62	Granite	0.7	0.17	5.5	0.24	0.18
YF1	13.09.63	BILBY	37.06	116.02	714	17.00	(5.45)	N/A	4.25	5.58	5.92	1.8 E4	1.4 E4	249	Tuff	1.20	0.84	1.7	0.35	0.26
YF2	20.05.67	COMMODORE	37.13	116.06	746	15.00	5.8	5.81	4.34	5.31	5.68	1.1 E4	1.1 E4	250	Tuff	1.10	0.88(0.84)	1.7	0.41	0.22
YF3	28.02.75	TOPGALLANT	37.11	116.06	713	15.15	5.6	5.69	4.15	5.24	5.64	1.4 E4	1.0 E4	20-200		1.10	0.86	1.65	0.38	0.27
YF4	03.06.75	MIZZEN	37.09	116.04	637	14.40	5.6	5.64	4.29	5.28	5.54	1.3 E4	8.4 E3	20-200		0.95	0.85	1.5	0.43	0.24
YF5	20.12.75	CHIBERTA	37.13	116.06	716	20.00	5.6	5.69	4.42	5.18	5.53	1.6 E4	1.1 E4	20-200		1.15	0.80	1.8	0.47	0.30
YF6	04.02.76	KEELSON	37.07	116.03	640	14.20	5.6	5.66	4.20	5.10	5.37	3.1 E3	3.1 E3	20-200		1.05	0.75	1.7	0.33	0.25
YF7	17.03.76	STRAIT	37.11	116.05	780	14.45	5.8	5.87	4.47	5.47	5.74	3.8 E4	2.6 E4	200-500		1.05	0.92	1.69	0.51	0.29
YF8	05.04.77	MARSILLY	37.12	116.06	690	15.00	5.6	5.71		5.12	5.45	1.2 E4	8.9 E3	20-150		1.10	0.81	1.7	0.43	0.22
YF9	25.05.77	CREWLINE	37.10	116.04	564	17.00	5.3	5.36		4.87	5.23	2.3 E3	2.3 E3	20-150		0.85	0.66	1.7	0.33	0.13
YF10	14.12.77	FARALLONES	37.14	116.09	668	15.30	5.7	5.77		5.36	5.63	1.3 E4	9.2 E3	20-150		1.05	0.79	1.7	0.42	0.19
YF11	12.07.78	LOWBALL	37.08	116.04	564	17.00	5.6	5.67		5.17	5.49	6.1 E3	5.0 E3	20-150		1.05	0.66	1.7	0.36	0.22
YF12	06.09.79	HEARTS	37.09	116.05	640	15.00	5.8	5.88		4.89	5.19	3.1 E3	2.8 E3	20-150		1.05	0.75	1.7	0.35	0.22
YF13	05.08.82	ATRISCO	37.08	116.01	640	14.00	5.7	N/A		5.39	5.69	2.0 E4	1.2 E4	20-150		1.15	0.75	1.7	0.35	0.28
PM1	30.06.66	HALFBEAK	37.32	116.30	819	22.15	6.1	6.02	4.66	5.79	6.05	1.7 E4	1.7 E4	365	Rhyolite	0.75	0.50(0.72)	3.3	0.44	0.25
PM2	20.12.66	GREELEY	37.30	116.41	1215	15.30	6.3	6.18	5.09	5.92	6.08	3.0 E4	3.0 E4	870	Tuff	0.85	0.84(0.97)	2.9	0.50	0.40
PM3	23.05.67	SCOTCH	37.28	116.37	978	14.00	5.7	5.59	4.45	5.23	5.52	3.2 E3	4.4 E3	155	Tuff	0.90	0.67(0.91)	2.9	0.29	0.18
PM4	26.04.68	BOXCAR	37.30	116.46	1158	15.00	6.2	6.27	5.21	6.02	6.26	5.6 E4	5.6 E4	1300	Rhyolite	1.00	0.80(0.96)	2.9	0.48	0.32
PM5	29.08.68	SLED	37.25	116.35	729	22.45	5.9	5.84	4.45	5.92	6.21	1.2 E4	1.2 E4	20-300	Tuff	0.75	0.50	2.9	0.32	0.17
PM6	19.12.68	BENHAM	37.23	116.47	1402	16.30	6.3	6.30	5.24	6.27	6.46	5.4 E4	5.4 E4	1150	Tuff	0.80	0.97	2.9	0.50	0.38
PM7	07.05.69	PURSE	37.28	116.50	599	13.45	5.5	5.66	4.74	5.50	5.70	9.2 E3	7.1 E3	20-200	Tuff	0.80	0.41	2.9	0.49	0.23
PM8	08.10.69	PIPKIN	37.26	116.44	617	14.30	5.6	5.46	4.20	5.56	5.79	8.3 E3	7.5 E3	200-1000	Tuff/Rhyo.	0.55	0.43	2.9	0.45	0.30
PM9	26.03.70	HANDLEY	37.30	116.53	1206	19.00	6.4	6.33	5.37	6.07	6.32	6.0 E4	4.9 E4	>1Mt	Tuff	0.85	0.83(0.95)	2.9	0.51	0.31
PM10	06.06.73	ALMENDRO	37.25	116.35	1064	13.00	6.1	6.16	4.88	5.93	6.16	3.8 E4	3.6 E4	200-1000	Tuff/Rhyo.	0.90	0.69	3.1	0.52	0.34
PM11	14.05.75	TYBO	37.22	116.47	765	14.00	5.9	6.05	4.70	5.82	6.03	1.7 E4	1.7 E4	200-1000		0.70	0.67	2.3	0.46	0.37
PM12	03.06.75	STILTON	37.34	116.52	731	14.20	5.8	5.82	4.46	5.49	5.80	1.3 E4	7.9 E3	20-200		0.70	0.68	2.15	0.39	0.24
PM13	19.06.75	MAST	37.35	116.32	912	13.00	5.9	6.05	4.80	5.91	6.09	2.0 E4	1.6 E4	200-1000		0.60	0.47	3.9	0.44	0.31
PM14	26.06.75	CAMEMBERT	37.28	116.37	1311	12.30	6.1	6.20	4.98	5.98	6.20	4.5 E4	3.6 E4	200-1000		0.95	0.90	2.9	0.50	0.37
PM15	28.10.75	KASSERI	37.29	116.41	1265	14.30	6.2	6.30	5.25	6.14	6.27	5.1 E4	5.1 E4	200-1000		1.05	0.83	3.04	0.49	0.45
PM16	20.11.75	INLET	37.22	116.37	817	15.00	5.9	5.96	4.64	5.70	5.97	1.5 E4	1.2 E4	200-1000		1.05	0.54	3.04	0.45	0.20
PM17	03.01.76	MUENSTER	37.30	116.33	1451	19.15	6.2	6.28	5.17	5.99	6.18	3.5 E4	2.4 E4	200-1000		0.80	1.00	2.9	0.44	0.45
PM18	12.02.76	FONTINA	37.27	116.49	1219	14.45	6.1	6.24	5.37	5.93	6.12	5.5 E4	4.0 E4	200-1000		0.95	0.84	2.9	0.50	0.44
PM19	14.02.76	CHESHIRE	37.24	116.42	1167	11.30	5.8	5.92	4.85	5.54	5.82	1.0 E4	1.0 E4	200-300		0.85	0.73	3.2	0.45	0.19
PM20	09.03.76	ESTUARY	37.31	116.36	869	14.00	5.8	5.97	4.87	5.68	5.84	2.1 E4	1.5 E4	200-500		0.85	0.65	2.66	0.53	0.32
PM21	14.03.76	COLBY	37.31	116.47	1273	12.30	6.2	6.34	5.23	5.93	6.21	7.0 E4	6.3 E4	500-1000		1.10	0.91	2.8	0.54	0.44
PM22	17.03.76	POOL	37.26	116.31	879	14.15	6.0	6.05	4.66	5.68	5.95	1.2 E4	1.2 E4	200-500		1.05	0.61	2.9	0.41	0.24
PM23	11.04.78	BACKBEACH	37.23	116.37	611	17.45	5.5	5.54		5.37	5.64	3.9 E3	3.9 E3	20-150		0.80	0.42	2.9	0.34	0.24
PM24	31.08.78	PANIR	37.28	116.36	681	14.00	5.6	5.66		5.52	5.75	1.0 E4	1.0 E4	20-150		0.70	0.47	2.9	0.47	0.26

#1 Yields are taken from [20].

#2 Information on the firing medium is taken from [22] and [23].

#3 Times in brackets are estimates of pP-P times obtained from very close in observations (see Springer [13]).

#4 Wave speeds are taken from [21].

TABLE 3

Amplitudes, Periods and Estimated Eskdalemuir Magnitudes for the Nevada Explosions

		$\frac{1}{2}$ pk/pk uncorrected	$\frac{1}{2}$ pk/pk corrected	Period	Log $^{A}/_{T}$	m_b	Difference
HCV	Faultless	147.5	273.2	1.3	2.32	6.22	0.16
		236.5	358.3	1.2	2.48	6.38	
GS1	Pile Driver	20.7	10.1	0.6	1.23	5.13	0.49
		64.7	31.6	0.6	1.72	5.62	
YF1	Bilby	52.5	43.4	0.9	1.68	5.58	0.34
		115.0	95.0	0.9	2.02	5.92	
YF2	Commodore	28.1	23.2	0.9	1.41	5.31	0.37
		65.2	53.9	0.9	1.78	5.68	
YF3	Topgallant	23.8	19.6	0.9	1.34	5.24	0.40
		59.6	49.2	0.9	1.74	5.64	
YF4	Mizzen	21.2	26.2	1.1	1.38	5.28	0.26
		43.8	43.8	1.0	1.64	5.54	
YF5	Chiberta	20.6	17.0	0.9	1.28	5.18	0.35
		46.0	38.0	0.9	1.63	5.53	
YF6	Keelson	17.3	14.3	0.9	1.20	5.10	0.27
		35.6	20.6	0.7	1.47	5.37	
YF7	Strait	39.1	32.3	0.9	1.56	5.46	0.28
		75.5	62.4	0.9	1.84	5.74	
YF8	Marsilly	18.1	14.9	0.9	1.22	5.12	0.33
		38.9	32.2	0.9	1.55	5.45	
YF9	Crewline	10.3	8.5	0.9	0.97	4.87	0.36
		25.3	17.3	0.8	1.33	5.23	
YF10	Farallones	25.5	31.5	1.1	1.46	5.36	0.27
		53.9	53.9	1.0	1.73	5.63	
YF11	Lowball	20.4	16.9	0.9	1.27	5.17	0.32
		42.4	35.0	0.9	1.59	5.49	
YF12	Hearts	10.7	8.8	0.9	0.99	4.89	0.30
		23.6	13.6	0.7	1.29	5.19	
YF13	Atrisco	34.0	28.1	0.9	1.49	5.39	0.30
		71.7	49.1	0.8	1.79	5.69	
PM1	Halfbeak	69.0	85.1	1.1	1.89	5.79	0.26
		125.4	154.8	1.1	2.15	6.05	
PM2	Greeley	73.7	136.5	1.3	2.02	5.92	0.16
		120.7	182.9	1.2	2.18	6.08	
PM3	Scotch	19.0	23.6	1.1	1.33	5.23	0.29
		37.4	46.2	1.1	1.62	5.52	
PM4	Boxcar	104.4	158.2	1.2	2.12	6.02	0.24
		202.0	249.3	1.1	2.36	6.26	
PM5	Sled	93.2	115.1	1.1	2.02	5.92	0.29
		184.0	227.1	1.1	2.31	6.21	
PM6	Benham	184.7	279.9	1.2	2.37	6.27	0.19
		320.1	395.1	1.1	2.56	6.46	
PM7	Purse	31.8	48.1	1.2	1.60	5.50	0.20
		56.4	69.6	1.1	1.80	5.70	
PM8	Pipkin	36.0	54.6	1.2	1.66	5.56	0.23
		68.5	84.5	1.1	1.89	5.79	
PM9	Handley	131.0	161.7	1.1	2.17	6.07	0.25
		262.5	262.5	1.0	2.42	6.32	

TABLE 3 (Cont'd)

		½ pk/pk uncorrected	½ pk/pk corrected	Period	Log $^{A}/T$	m_b	Difference
PM10	Almendro	84.4	127.9	1.2	2.03	5.93	0.21
		137.4	208.1	1.2	2.24	6.14	
PM11	Tybo	66.4	100.5	1.2	1.92	5.82	0.21
		121.4	149.9	1.1	2.13	6.03	
PM12	Stilton	33.1	40.8	1.1	1.57	5.49	0.31
		71.3	88.0	1.1	1.90	5.80	
PM13	Mast	81.0	122.7	1.2	2.01	5.91	0.18
		137.0	169.1	1.1	2.19	6.09	
PM14	Camembert	96.2	145.8	1.2	2.08	5.98	0.22
		157.6	238.8	1.2	2.30	6.20	
PM15	Kasseri	108.0	245.5	1.4	2.24	6.14	0.13
		165.5	306.5	1.3	2.37	6.27	
PM16	Inlet	56.4	69.6	1.1	1.80	5.70	0.27
		118.0	118.0	1.0	2.07	5.97	
PM17	Muenster	98.5	149.3	1.2	2.09	5.99	0.19
		170.4	210.4	1.1	2.28	6.18	
PM18	Fontina	76.1	140.8	1.3	2.03	5.93	0.19
		132.8	201.2	1.2	2.22	6.12	
PM19	Cheshire	38.9	48.0	1.1	1.64	5.54	0.28
		90.5	74.8	0.9	1.92	5.82	
PM20	Estuary	42.4	78.6	1.3	1.78	5.68	0.26
		69.6	105.5	1.2	1.94	5.84	
PM21	Colby	84.4	127.8	1.2	2.03	5.93	0.28
		161.6	244.8	1.2	2.31	6.21	
PM22	Pool	47.5	71.9	1.2	1.78	5.68	0.27
		99.1	122.3	1.1	2.05	5.95	
PM23	Backbeach	23.4	35.5	1.2	1.47	5.37	0.27
		49.1	60.7	1.1	1.74	5.64	
PM24	Panir	33.3	50.4	1.2	1.62	5.52	0.23
		63.6	78.6	1.1	1.85	5.75	

The first magnitude given for each explosion is computed directly from the short period array sum, the second magnitude is from the array sum corrected for some of the effects of anelastic attenuation with a t* of 0.2s. The last column of the table is the difference between the two magnitudes.

NOTES ON FIGURES

Figure 1. Maps showing epicentres of the Nevada Test Site explosions for which seismograms are given in this report.

Figure 2. Layout of the Eskdalemuir array. The intersection of the arms of the array is at 55° 19' 59" N, 3° 9' 33" W.

Figure 3. Amplitude response as a function of frequency of short-period and broad-band systems.

Figure 4. P seismograms recorded at Eskdalemuir, Scotland from NTS explosion FAULTLESS.

(a) Short-period seismogram (array sum)
(b) Seismogram (a) corrected for anelastic attenuation assuming t* = 0.2 s
(c) Broad-band seismogram
(d) Seismogram (c) corrected for anelastic attenuation assuming t* = 0.2 s
(e) Seismogram (c) corrected for anelastic attenuation assuming t* = 0.35 s (deconvolved seismogram).

A_{pP} is the apparent pP pulse. A_S the slap-down pulse. A_q marks possible arrivals from after shocks of the explosion. The arrival time shown for PcP is the predicted time. The amplitude scale shown for each trace is in nanometres. The SP amplitudes and periods used to compute the station magnitudes are also marked. Shading shows area used to estimate $\Psi^{c}(\infty)$.

Figure 5. P seismograms recorded at Eskdalemuir, Scotland from NTS explosion PILE DRIVER.

(a) Short-period seismogram (array sum)
(b) Seismogram (a) corrected for anelastic attenuation assuming t* = 0.2 s
(c) Broad-band seismogram
(d) Seismogram (c) corrected for anelastic attenuation assuming t* = 0.2 s
(e) Seismogram (c) corrected for anelastic attenuation assuming t* = 0.35 s (deconvolved seismogram).

A_{pP} is the apparent pP pulse. The arrival time shown for PcP is the predicted time. The amplitude scale shown for each trace is in nanometres. The SP amplitudes and periods used to compute the station magnitudes are also marked. Shading shows area used to estimate $\Psi^{c}(\infty)$.

Figure 6. P seismograms recorded at Eskdalemuir, Scotland from NTS explosion BILBY.

(a) Short-period seismogram (array sum)
(b) Seismogram (a) corrected for anelastic attenuation assuming $t* = 0.2$ s
(c) Broad-band seismogram
(d) Seismogram (c) corrected for anelastic attenuation assuming $t* = 0.2$ s
(e) Seismogram (c) corrected for anelastic attenuation assuming $t* = 0.35$ s (deconvolved seismogram).

A_{pP} is the apparent pP pulse. A_q marks possible arrivals from aftershocks of the explosion. The arrival time shown for PcP is the predicted time. The amplitude scale shown for each trace is in nanometres. The SP amplitudes and periods used to compute the station magnitudes are also marked. Shading shows area used to estimate $\Psi^c(\infty)$.

Figure 7. P seismograms recorded at Eskdalemuir, Scotland from NTS explosion COMMODORE.

(a) Short-period seismogram (array sum)
(b) Seismogram (a) corrected for anelastic attenuation assuming $t* = 0.2$ s
(c) Broad-band seismogram
(d) Seismogram (c) corrected for anelastic attenuation assuming $t* = 0.2$ s
(e) Seismogram (c) corrected for anelastic attenuation assuming $t* = 0.35$ s (deconvolved seismogram).

A_{pP} is the apparent pP pulse. The arrival time shown for PcP is the predicted time. The amplitude scale shown for each trace is in nanometres. The SP amplitudes and periods used to compute the station magnitudes are also marked. Shading shows area used to estimate $\Psi^c(\infty)$.

Figure 8. P seismograms recorded at Eskdalemuir, Scotland from NTS explosion TOPGALLANT.

(a) Short-period seismogram (array sum)
(b) Seismogram (a) corrected for anelastic attenuation assuming $t* = 0.2$ s
(c) Broad-band seismogram
(d) Seismogram (c) corrected for anelastic attenuation assuming $t* = 0.2$ s
(e) Seismogram (c) corrected for anelastic attenuation assuming $t* = 0.35$ s (deconvolved seismogram).

A_{pP} is the apparent pP pulse. The arrival time shown for PcP is the predicted time. The amplitude scale shown for each trace is in nanometres. The SP amplitudes and periods used to compute the station magnitudes are also marked. Shading shows area used to estimate $\Psi^c(\infty)$.

Figure 9. P seismograms recorded at Eskdalemuir, Scotland from NTS explosion MIZZEN.

(a) Short-period seismogram (array sum)
(b) Seismogram (a) corrected for anelastic attenuation assuming $t^* = 0.2$ s
(c) Broad-band seismogram
(d) Seismogram (c) corrected for anelastic attenuation assuming $t^* = 0.2$ s
(e) Seismogram (c) corrected for anelastic attenuation assuming $t^* = 0.35$ s (deconvolved seismogram).

A_{pP} is the apparent pP pulse. The arrival time shown for PcP is the predicted time. The amplitude scale shown for each trace is in nanometres. The SP amplitudes and periods used to compute the station magnitudes are also marked. Shading shows area used to estimate $\Psi^c(\infty)$.

Figure 10. P seismograms recorded at Eskdalemuir, Scotland from NTS explosion CHIBERTA.

(a) Short-period seismogram (array sum)
(b) Seismogram (a) corrected for anelastic attenuation assuming $t^* = 0.2$ s
(c) Broad-band seismogram
(d) Seismogram (c) corrected for anelastic attenuation assuming $t^* = 0.2$ s
(e) Seismogram (c) corrected for anelastic attenuation assuming $t^* = 0.35$ s (deconvolved seismogram).

A_{pP} is the apparent pP pulse. The arrival time shown for PcP is the predicted time. The amplitude scale shown for each trace is in nanometres. The SP amplitudes and periods used to compute the station magnitudes are also marked. Shading shows area used to estimate $\Psi^c(\infty)$.

Figure 11. P seismograms recorded at Eskdalemuir, Scotland from NTS explosion KEELSON.

(a) Short-period seismogram (array sum)
(b) Seismogram (a) corrected for anelastic attenuation assuming $t^* = 0.2$ s
(c) Broad-band seismogram
(d) Seismogram (c) corrected for anelastic attenuation assuming $t^* = 0.2$ s
(e) Seismogram (c) corrected for anelastic attenuation assuming $t^* = 0.35$ s (deconvolved seismogram).

A_{pP} is the apparent pP pulse. A_s the slap-down pulse. The arrival time shown for PcP is the predicted time. The amplitude scale shown for each trace is in nanometres. The SP amplitudes and periods used to compute the station magnitudes are also marked. Shading shows area used to estimate $\Psi^c(\infty)$.

Figure 12. P seismograms recorded at Eskdalemuir, Scotland from NTS explosion STRAIT.

(a) Short-period seismogram (array sum)
(b) Seismogram (a) corrected for anelastic attenuation assuming $t^* = 0.2$ s
(c) Broad-band seismogram
(d) Seismogram (c) corrected for anelastic attenuation assuming $t^* = 0.2$ s
(e) Seismogram (c) corrected for anelastic attenuation assuming $t^* = 0.35$ s (deconvolved seismogram).

A_{pP} is the apparent pP pulse. The arrival time shown for PcP is the predicted time. The amplitude scale shown for each trace is in nanometres. The SP amplitudes and periods used to compute the station magnitudes are also marked. Shading shows area used to estimate $\Psi^c(\infty)$.

Figure 13. P seismograms recorded at Eskdalemuir, Scotland from NTS explosion MARSILLY.

(a) Short-period seismogram (array sum)
(b) Seismogram (a) corrected for anelastic attenuation assuming $t^* = 0.2$ s
(c) Broad-band seismogram
(d) Seismogram (c) corrected for anelastic attenuation assuming $t^* = 0.2$ s
(e) Seismogram (c) corrected for anelastic attenuation assuming $t^* = 0.35$ s (deconvolved seismogram).

A_{pP} is the apparent pP pulse. The arrival time shown for PcP is the predicted time. The amplitude scale shown for each trace is in nanometres. The SP amplitudes and periods used to compute the station magnitudes are also marked. Shading shows area used to estimate $\Psi^c(\infty)$.

Figure 14. P seismograms recorded at Eskdalemuir, Scotland from NTS explosion CREWLINE.

(a) Short-period seismogram (array sum)
(b) Seismogram (a) corrected for anelastic attenuation assuming $t^* = 0.2$ s
(c) Broad-band seismogram
(d) Seismogram (c) corrected for anelastic attenuation assuming $t^* = 0.2$ s
(e) Seismogram (c) corrected for anelastic attenuation assuming $t^* = 0.35$ s (deconvolved seismogram).

A_{pP} is the apparent pP pulse. A_S the slap-down pulse. The arrival time shown for PcP is the predicted time. The amplitude scale shown for each trace is in nanometres. The SP amplitudes and periods used to compute the station magnitudes are also marked. Shading shows area used to estimate $\Psi^c(\infty)$.

Figure 15. P seismograms recorded at Eskdalemuir, Scotland from NTS explosion FARALLONES.

(a) Short-period seismogram (array sum)
(b) Seismogram (a) corrected for anelastic attenuation assuming $t^* = 0.2$ s
(c) Broad-band seismogram
(d) Seismogram (c) corrected for anelastic attenuation assuming $t^* = 0.2$ s
(e) Seismogram (c) corrected for anelastic attenuation assuming $t^* = 0.35$ s (deconvolved seismogram).

A_{pP} is the apparent pP pulse. A_{LF} is a possible low frequency arrival from an earthquake triggered by the explosion. The arrival time shown for PcP is the predicted time. Note that like P, PcP may be followed by low frequency arrivals from triggered earthquakes. The amplitude scale shown for each trace is in nanometres. The SP amplitude and periods used to compute the station magnitudes are also marked. Shading shows area used to estimate $\Psi^c(\infty)$.

Figure 16. P seismograms recorded at Eskdalemuir, Scotland from NTS explosion LOWBALL.

(a) Short-period seismogram (array sum)
(b) Seismogram (a) corrected for anelastic attenuation assuming $t^* = 0.2$ s
(c) Broad-band seismogram
(d) Seismogram (c) corrected for anelastic attenuation assuming $t^* = 0.2$ s
(e) Seismogram (c) corrected for anelastic attenuation assuming $t^* = 0.35$ s (deconvolved seismogram).

A_{pP} is the apparent pP pulse. A_S the slap-down pulse. The arrival time shown for PcP is the predicted time. The amplitude scale shown for each trace is in nanometres. The SP amplitudes and periods used to compute the station magnitudes are also marked. Shading shows area used to estimate $\Psi^c(\infty)$.

Figure 17. P seismograms recorded at Eskdalemuir, Scotland from NTS explosion HEARTS.

(a) Short-period seismogram (array sum)
(b) Seismogram (a) corrected for anelastic attenuation assuming $t^* = 0.2$ s
(c) Broad-band seismogram
(d) Seismogram (c) corrected for anelastic attenuation assuming $t^* = 0.2$ s
(e) Seismogram (c) corrected for anelastic attenuation assuming $t^* = 0.35$ s (deconvolved seismogram).

A_{pP} is the apparent pP pulse. A_S the slap-down pulse. The arrival time shown for PcP is the predicted time. The amplitude scale shown for each trace is in nanometres. The SP amplitudes and periods used to compute the station magnitudes are also marked. Shading shows area used to estimate $\Psi^c(\infty)$.

Figure 18. P seismograms recorded at Eskdalemuir, Scotland from NTS explosion ATRISCO.

(a) Short-period seismogram (array sum)
(b) Seismogram (a) corrected for anelastic attenuation assuming $t^* = 0.2$ s
(c) Broad-band seismogram
(d) Seismogram (c) corrected for anelastic attenuation assuming $t^* = 0.2$ s
(e) Seismogram (c) corrected for anelastic attenuation assuming $t^* = 0.35$ s (deconvolved seismogram).

A_{pP} is the apparent pP pulse. The arrival time shown for PcP is the predicted time. The amplitude scale shown for each trace is in nanometres. The SP amplitudes and periods used to compute the station magnitudes are also marked. Shading shows area used to estimate $\Psi^c(\infty)$.

Figure 19. P seismograms recorded at Eskdalemuir, Scotland from NTS explosion HALFBEAK.

(a) Short-period seismogram (array sum)
(b) Seismogram (a) corrected for anelastic attenuation assuming $t^* = 0.2$ s
(c) Broad-band seismogram
(d) Seismogram (c) corrected for anelastic attenuation assuming $t^* = 0.2$ s
(e) Seismogram (c) corrected for anelastic attenuation assuming $t^* = 0.35$ s (deconvolved seismogram).

A_{pP} is the apparent pP pulse. A_s the slap-down pulse. The arrival time shown for PcP is the predicted time. The amplitude scale shown for each trace is in nanometres. The SP amplitudes and periods used to compute the station magnitudes are also marked. Shading shows area used to estimate $\Psi^c(\infty)$.

Figure 20. P seismograms recorded at Eskdalemuir, Scotland from NTS explosion GREELEY.

(a) Short-period seismogram (array sum)
(b) Seismogram (a) corrected for anelastic attenuation assuming $t^* = 0.2$ s
(c) Broad-band seismogram
(d) Seismogram (c) corrected for anelastic attenuation assuming $t^* = 0.2$ s
(e) Seismogram (c) corrected for anelastic attenuation assuming $t^* = 0.35$ s (deconvolved seismogram).

A_{pP} is the apparent pP pulse. A_s the slap-down pulse. The arrival time shown for PcP is the predicted time. The amplitude scale shown for each trace is in nanometres. The SP amplitudes and periods used to compute the station magnitudes are also marked. Shading shows area used to estimate $\Psi^c(\infty)$.

Figure 21. P seismograms recorded at Eskdalemuir, Scotland from NTS explosion SCOTCH.

(a) Short-period seismogram (array sum)
(b) Seismogram (a) corrected for anelastic attenuation assuming $t^* = 0.2$ s
(c) Broad-band seismogram
(d) Seismogram (c) corrected for anelastic attenuation assuming $t^* = 0.2$ s
(e) Seismogram (c) corrected for anelastic attenuation assuming $t^* = 0.35$ s (deconvolved seismogram).

A_{pP} is the apparent pP pulse. A_S the slap-down pulse. The arrival time shown for PcP is the predicted time. The amplitude scale shown for each trace is in nanometres. The SP amplitudes and periods used to compute the station magnitudes are also marked. Shading shows area used to estimate $\Psi^C(\infty)$.

Figure 22. P seismograms recorded at Eskdalemuir, Scotland from NTS explosion BOXCAR.

(a) Short-period seismogram (array sum)
(b) Seismogram (a) corrected for anelastic attenuation assuming $t^* = 0.2$ s
(c) Broad-band seismogram
(d) Seismogram (c) corrected for anelastic attenuation assuming $t^* = 0.2$ s
(e) Seismogram (c) corrected for anelastic attenuation assuming $t^* = 0.35$ s (deconvolved seismogram).

A_{pP} is the apparent pP pulse. A_S the slap-down pulse. A_{q_1} and A_{q_2} appear to be of opposite polarity and thus may be P and pP respectively from an aftershock of the explosion. The arrival time shown for PcP is the predicted time. The amplitude scale shown for each trace is in nanometres. The SP amplitudes and periods used to compute the station magnitudes are also marked. Shading shows area used to estimate $\Psi^C(\infty)$.

Figure 23. P seismograms recorded at Eskdalemuir, Scotland from NTS explosion SLED.

(a) Short-period seismogram (array sum)
(b) Seismogram (a) corrected for anelastic attenuation assuming $t^* = 0.2$ s
(c) Broad-band seismogram
(d) Seismogram (c) corrected for anelastic attenuation assuming $t^* = 0.2$ s
(e) Seismogram (c) corrected for anelastic attenuation assuming $t^* = 0.35$ s (deconvolved seismogram).

A_{pP} is the apparent pP pulse. A_S the slap-down pulse. The arrival time shown for PcP is the predicted time. The amplitude scale shown for each trace is in nanometres. The SP amplitudes and periods used to compute the station magnitudes are also marked. Shading shows area used to estimate $\Psi^C(\infty)$.

Figure 24. P seismograms recorded at Eskdalemuir, Scotland from NTS explosion BENHAM.

(a) Short-period seismogram (array sum)
(b) Seismogram (a) corrected for anelastic attenuation assuming $t^* = 0.2$ s
(c) Broad-band seismogram
(d) Seismogram (c) corrected for anelastic attenuation assuming $t^* = 0.2$ s
(e) Seismogram (c) corrected for anelastic attenuation assuming $t^* = 0.35$ s (deconvolved seismogram).

A_{pP} is the apparent pP pulse. A_s the slap-down pulse. A_q marks possible arrivals from aftershocks of the explosion. The arrival time shown for PcP is the predicted time. The amplitude scale shown for each trace is in nanometres. The SP amplitudes and periods used to compute the station magnitudes are also marked. Shading shows area used to estimate $\Psi^c(\infty)$.

Figure 25. P seismograms recorded at Eskdalemuir, Scotland from NTS explosion PURSE.

(a) Short-period seismogram (array sum)
(b) Seismogram (a) corrected for anelastic attenuation assuming $t^* = 0.2$ s
(c) Broad-band seismogram
(d) Seismogram (c) corrected for anelastic attenuation assuming $t^* = 0.2$ s
(e) Seismogram (c) corrected for anelastic attenuation assuming $t^* = 0.35$ s (deconvolved seismogram).

A_{pP} is the apparent pP pulse. A_s the slap-down pulse. A_q marks possible arrivals from aftershocks of the explosion. The arrival time shown for PcP is the predicted time. The amplitude scale shown for each trace is in nanometres. The SP amplitudes and periods used to compute the station magnitudes are also marked. Shading shows area used to estimate $\Psi^c(\infty)$.

Figure 26. P seismograms recorded at Eskdalemuir, Scotland from NTS explosion PIPKIN.

(a) Short-period seismogram (array sum)
(b) Seismogram (a) corrected for anelastic attenuation assuming $t^* = 0.2$ s
(c) Broad-band seismogram
(d) Seismogram (c) corrected for anelastic attenuation assuming $t^* = 0.2$ s
(e) Seismogram (c) corrected for anelastic attenuation assuming $t^* = 0.35$ s (deconvolved seismogram).

A_{pP} is the apparent pP pulse. The arrival time shown for PcP is the predicted time. The amplitude scale shown for each trace is in nanometres. The SP amplitudes and periods used to compute the station magnitudes are also marked. Shading shows area used to estimate $\Psi^c(\infty)$.

Figure 27. P seismograms recorded at Eskdalemuir, Scotland from NTS explosion HANDLEY.

(a) Short-period seismogram (array sum)
(b) Seismogram (a) corrected for anelastic attenuation assuming $t^* = 0.2$ s
(c) Broad-band seismogram
(d) Seismogram (c) corrected for anelastic attenuation assuming $t^* = 0.2$ s
(e) Seismogram (c) corrected for anelastic attenuation assuming $t^* = 0.35$ s (deconvolved seismogram).

A_{pP} is the apparent pP pulse. A_S the slap-down pulse. The arrival time shown for PcP is the predicted time. The amplitude scale shown for each trace is in nanometres. The SP amplitudes and periods used to compute the station magnitudes are also marked. Shading shows area used to estimate $\Psi^c(\infty)$.

Figure 28. P seismograms recorded at Eskdalemuir, Scotland from NTS explosion ALMENDRO.

(a) Short-period seismogram (array sum)
(b) Seismogram (a) corrected for anelastic attenuation assuming $t^* = 0.2$ s
(c) Broad-band seismogram
(d) Seismogram (c) corrected for anelastic attenuation assuming $t^* = 0.2$ s
(e) Seismogram (c) corrected for anelastic attenuation assuming $t^* = 0.35$ s (deconvolved seismogram).

A_{pP} is the apparent pP pulse. The arrival time shown for PcP is the predicted time. The amplitude scale shown for each trace is in nanometres. The SP amplitudes and periods used to compute the station magnitudes are also marked. Shading shows area used to estimate $\Psi^c(\infty)$.

Figure 29. P seismograms recorded at Eskdalemuir, Scotland from NTS explosion TYBO.

(a) Short-period seismogram (array sum)
(b) Seismogram (a) corrected for anelastic attenuation assuming $t^* = 0.2$ s
(c) Broad-band seismogram
(d) Seismogram (c) corrected for anelastic attenuation assuming $t^* = 0.2$ s
(e) Seismogram (c) corrected for anelastic attenuation assuming $t^* = 0.35$ s (deconvolved seismogram).

A_{pP} is the apparent pP pulse. A_q marks possible arrivals from aftershocks of the explosion. The arrival time shown for PcP is the predicted time. The amplitude scale shown for each trace is in nanometres. The SP amplitudes and periods used to compute the station magnitudes are also marked. Shading shows area used to estimate $\Psi^c(\infty)$.

Figure 30. P seismograms recorded at Eskdalemuir, Scotland from NTS explosion STILTON.

(a) Short-period seismogram (array sum)
(b) Seismogram (a) corrected for anelastic attenuation assuming $t^* = 0.2$ s
(c) Broad-band seismogram
(d) Seismogram (c) corrected for anelastic attenuation assuming $t^* = 0.2$ s
(e) Seismogram (c) corrected for anelastic attenuation assuming $t^* = 0.35$ s (deconvolved seismogram).

A_{pP} is the apparent pP pulse. The arrival time shown for PcP is the predicted time. The amplitude scale shown for each trace is in nanometres. The SP amplitudes and periods used to compute the station magnitudes are also marked. Shading shows area used to estimate $\Psi^c(\infty)$.

Figure 31. P seismograms recorded at Eskdalemuir, Scotland from NTS explosion MAST.

(a) Short-period seismogram (array sum)
(b) Seismogram (a) corrected for anelastic attenuation assuming $t^* = 0.2$ s
(c) Broad-band seismogram
(d) Seismogram (c) corrected for anelastic attenuation assuming $t^* = 0.2$ s
(e) Seismogram (c) corrected for anelastic attenuation assuming $t^* = 0.35$ s (deconvolved seismogram).

A_{pP} is the apparent pP pulse. A_s the slap-down pulse. A_q marks possible arrivals from aftershocks of the explosion. The arrival time shown for PcP is the predicted time. The amplitude scale shown for each trace is in nanometres. The SP amplitudes and periods used to compute the station magnitudes are also marked. Shading shows area used to estimate $\Psi^c(\infty)$.

Figure 32. P seismograms recorded at Eskdalemuir, Scotland from NTS explosion CAMEMBERT.

(a) Short-period seismogram (array sum)
(b) Seismogram (a) corrected for anelastic attenuation assuming $t^* = 0.2$ s
(c) Broad-band seismogram
(d) Seismogram (c) corrected for anelastic attenuation assuming $t^* = 0.2$ s
(e) Seismogram (c) corrected for anelastic attenuation assuming $t^* = 0.35$ s (deconvolved seismogram).

A_{pP} is the apparent pP pulse. A_s the slap-down pulse. A_q marks possible arrivals from aftershocks of the explosion. The arrival time shown for PcP is the predicted time. The amplitude scale shown for each trace is in nanometres. The SP amplitudes and periods used to compute the station magnitudes are also marked. Shading shows area used to estimate $\Psi^c(\infty)$.

Figure 33. P seismograms recorded at Eskdalemuir, Scotland from NTS explosion KASSERI.

(a) Short-period seismogram (array sum)
(b) Seismogram (a) corrected for anelastic attenuation assuming $t^* = 0.2$ s
(c) Broad-band seismogram
(d) Seismogram (c) corrected for anelastic attenuation assuming $t^* = 0.2$ s
(e) Seismogram (c) corrected for anelastic attenuation assuming $t^* = 0.35$ s (deconvolved seismogram).

A_{pP} is the apparent pP pulse. A_{q_1} and A_{q_2} appear to have opposite polarity and may thus be P and pP from an aftershock of the explosion. The arrival time shown for PcP is the predicted time. The amplitude scale shown for each trace is in nanometres. The SP amplitudes and periods used to compute the station magnitudes are also marked. Shading shows area used to estimate $\Psi^c(\infty)$.

Figure 34. P seismograms recorded at Eskdalemuir, Scotland from NTS explosion INLET.

(a) Short-period seismogram (array sum)
(b) Seismogram (a) corrected for anelastic attenuation assuming $t^* = 0.2$ s
(c) Broad-band seismogram
(d) Seismogram (c) corrected for anelastic attenuation assuming $t^* = 0.2$ s
(e) Seismogram (c) corrected for anelastic attenuation assuming $t^* = 0.35$ s (deconvolved seismogram).

A_{pP} is the apparent pP pulse. The arrival time shown for PcP is the predicted time. The amplitude scale shown for each trace is in nanometres. The SP amplitudes and periods used to compute the station magnitudes are also marked. Shading shows area used to estimate $\Psi^c(\infty)$.

Figure 35. P seismograms recorded at Eskdalemuir, Scotland from NTS explosion MUENSTER.

(a) Short-period seismogram (array sum)
(b) Seismogram (a) corrected for anelastic attenuation assuming $t^* = 0.2$ s
(c) Broad-band seismogram
(d) Seismogram (c) corrected for anelastic attenuation assuming $t^* = 0.2$ s
(e) Seismogram (c) corrected for anelastic attenuation assuming $t^* = 0.35$ s (deconvolved seismogram).

A_{pP} is the apparent pP pulse. A_S the slap-down pulse. The arrival time shown for PcP is the predicted time. The amplitude scale shown for each trace is in nanometres. The SP amplitudes and periods used to compute the station magnitudes are also marked. Shading shows area used to estimate $\Psi^c(\infty)$.

Figure 36. P seismograms recorded at Eskdalemuir, Scotland from NTS explosion FONTINA.

(a) Short-period seismogram (array sum)
(b) Seismogram (a) corrected for anelastic attenuation assuming $t^* = 0.2$ s
(c) Broad-band seismogram
(d) Seismogram (c) corrected for anelastic attenuation assuming $t^* = 0.2$ s
(e) Seismogram (c) corrected for anelastic attenuation assuming $t^* = 0.35$ s (deconvolved seismogram).

A_{pP} is the apparent pP pulse. A_S the slap-down pulse. The arrival time shown for PcP is the predicted time. The amplitude scale shown for each trace is in nanometres. The SP amplitudes and periods used to compute the station magnitudes are also marked. Shading shows area used to estimate $\Psi^C(\infty)$.

Figure 37. P seismograms recorded at Eskdalemuir, Scotland from NTS explosion CHESHIRE.

(a) Short-period seismogram (array sum)
(b) Seismogram (a) corrected for anelastic attenuation assuming $t^* = 0.2$ s
(c) Broad-band seismogram
(d) Seismogram (c) corrected for anelastic attenuation assuming $t^* = 0.2$ s
(e) Seismogram (c) corrected for anelastic attenuation assuming $t^* = 0.35$ s (deconvolved seismogram).

A_{pP} is the apparent pP pulse. A_S the slap-down pulse. The arrival time shown for PcP is the predicted time. The amplitude scale shown for each trace is in nanometres. The SP amplitudes and periods used to compute the station magnitudes are also marked. Shading shows area used to estimate $\Psi^C(\infty)$.

Figure 38. P seismograms recorded at Eskdalemuir, Scotland from NTS explosion ESTUARY.

(a) Short-period seismogram (array sum)
(b) Seismogram (a) corrected for anelastic attenuation assuming $t^* = 0.2$ s
(c) Broad-band seismogram
(d) Seismogram (c) corrected for anelastic attenuation assuming $t^* = 0.2$ s
(e) Seismogram (c) corrected for anelastic attenuation assuming $t^* = 0.35$ s (deconvolved seismogram).

A_{pP} is the apparent pP pulse. A_S the slap-down pulse. The arrival time shown for PcP is the predicted time. The amplitude scale shown for each trace is in nanometres. The SP amplitudes and periods used to compute the station magnitudes are also marked. Shading shows area used to estimate $\Psi^C(\infty)$.

Figure 39. P seismograms recorded at Eskdalemuir, Scotland from NTS explosion COLBY.

(a) Short-period seismogram (array sum)
(b) Seismogram (a) corrected for anelastic attenuation assuming $t^* = 0.2$ s
(c) Broad-band seismogram
(d) Seismogram (c) corrected for anelastic attenuation assuming $t^* = 0.2$ s
(e) Seismogram (c) corrected for anelastic attenuation assuming $t^* = 0.35$ s (deconvolved seismogram).

A_{pP} is the apparent pP pulse. A_S the slap-down pulse. The arrival time shown for PcP is the predicted time. The amplitude scale shown for each trace is in nanometres. The SP amplitudes and periods used to compute the station magnitudes are also marked. Shading shows area used to estimate $\Psi^C(\infty)$.

Figure 40. P seismograms recorded at Eskdalemuir, Scotland from NTS explosion POOL.

(a) Short-period seismogram (array sum)
(b) Seismogram (a) corrected for anelastic attenuation assuming $t^* = 0.2$ s
(c) Broad-band seismogram
(d) Seismogram (c) corrected for anelastic attenuation assuming $t^* = 0.2$ s
(e) Seismogram (c) corrected for anelastic attenuation assuming $t^* = 0.35$ s (deconvolved seismogram).

A_{pP} is the apparent pP pulse. A_S the slap-down pulse. The arrival time shown for PcP is the predicted time. The amplitude scale shown for each trace is in nanometres. The SP amplitudes and periods used to compute the station magnitudes are also marked. Shading shows area used to estimate $\Psi^C(\infty)$.

Figure 41. P seismograms recorded at Eskdalemuir, Scotland from NTS explosion BACKBEACH.

(a) Short-period seismogram (array sum)
(b) Seismogram (a) corrected for anelastic attenuation assuming $t^* = 0.2$ s
(c) Broad-band seismogram
(d) Seismogram (c) corrected for anelastic attenuation assuming $t^* = 0.2$ s
(e) Seismogram (c) corrected for anelastic attenuation assuming $t^* = 0.35$ s (deconvolved seismogram).

A_{pP} is the apparent pP pulse. A_S the slap-down pulse. The arrival time shown for PcP is the predicted time. The amplitude scale shown for each trace is in nanometres. The SP amplitudes and periods used to compute the station magnitudes are also marked. Shading shows area used to estimate $\Psi^C(\infty)$.

Figure 42. P seismograms recorded at Eskdalemuir, Scotland from NTS explosion PANIR.

(a) Short-period seismogram (array sum)
(b) Seismogram (a) corrected for anelastic attenuation assuming $t^* = 0.2$ s
(c) Broad-band seismogram
(d) Seismogram (c) corrected for anelastic attenuation assuming $t^* = 0.2$ s
(e) Seismogram (c) corrected for anelastic attenuation assuming $t^* = 0.35$ s (deconvolved seismogram).

A_{pP} is the apparent pP pulse. A_S the slap-down pulse. The arrival time shown for PcP is the predicted time. The amplitude scale shown for each trace is in nanometres. The SP amplitudes and periods used to compute the station magnitudes are also marked. Shading shows area used to estimate $\Psi^C(\infty)$.

Figure 43. The short-period seismograms for the Yucca Flats explosions arranged in order of depth of firing.

Figure 44. The short-period seismograms for the Pahute Mesa explosions arranged in order of depth of firing.

Figure 45. The deconvolved BB seismograms for the Yucca Flats explosions arranged in order of depth of firing.

Figure 46. The deconvolved BB seismograms for the Pahute Mesa explosions arranged in order of depth of firing.

Figure 47. Graph of m_b^C against m_b^O. m_b^C is the body wave magnitude computed from the Eskdalemuir SP seismograms corrected for attenuation with $t^* = 0.2$ s. m_b^O is the body wave magnitude computed from the observed SP seismograms (m_b^O and m_b^C are listed in table 2).

Figure 48. (a) Plot of $\Psi^C(\infty)$ estimates against yield for Nevada explosions for which yields have been announced. $\Psi^C(\infty)$ estimates for the Amchitka Island explosions are also shown.

(b) Plot of $\log^A/T$ against yield for Nevada explosions for which yields have been announced. Log^A/T for the Amchitka Island explosions are also shown. The yields for the Amchitka Island explosions are taken from von Seggern and Blandford (24).

Figure 49. Plot of $\Psi(\infty)$ estimates plotted against m_b^{ML}, the maximum-likelihood estimate of the body wave magnitude. (m_b^{ML} is listed in table 2).

Figure 50. Plot of rise times against m_b^{ML} - the maximum-likelihood estimate of body wave magnitudes (m_b^{ML} is listed in table 2).

Figure 51. Plot of estimated pP-P time against predicted time. (Estimated and predicted times are listed in table 2).

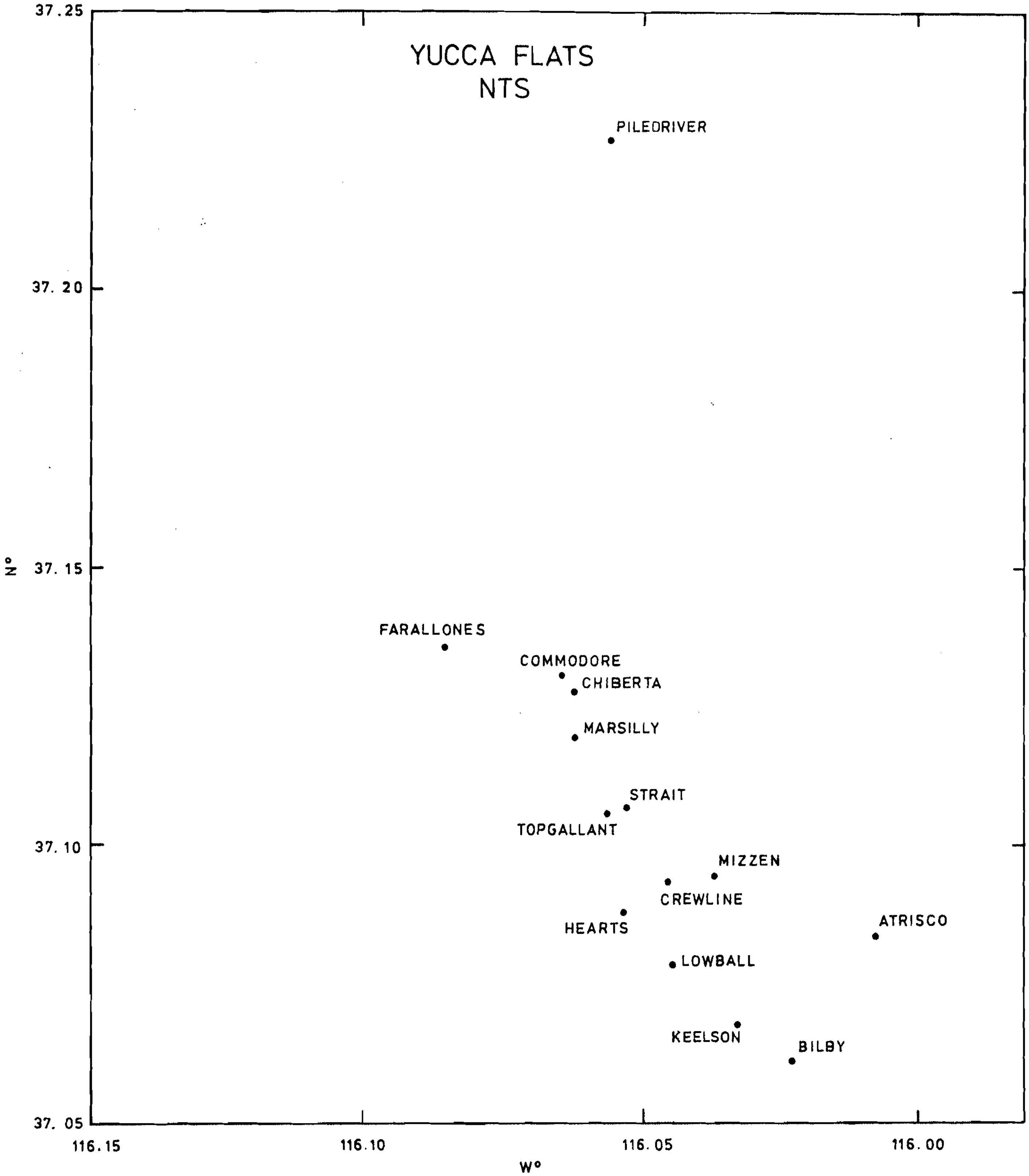

FIGURE 1. MAPS SHOWING EPICENTRES OF THE NEVADA TEST SITE EXPLOSIONS FOR WHICH SEISMOGRAMS ARE GIVEN IN THIS REPORT

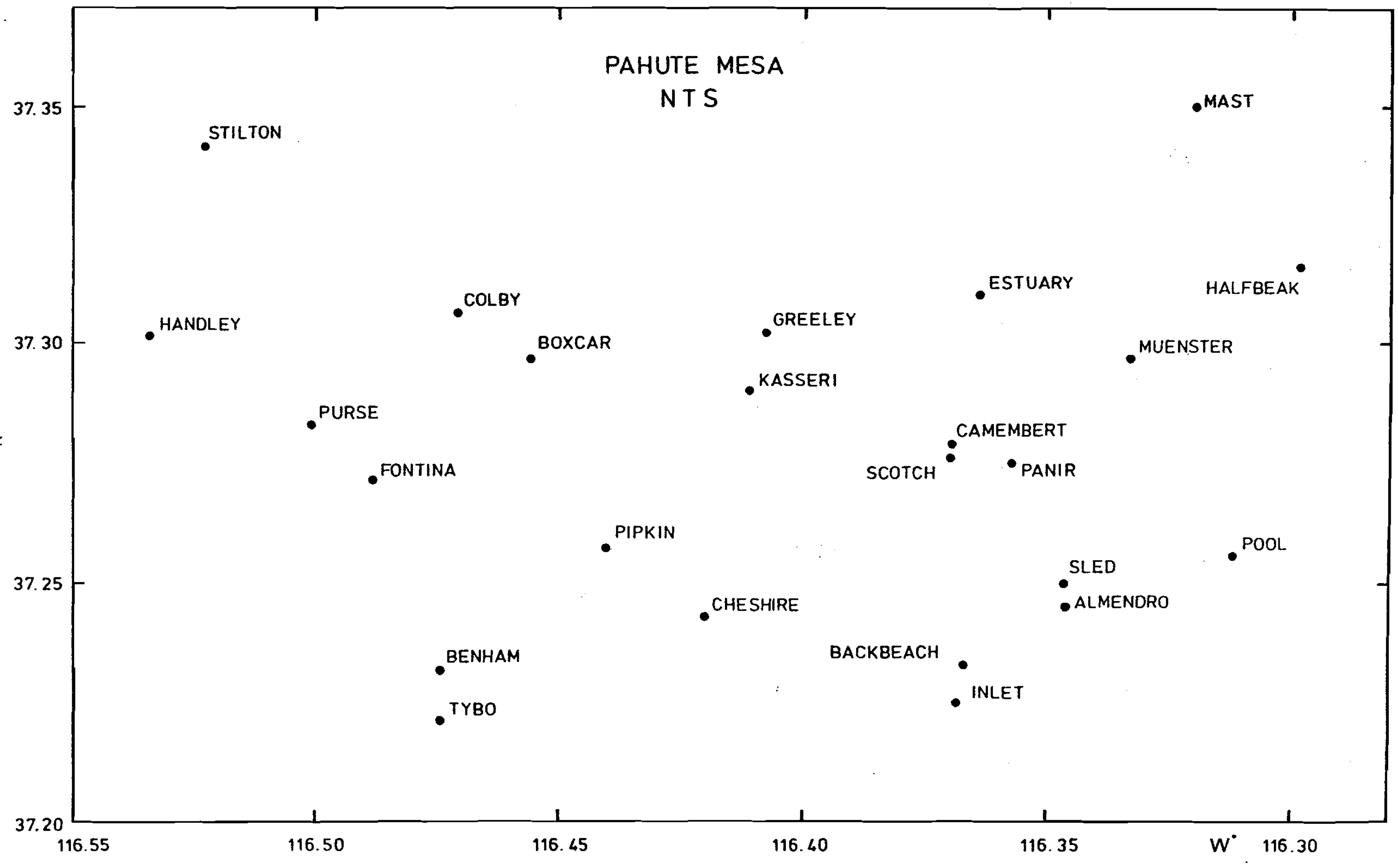

FIGURE 1. Cont'd

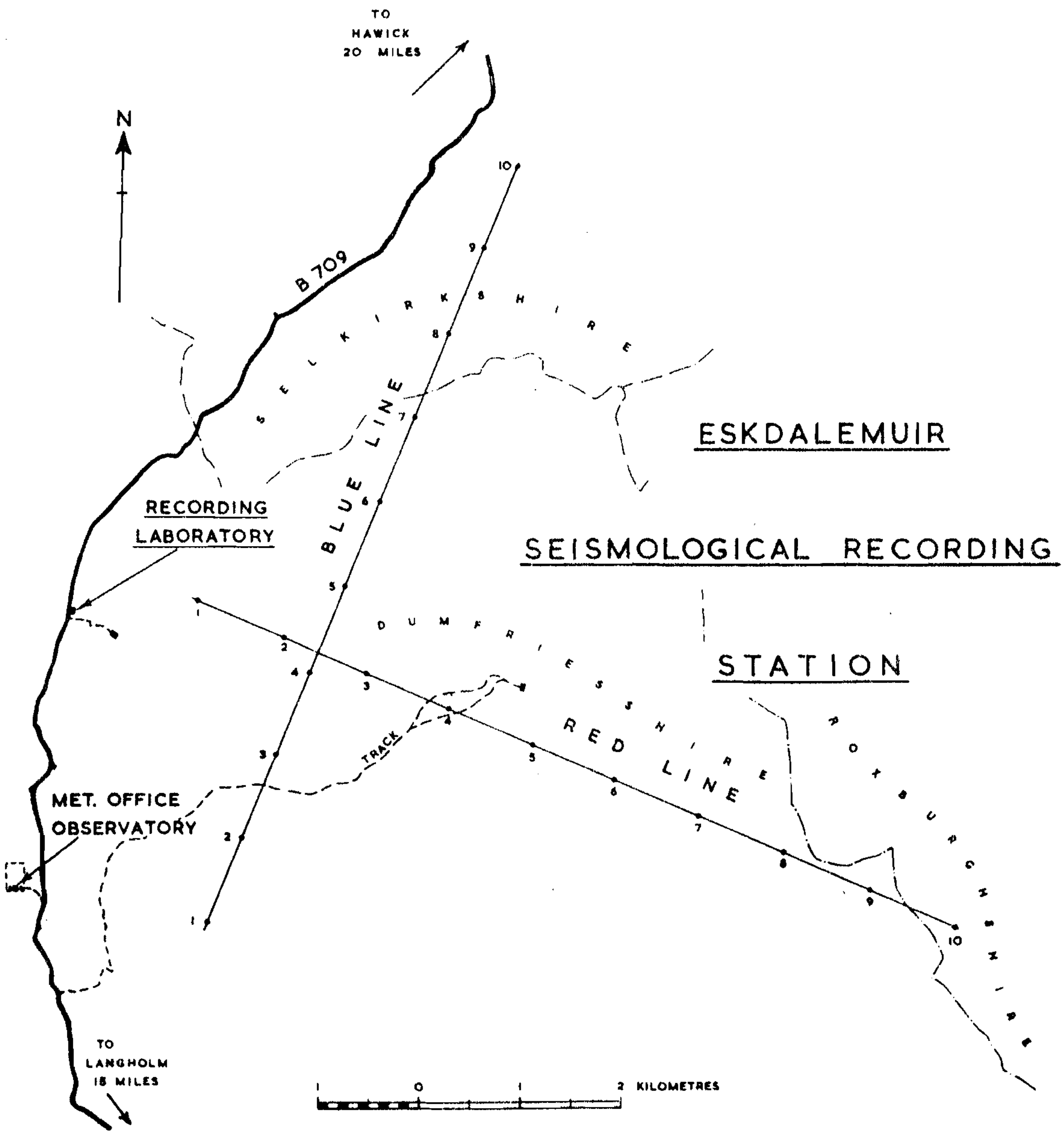

FIGURE 2. LAYOUT OF THE ESKDALEMUIR ARRAY

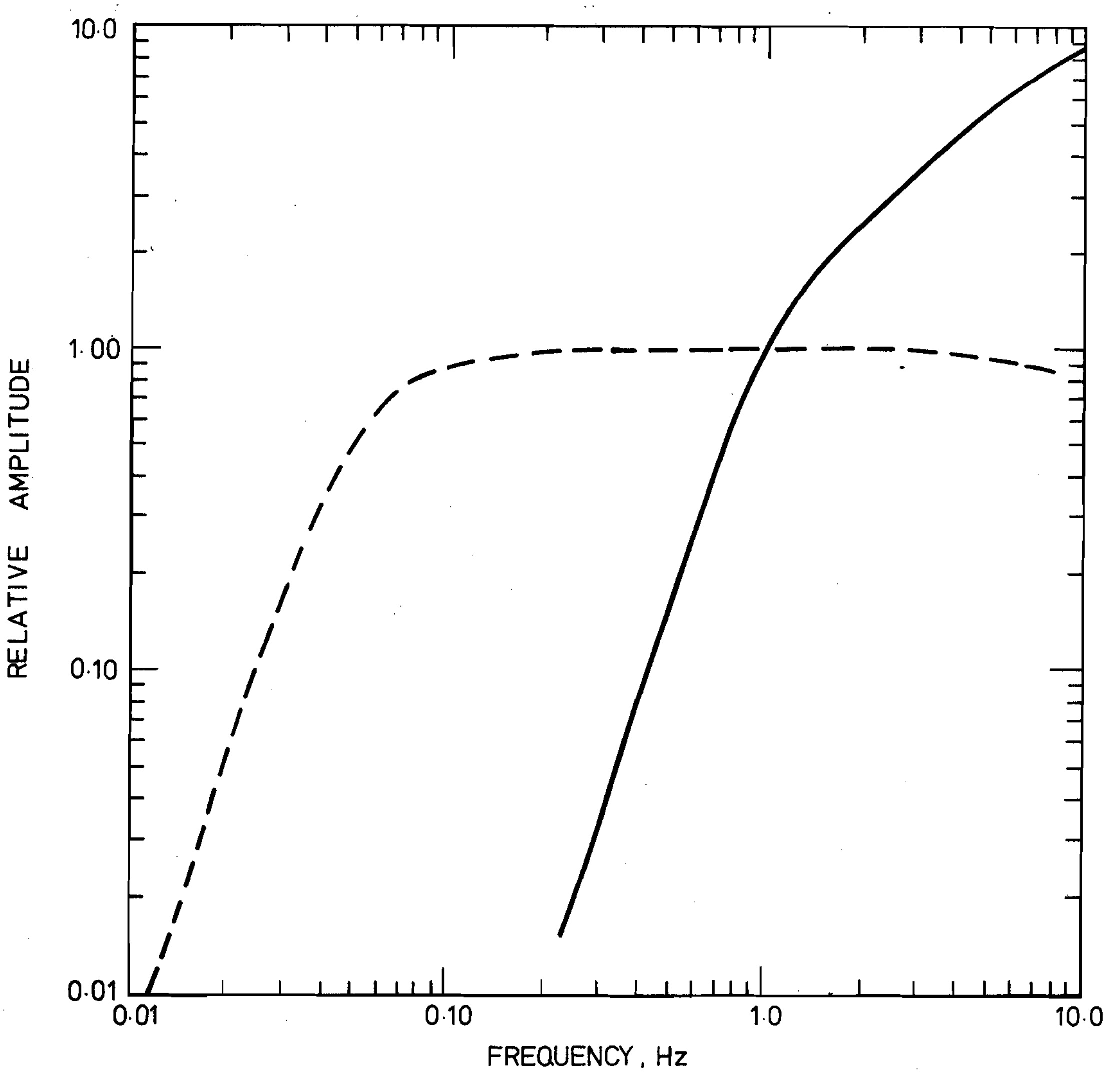

FIGURE 3. AMPLITUDE RESPONSE AS A FUNCTION OF FREQUENCY OF SHORT-PERIOD AND BROAD-BAND SYSTEMS

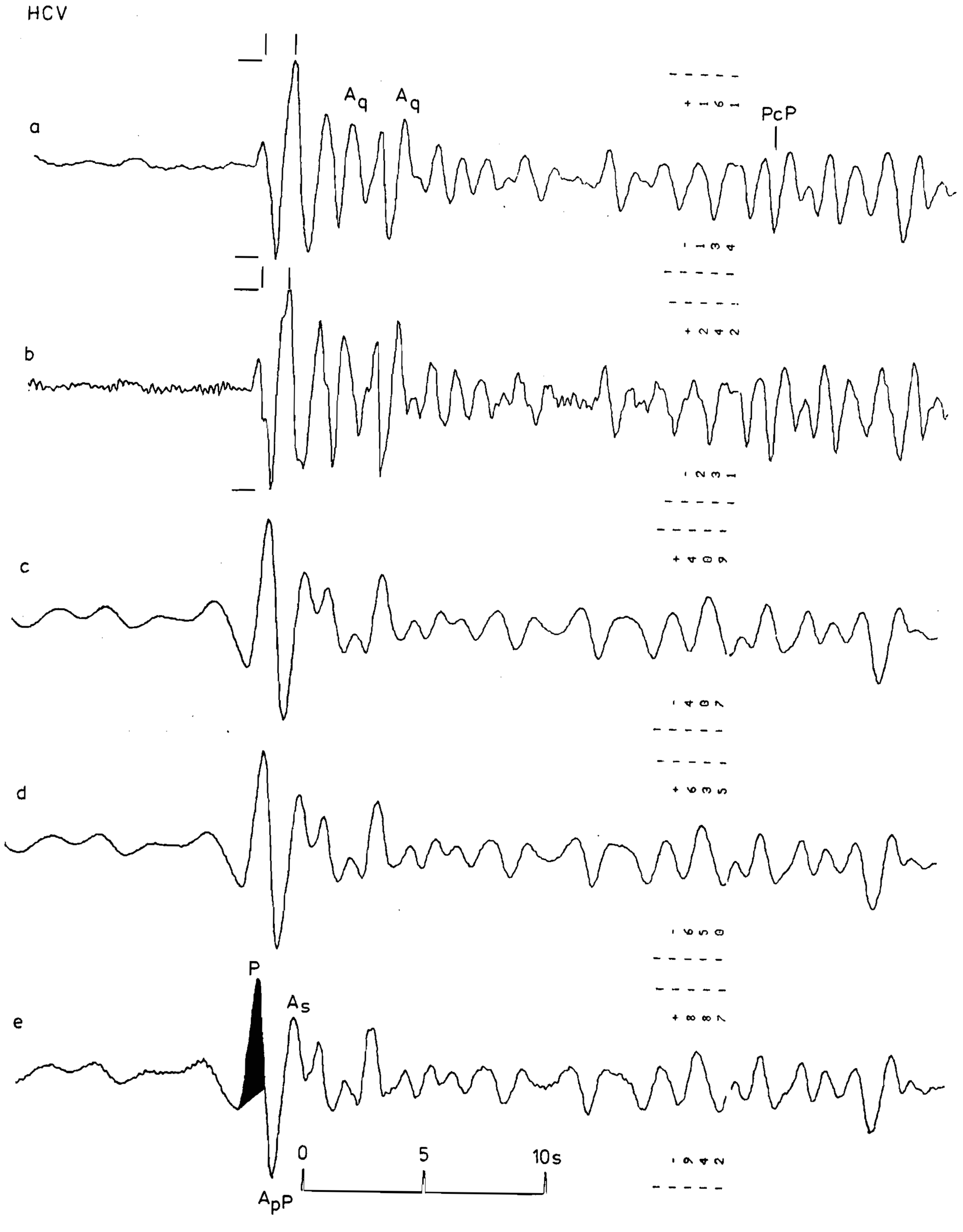

FIGURE 4. P SEISMOGRAMS RECORDED AT ESKDALEMUIR, SCOTLAND FROM NTS EXPLOSION FAULTLESS

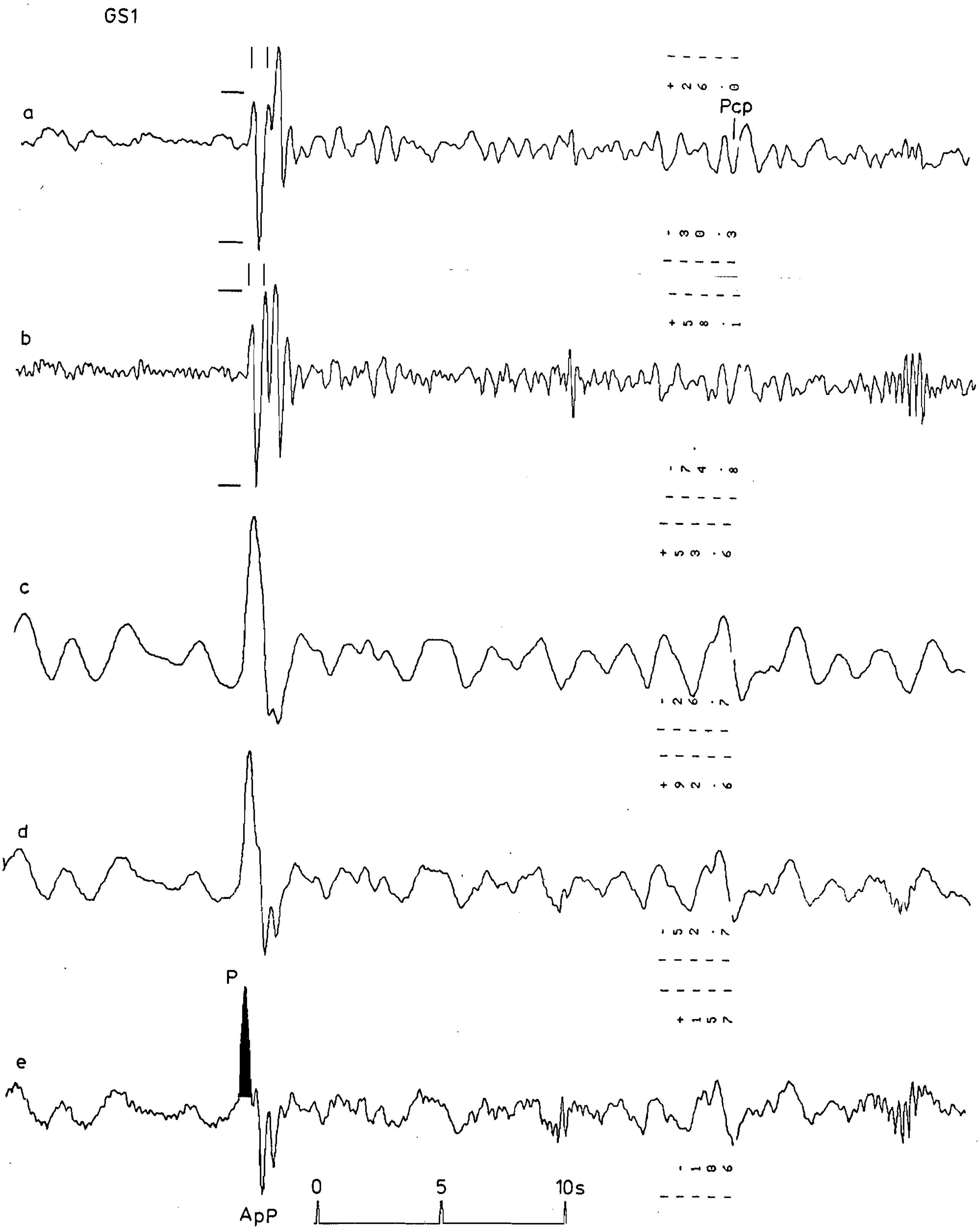

FIGURE 5. P SEISMOGRAMS RECORDED AT ESKDALEMUIR, SCOTLAND FROM NTS EXPLOSION PILE DRIVER

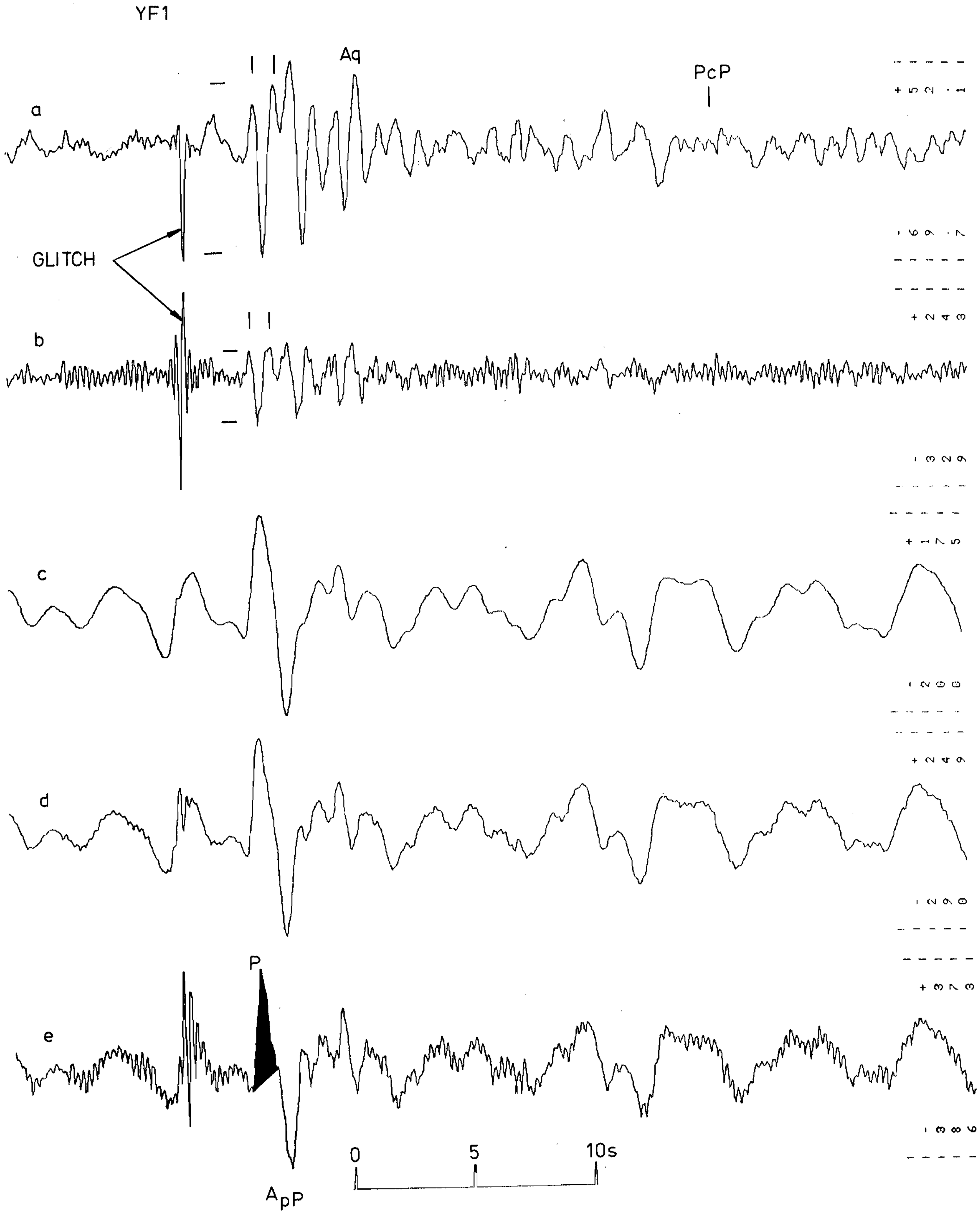

FIGURE 6. P SEISMOGRAMS RECORDED AT ESKDALEMUIR, SCOTLAND FROM NTS EXPLOSION BILBY

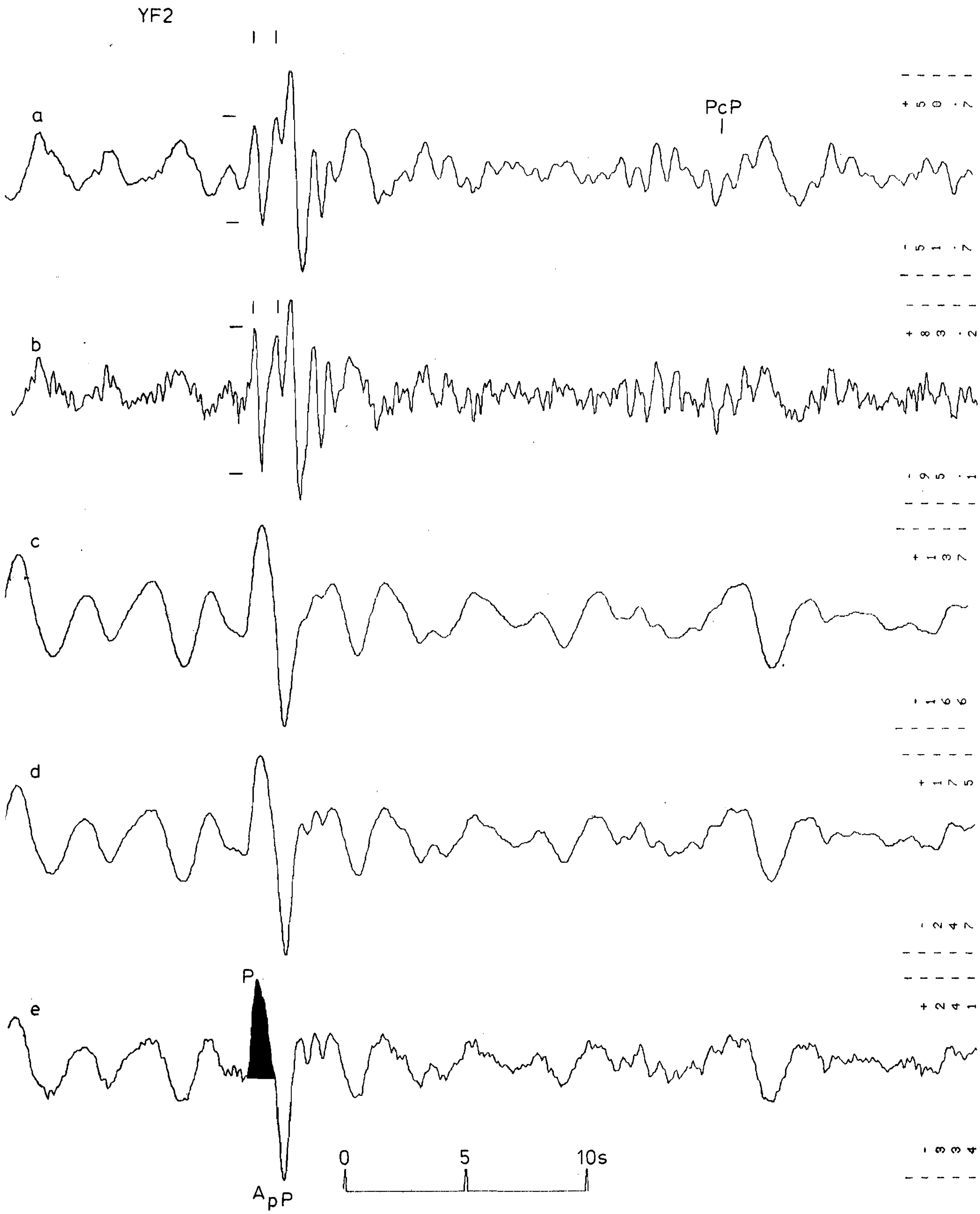

FIGURE 7. P SEISMOGRAMS RECORDED AT ESKDALEMUIR, SCOTLAND FROM NTS EXPLOSION COMMODORE

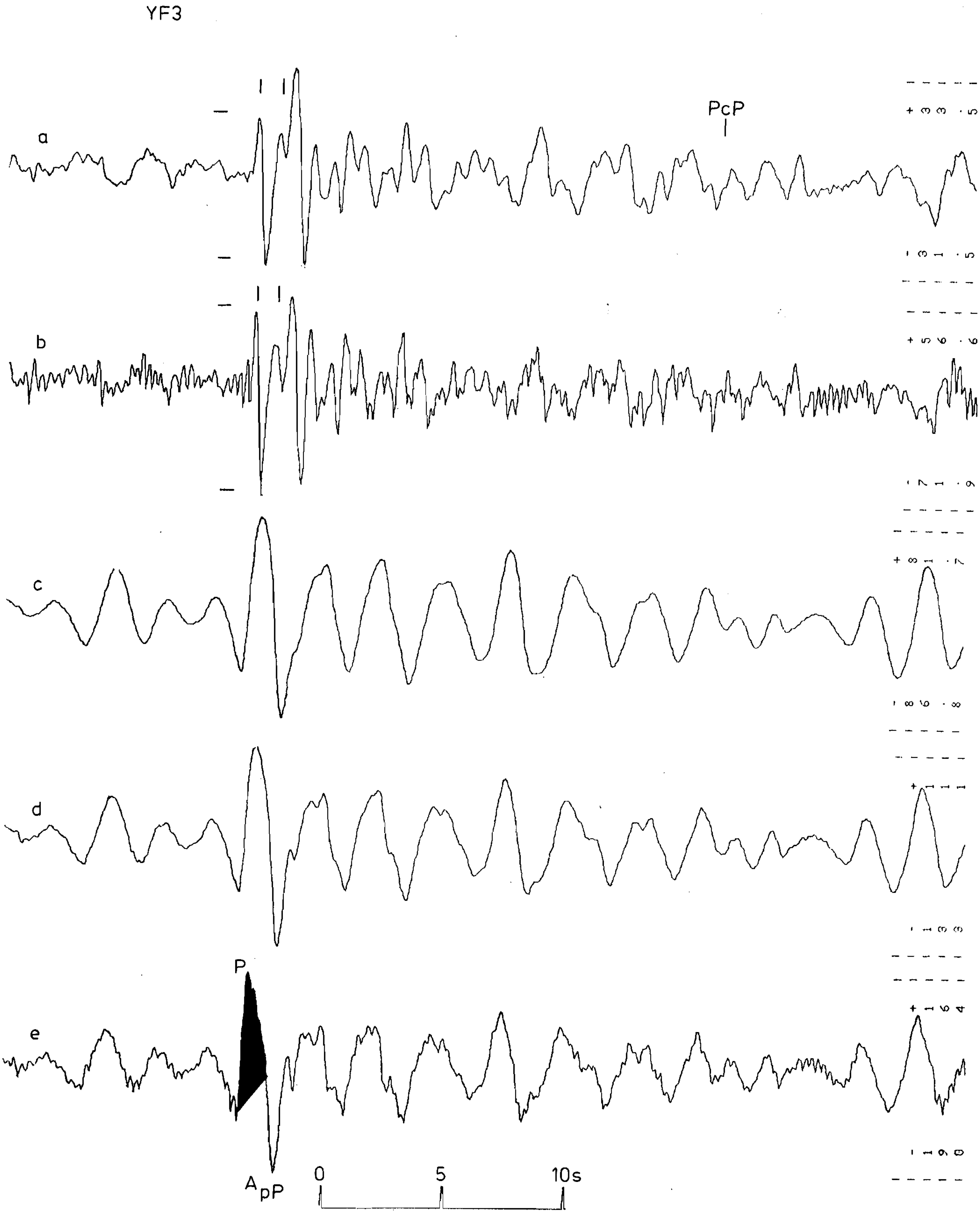

FIGURE 8. P SEISMOGRAMS RECORDED AT ESKDALEMUIR, SCOTLAND FROM NTS EXPLOSION TOPGALLANT

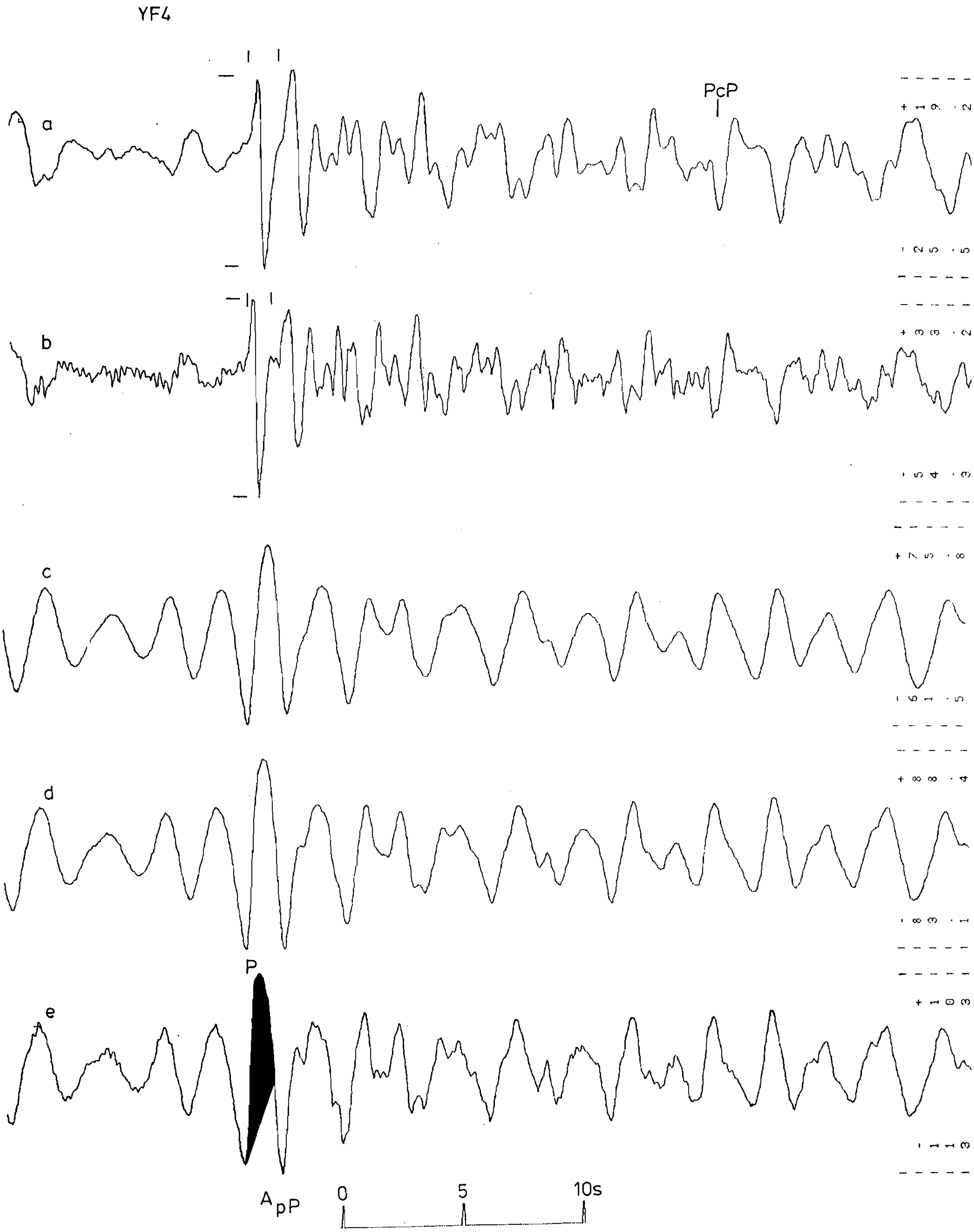

FIGURE 9. P SEISMOGRAMS RECORDED AT ESKDALEMUIR, SCOTLAND FROM NTS EXPLOSION MIZZEN

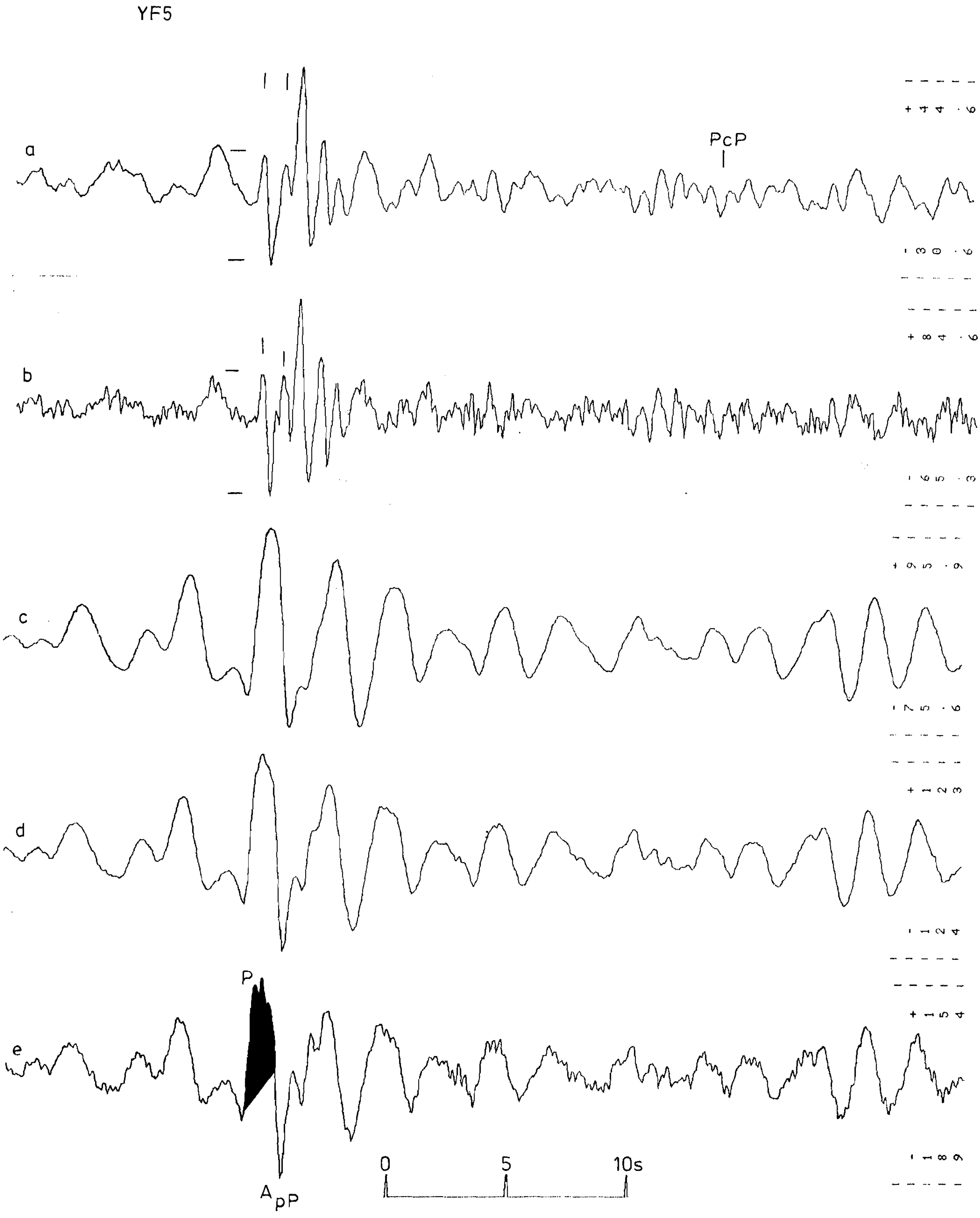

FIGURE 10. P SEISMOGRAMS RECORDED AT ESKDALEMUIR, SCOTLAND FROM NTS EXPLOSION CHIBERTA

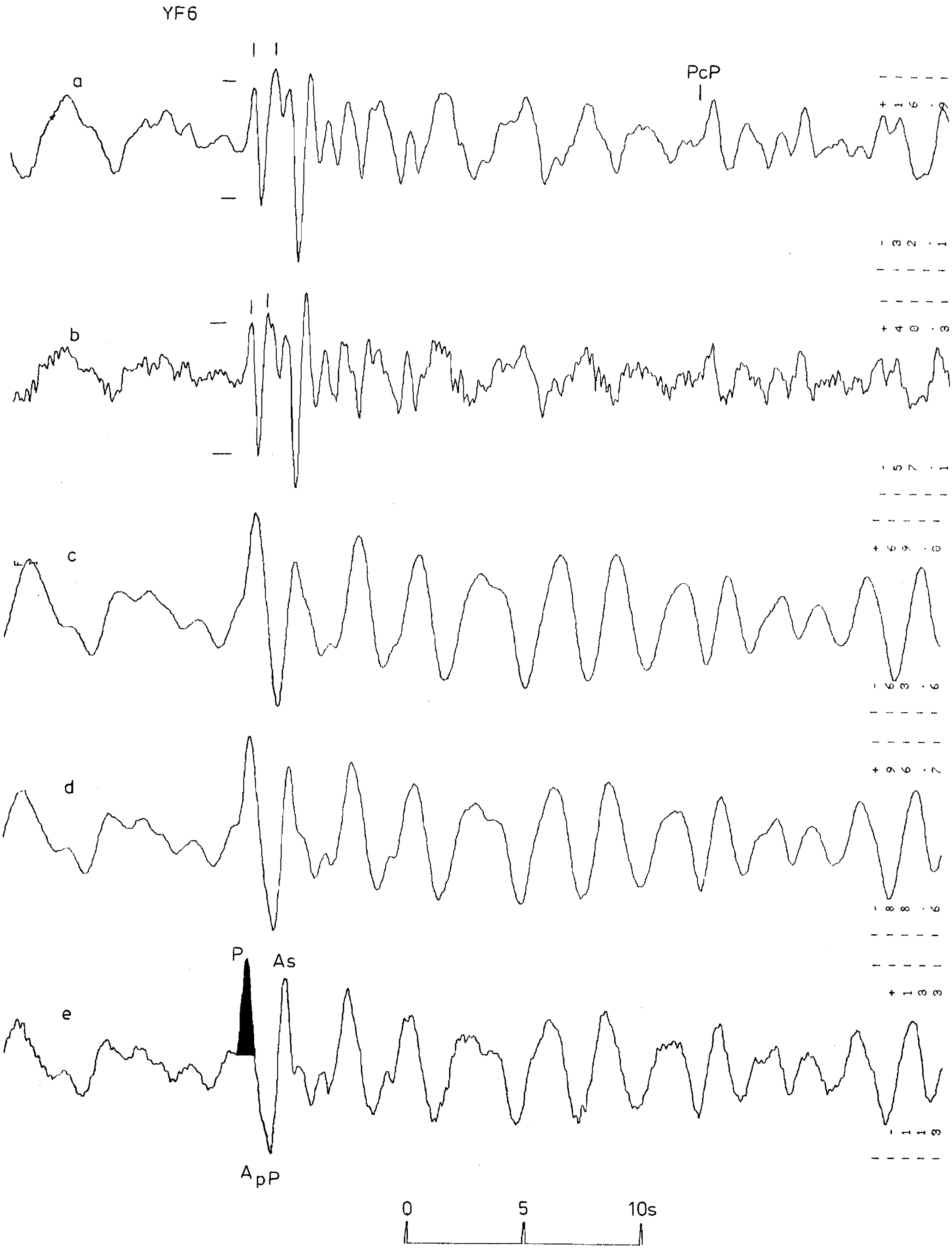

FIGURE 11. P SEISMOGRAMS RECORDED AT ESKDALEMUIR, SCOTLAND FROM NTS EXPLOSION KEELSON

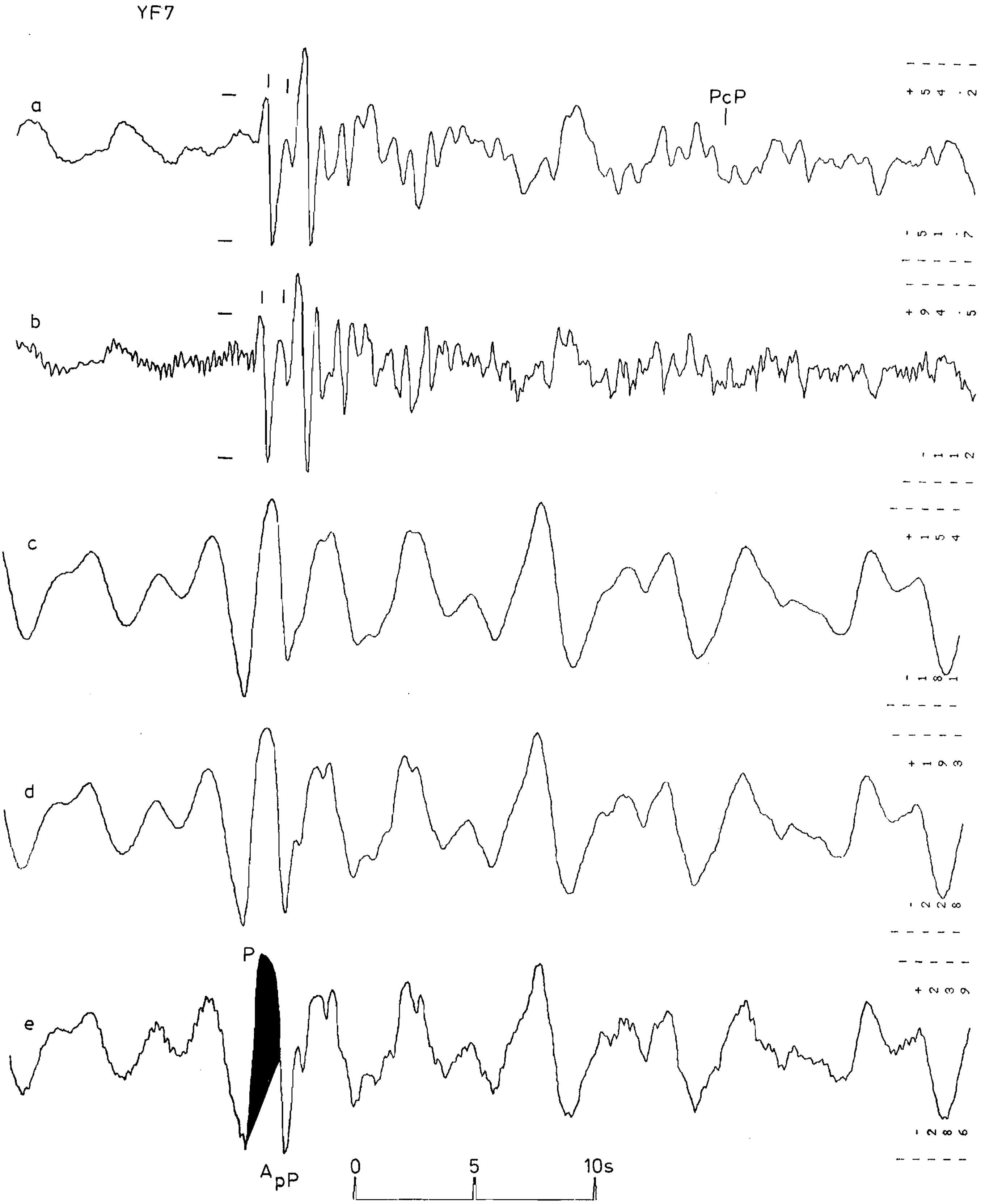

FIGURE 12. P SEISMOGRAMS RECORDED AT ESDKALEMUIR, SCOTLAND FROM NTS EXPLOSION STRAIT

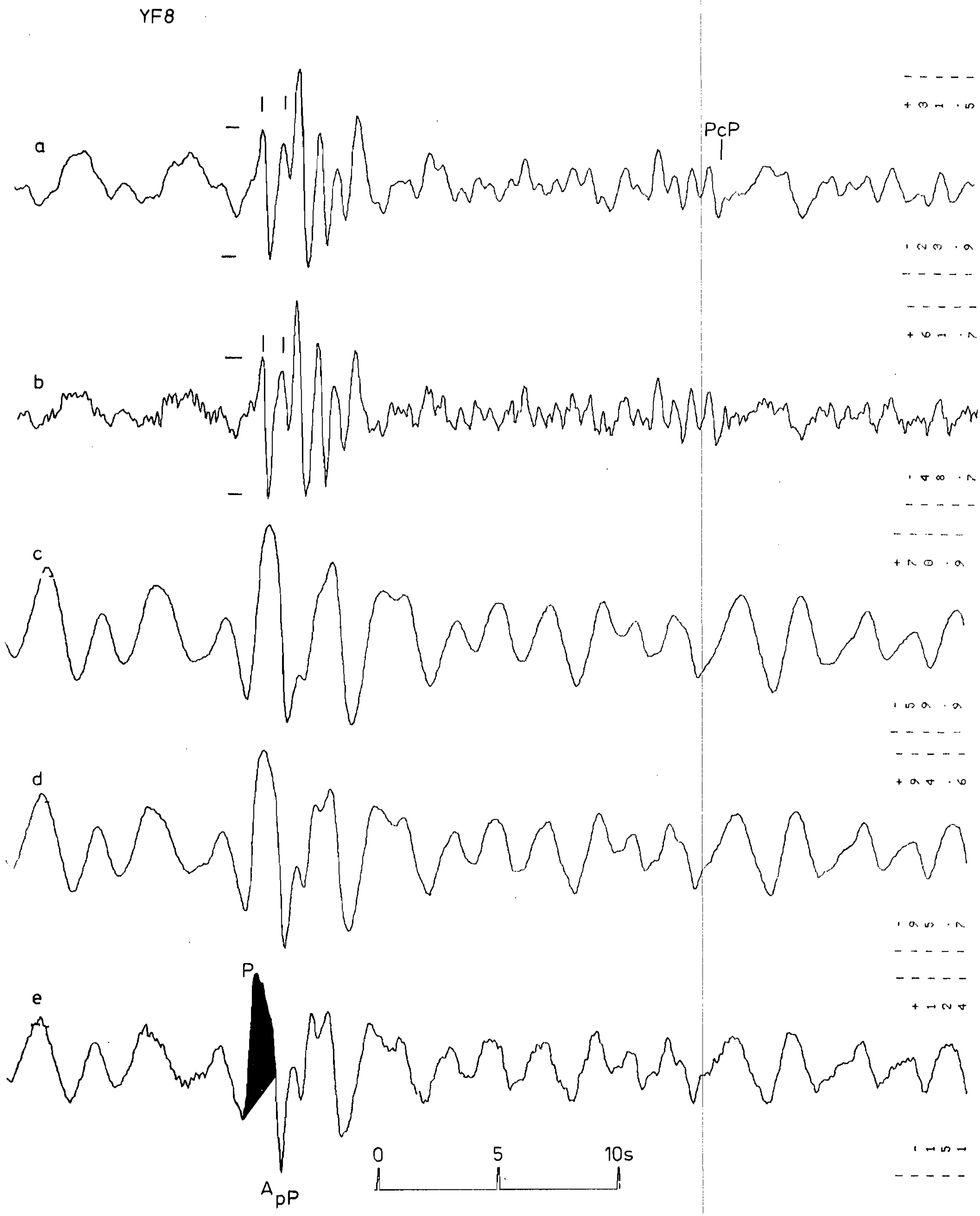

FIGURE 13. P SEISMOGRAMS RECORDED AT ESKDALEMUIR, SCOTLAND FROM NTS EXPLOSION MARSILLY

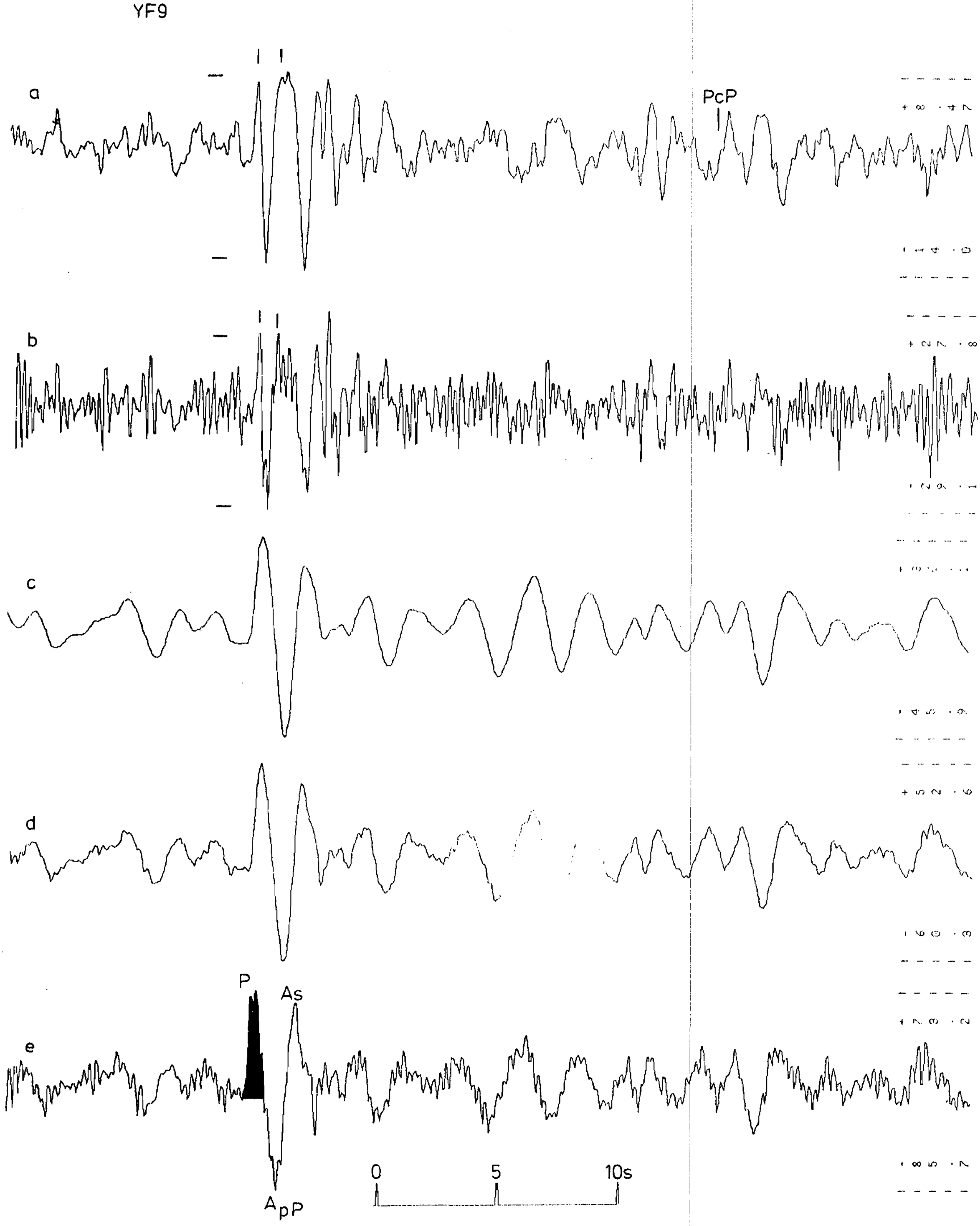

FIGURE 14. P SEISMOGRAMS RECORDED AT ESKDALEMUIR, SCOTLAND FROM NTS EXPLOSION CREWLINE

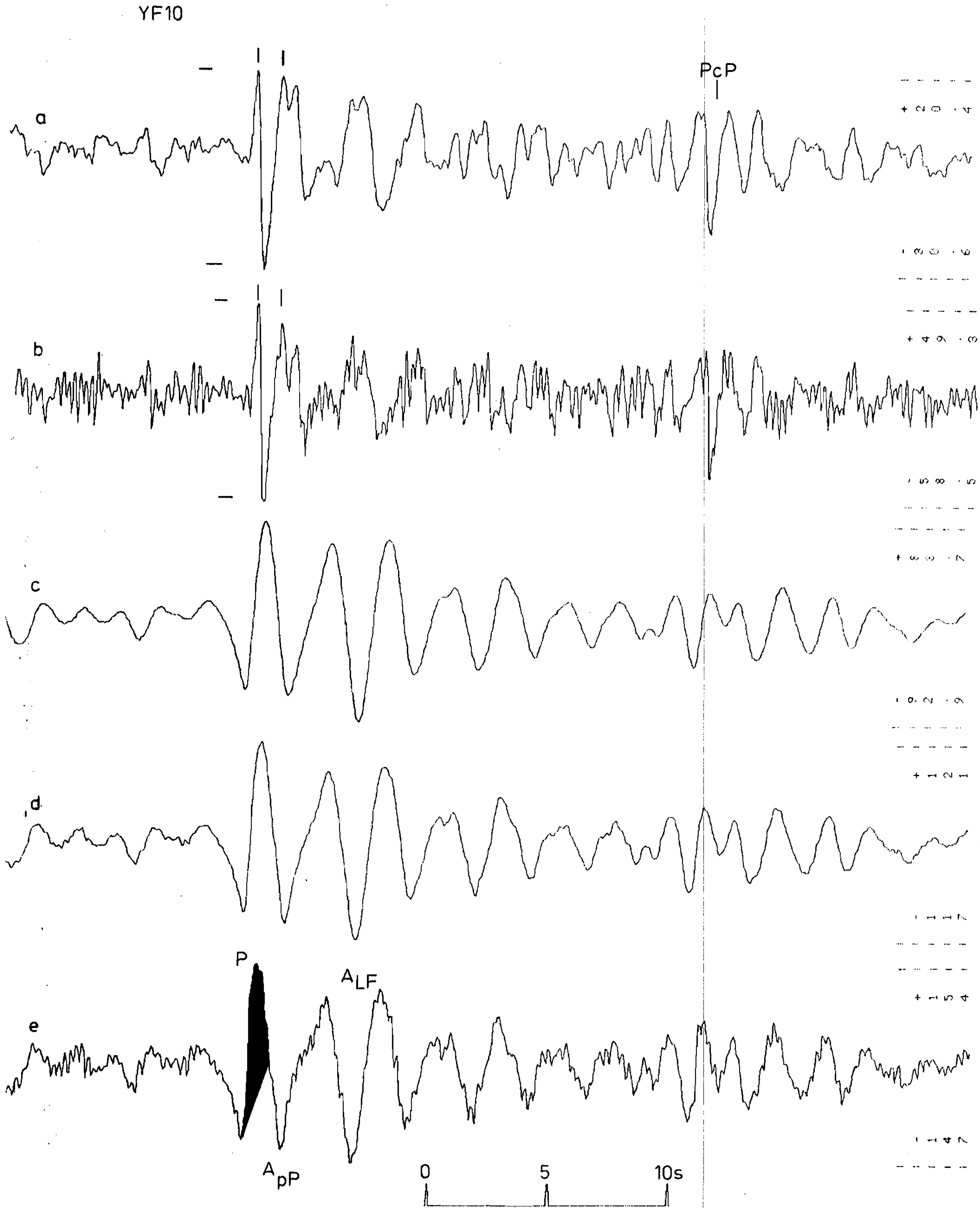

FIGURE 15. P SEISMOGRAMS RECORDED AT ESKDALEMUIR, SCOTLAND FROM NTS EXPLOSION FARALLONES

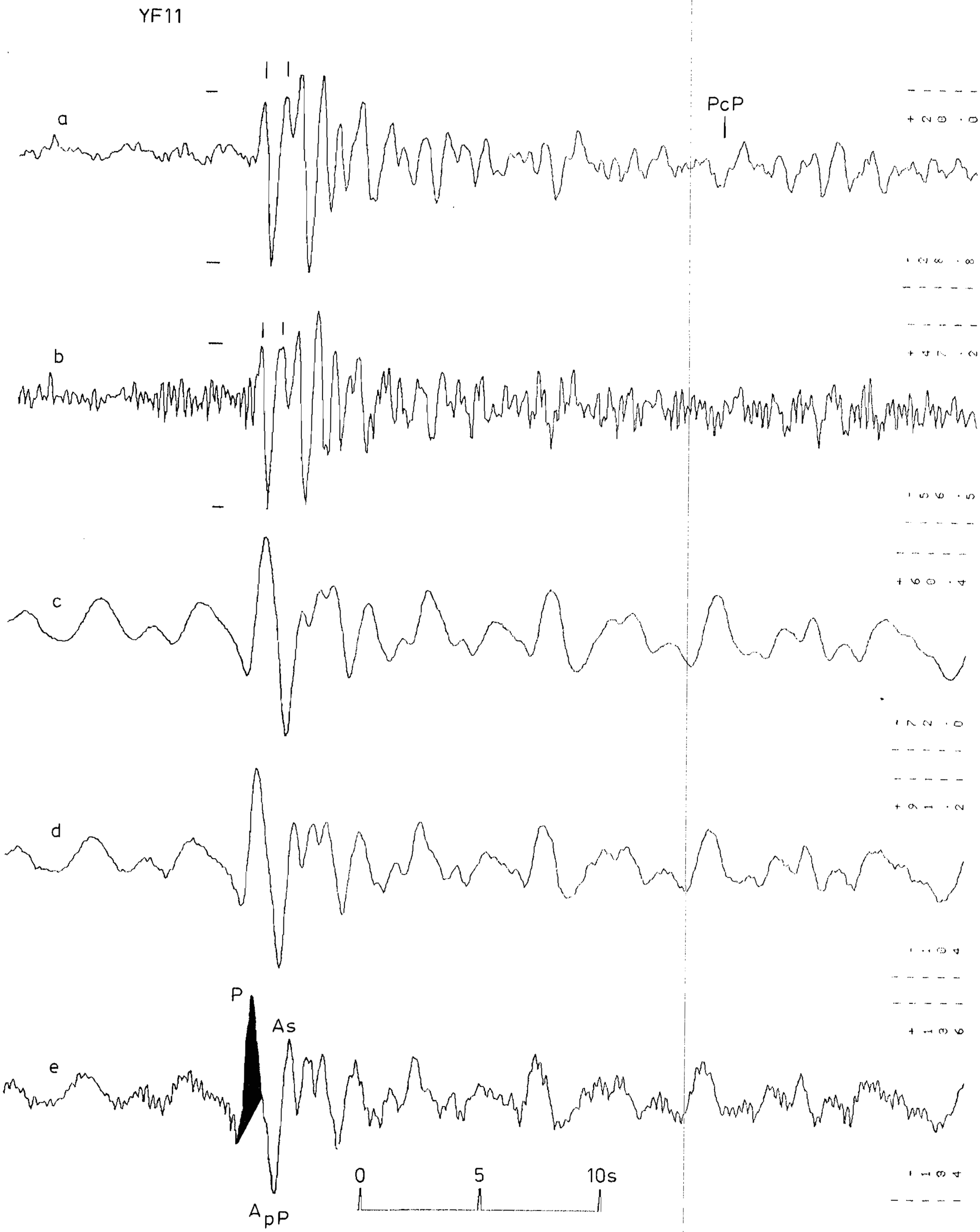

FIGURE 16. P SEISMOGRAMS RECORDED AT ESKDALEMUIR, SCOTLAND FROM NTS EXPLOSION LOWBALL

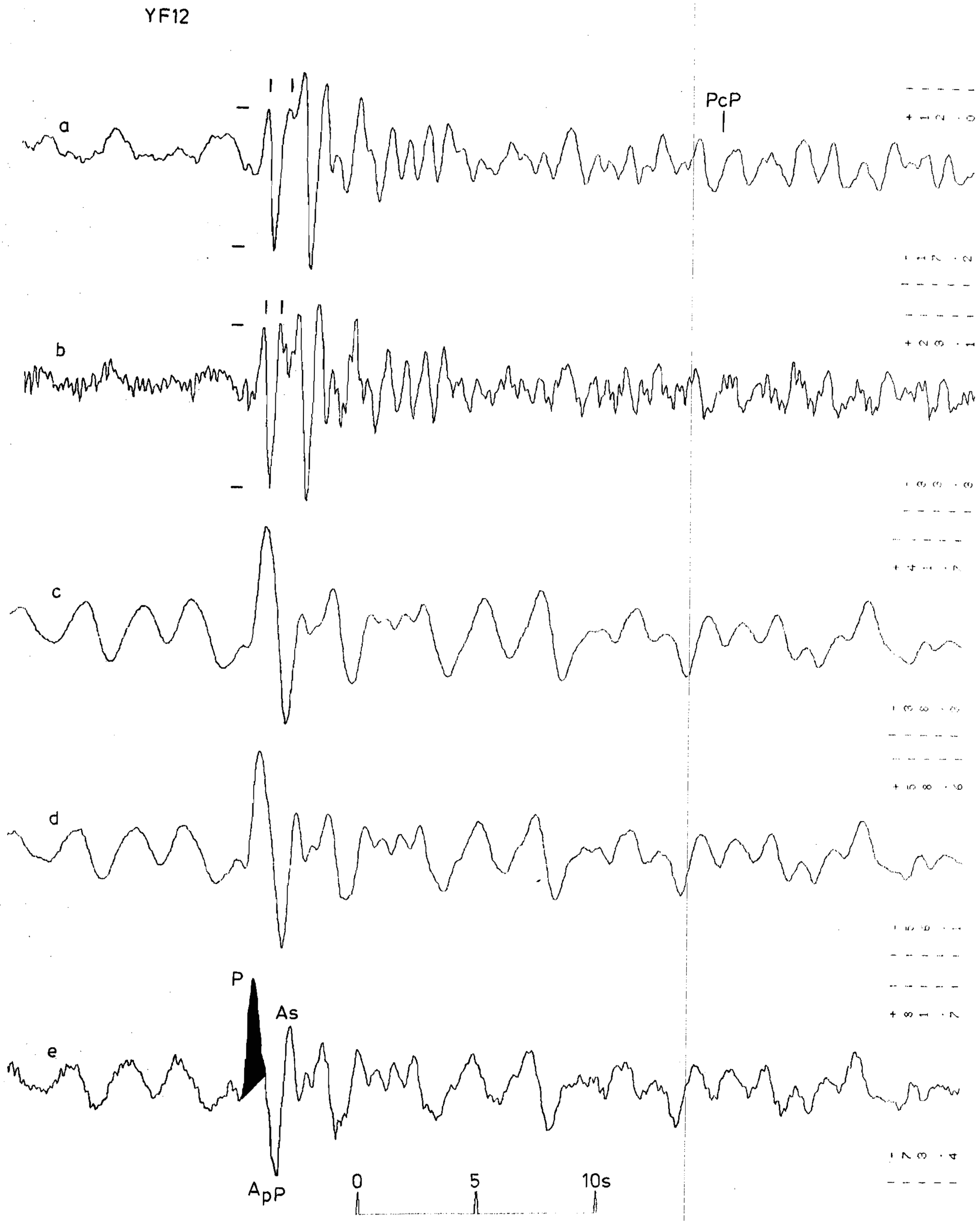

FIGURE 17. P SEISMOGRAMS RECORDED AT ESKDALEMUIR, SCOTLAND FROM NTS EXPLOSION HEARTS

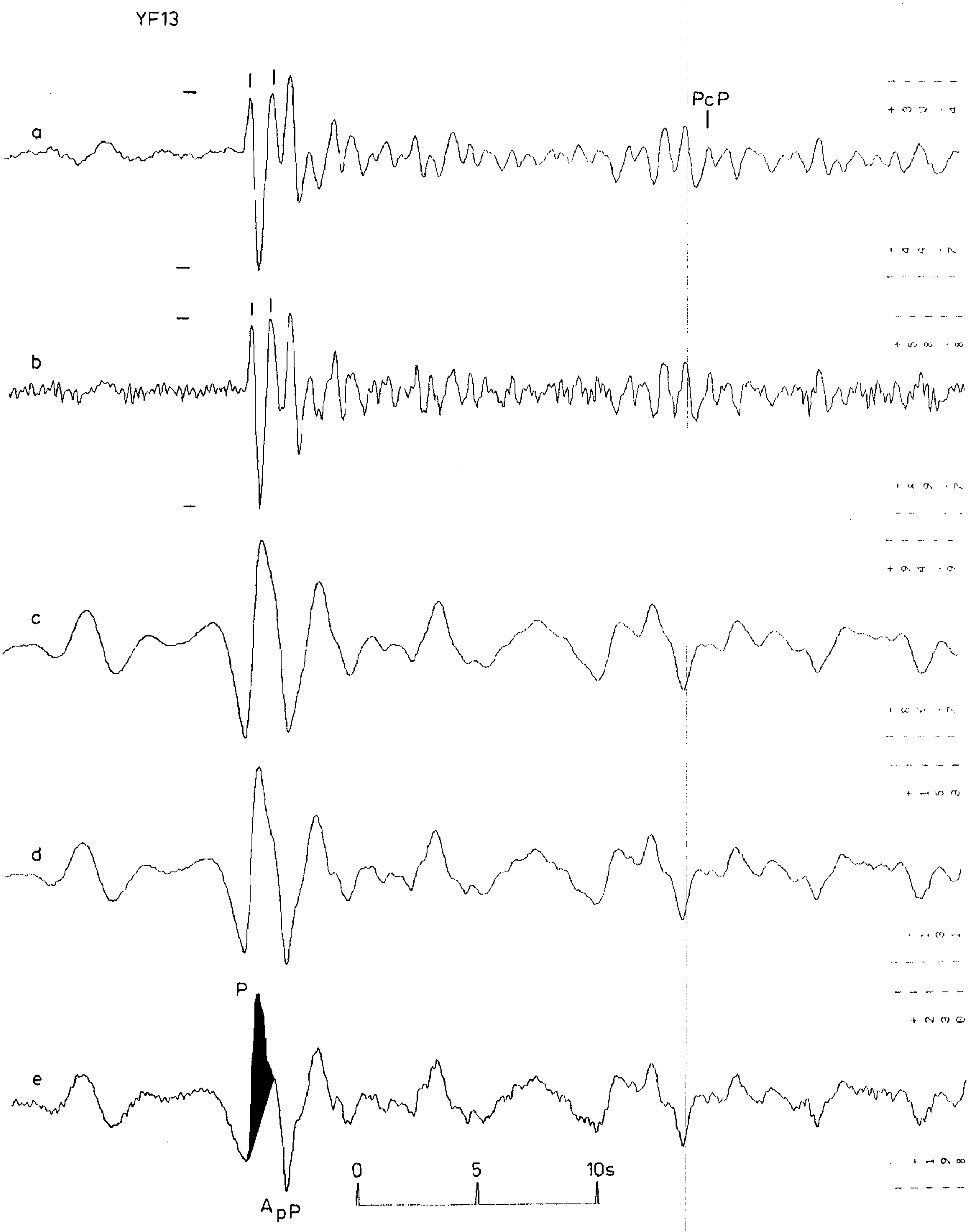

FIGURE 18. P SEISMOGRAMS RECORDED AT ESKDALEMUIR, SCOTLAND FROM NTS EXPLOSION ATRISCO

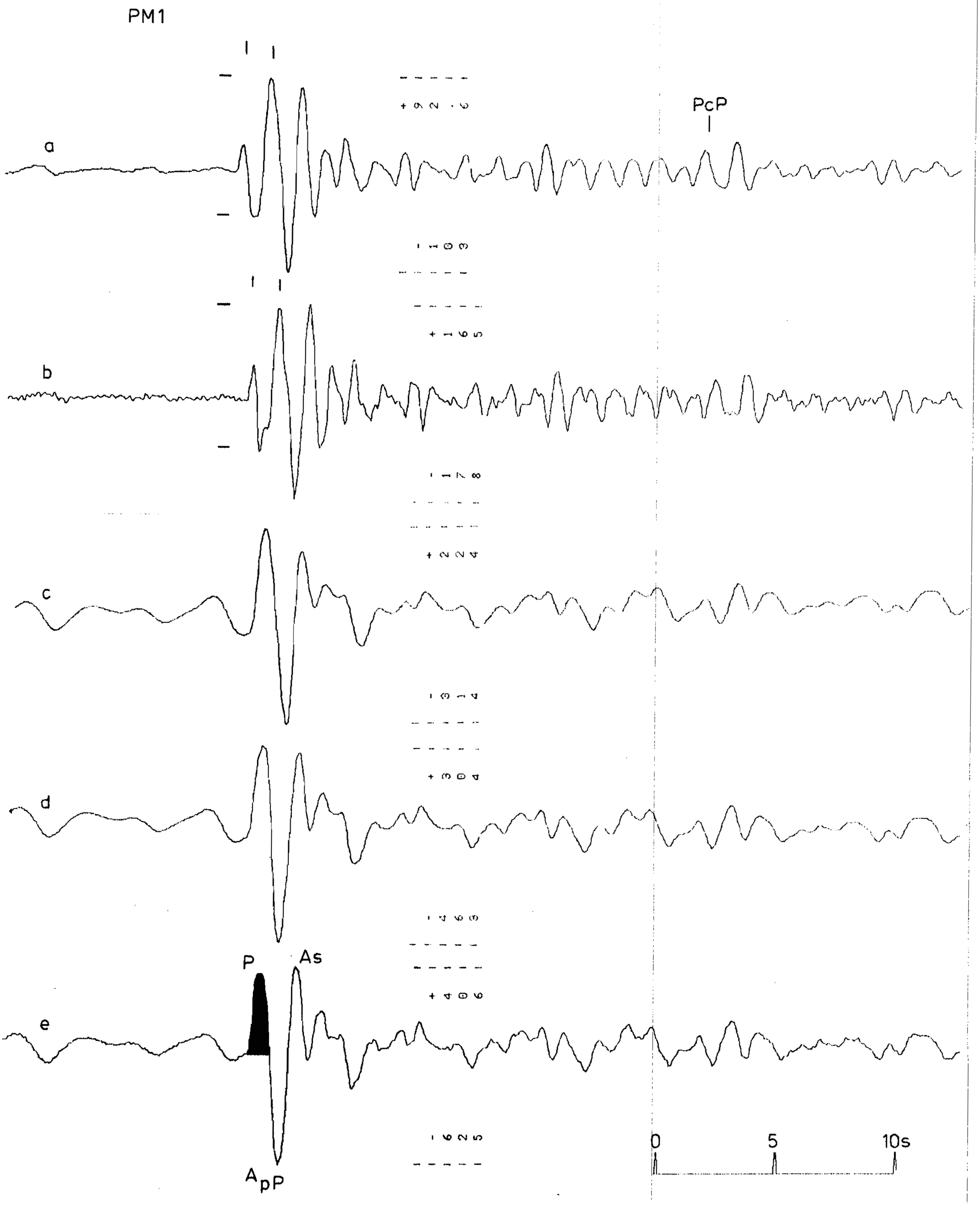

FIGURE 19. P SEISMOGRAMS RECORDED AT ESKDALEMUIR, SCOTLAND FROM NTS EXPLOSION HALFBEAK

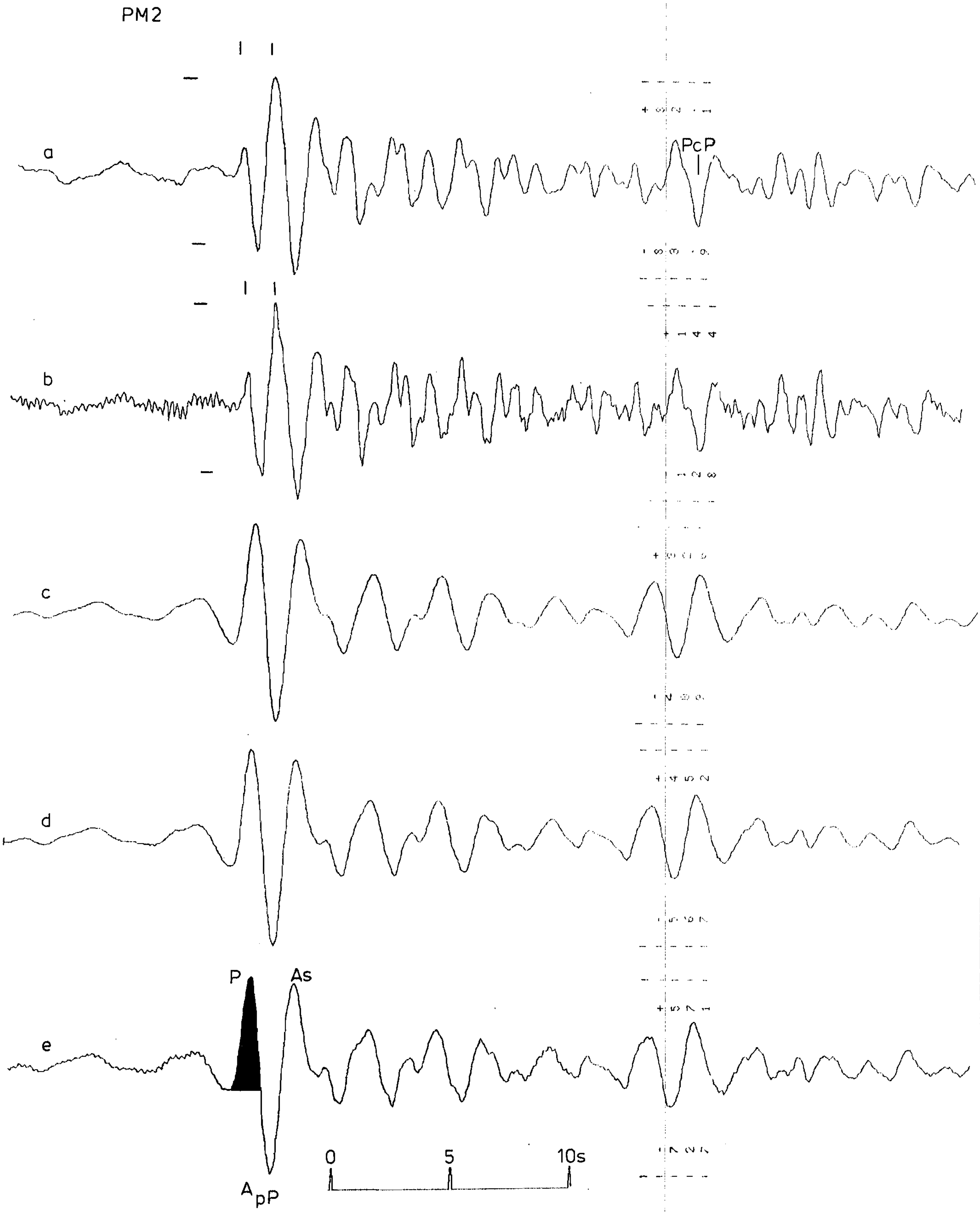

FIGURE 20. P SEISMOGRAMS RECORDED AT ESKDALEMUIR, SCOTLAND FROM NTS EXPLOSION GREELEY

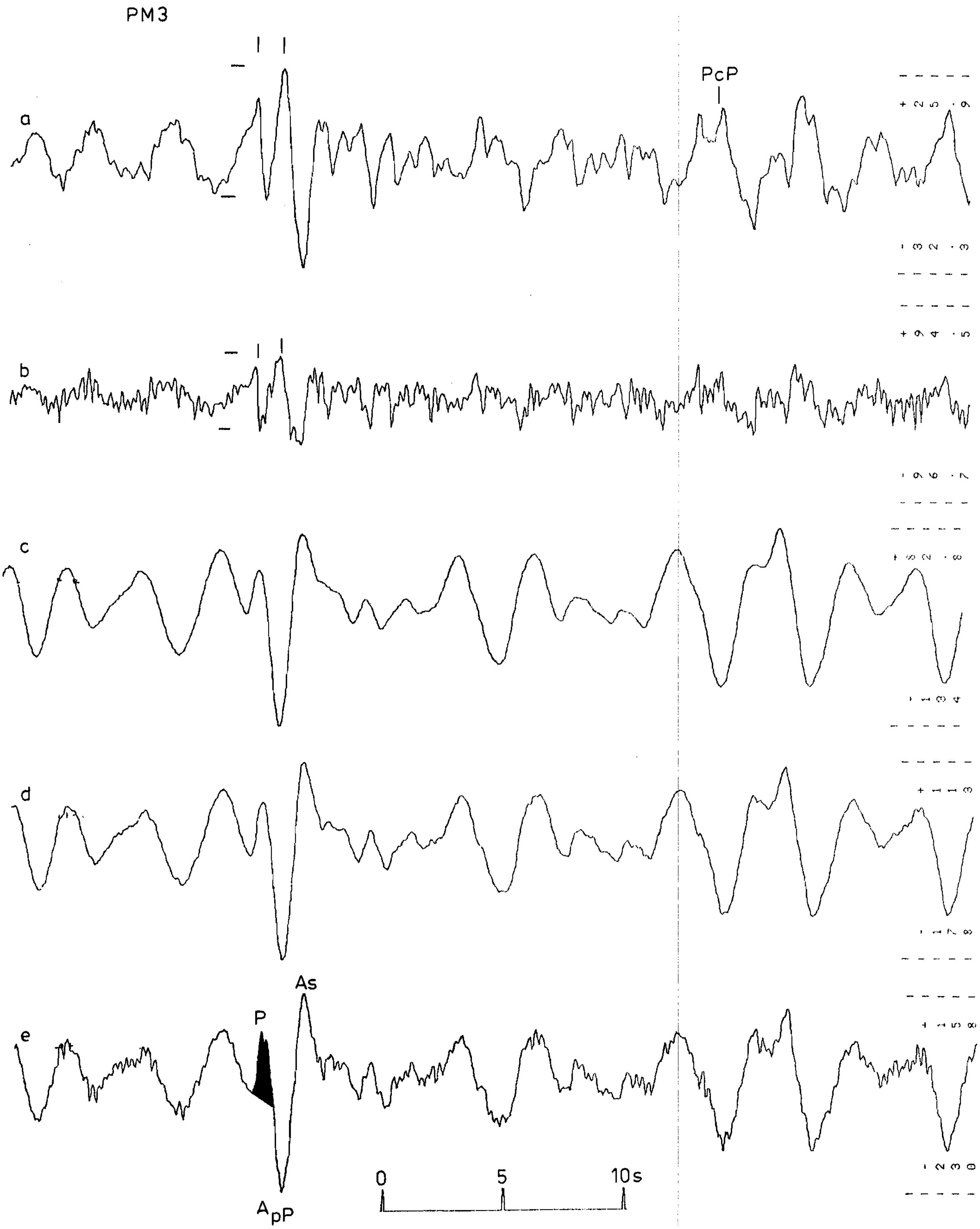

FIGURE 21. P SEISMOGRAMS RECORDED AT ESKDALEMUIR, SCOTLAND FROM NTS EXPLOSION SCOTCH

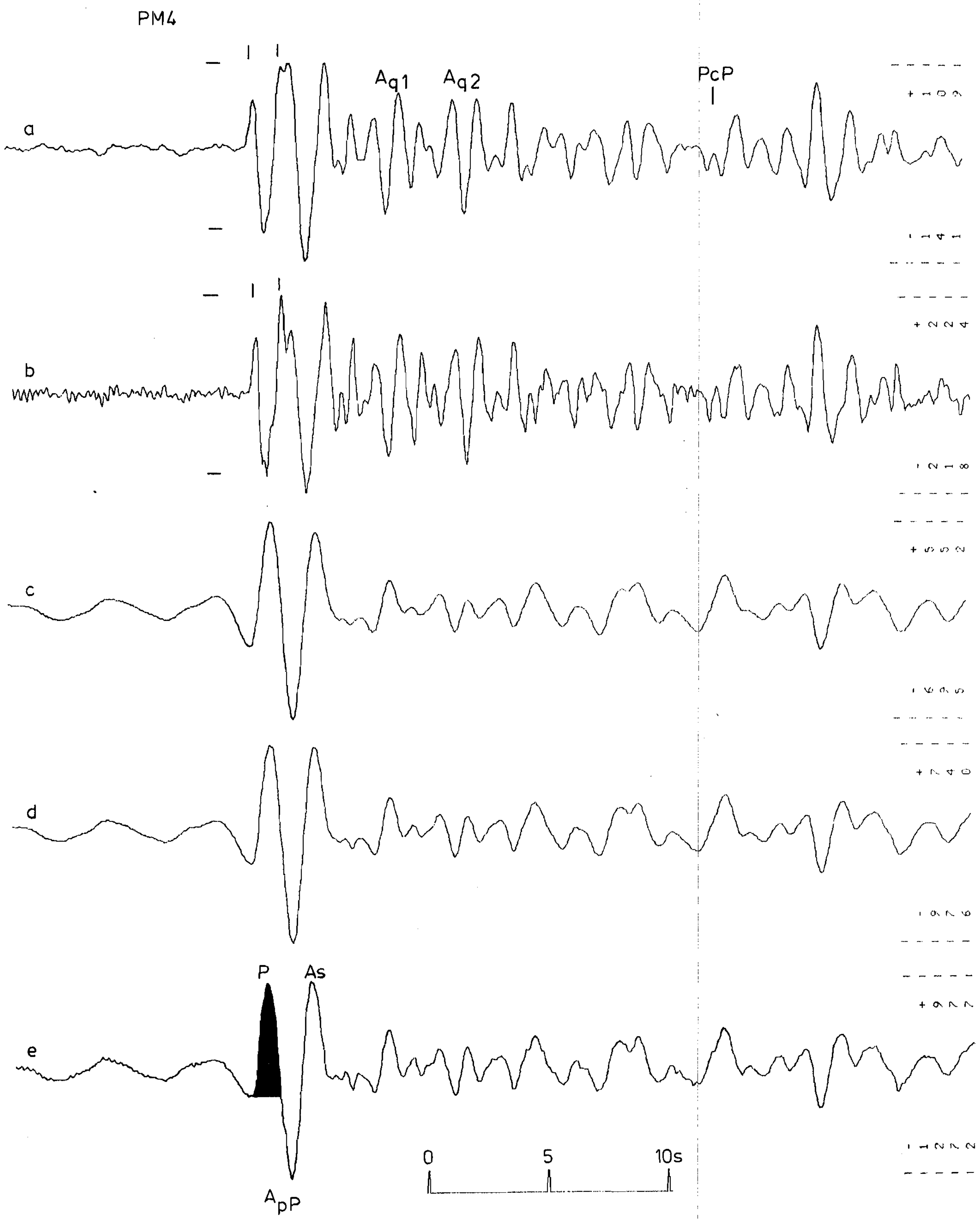

FIGURE 22. P SEISMOGRAMS RECORDED AT ESKDALEMUIR, SCOTLAND FROM NTS EXPLOSION BOXCAR

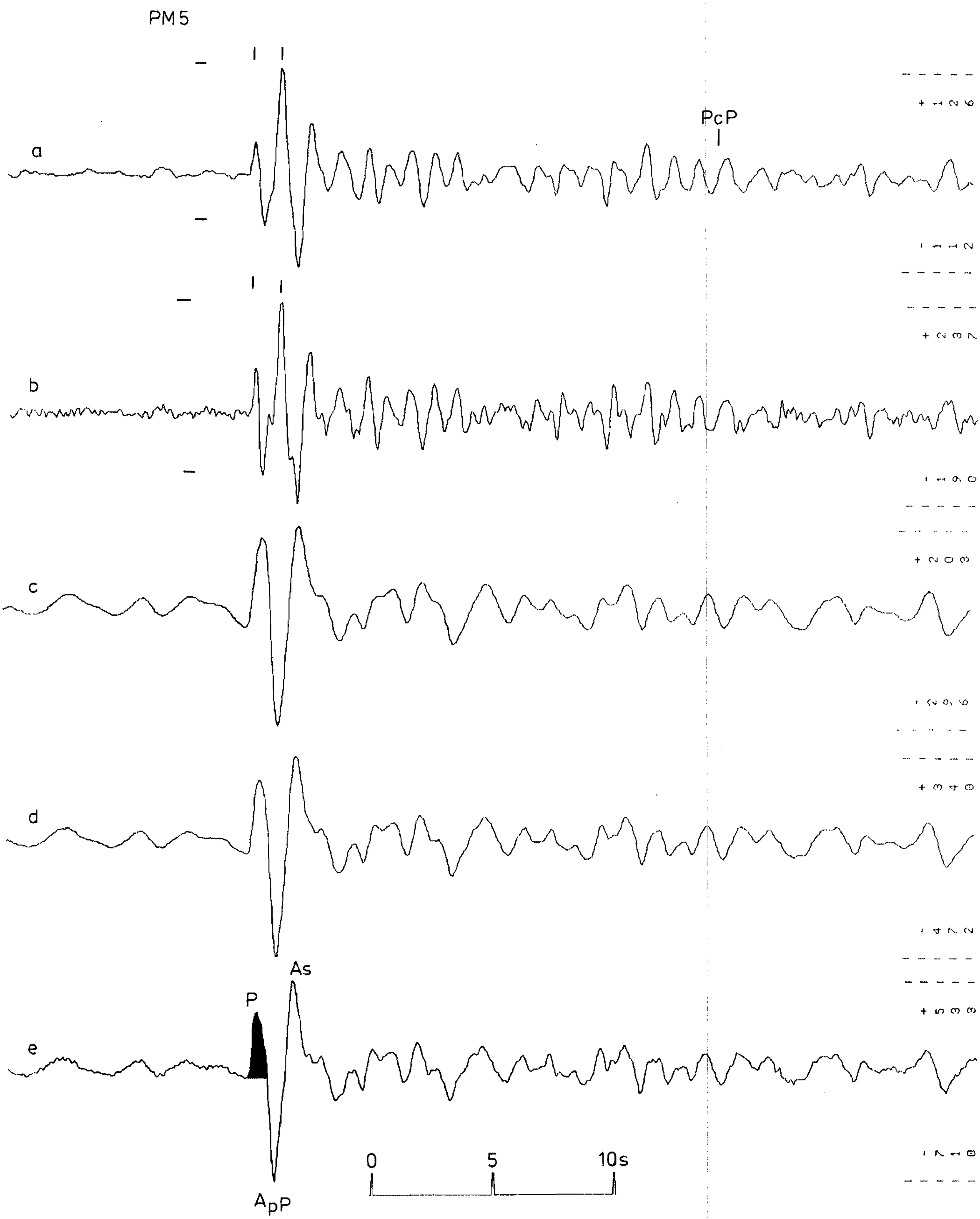

FIGURE 23. P SEISMOGRAMS RECORDED AT ESKDALEMUIR, SCOTLAND FROM NTS EXPLOSION SLED

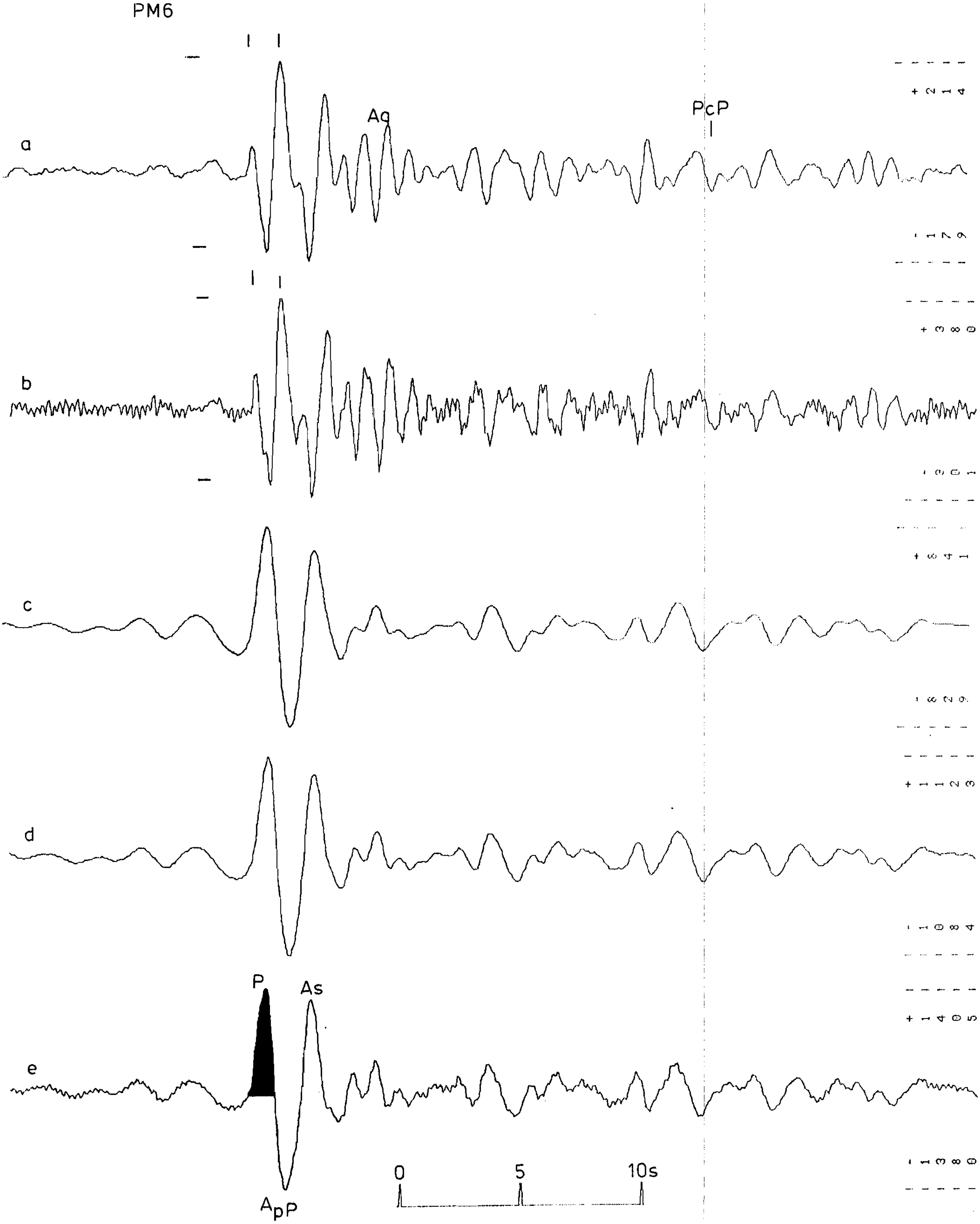

FIGURE 24. P SEISMOGRAMS RECORDED AT ESKDALEMUIR, SCOTLAND FROM NTS EXPLOSION BENHAM

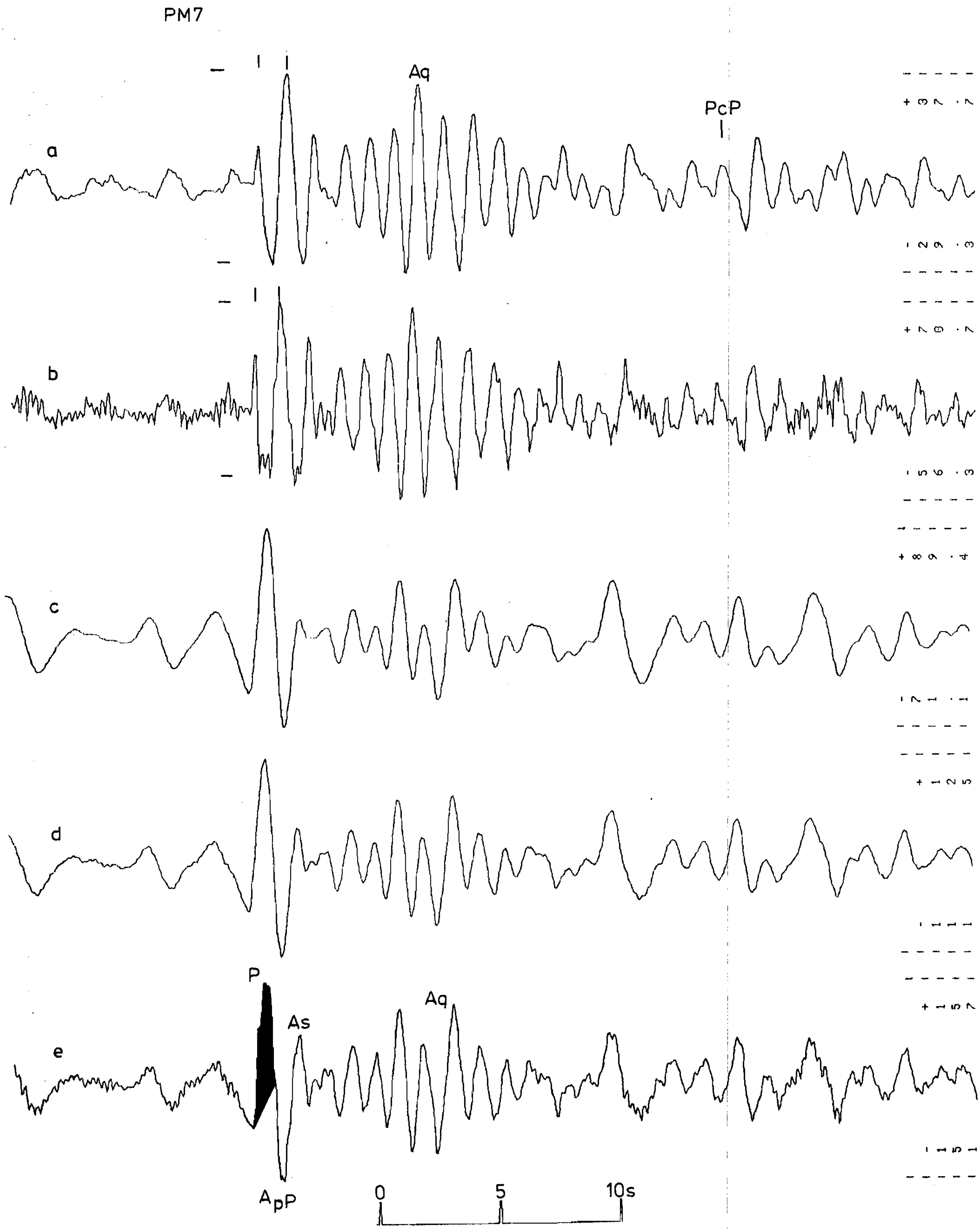

FIGURE 25. P SEISMOGRAMS RECORDED AT ESKDALEMUIR, SCOTLAND FROM NTS EXPLOSION PURSE

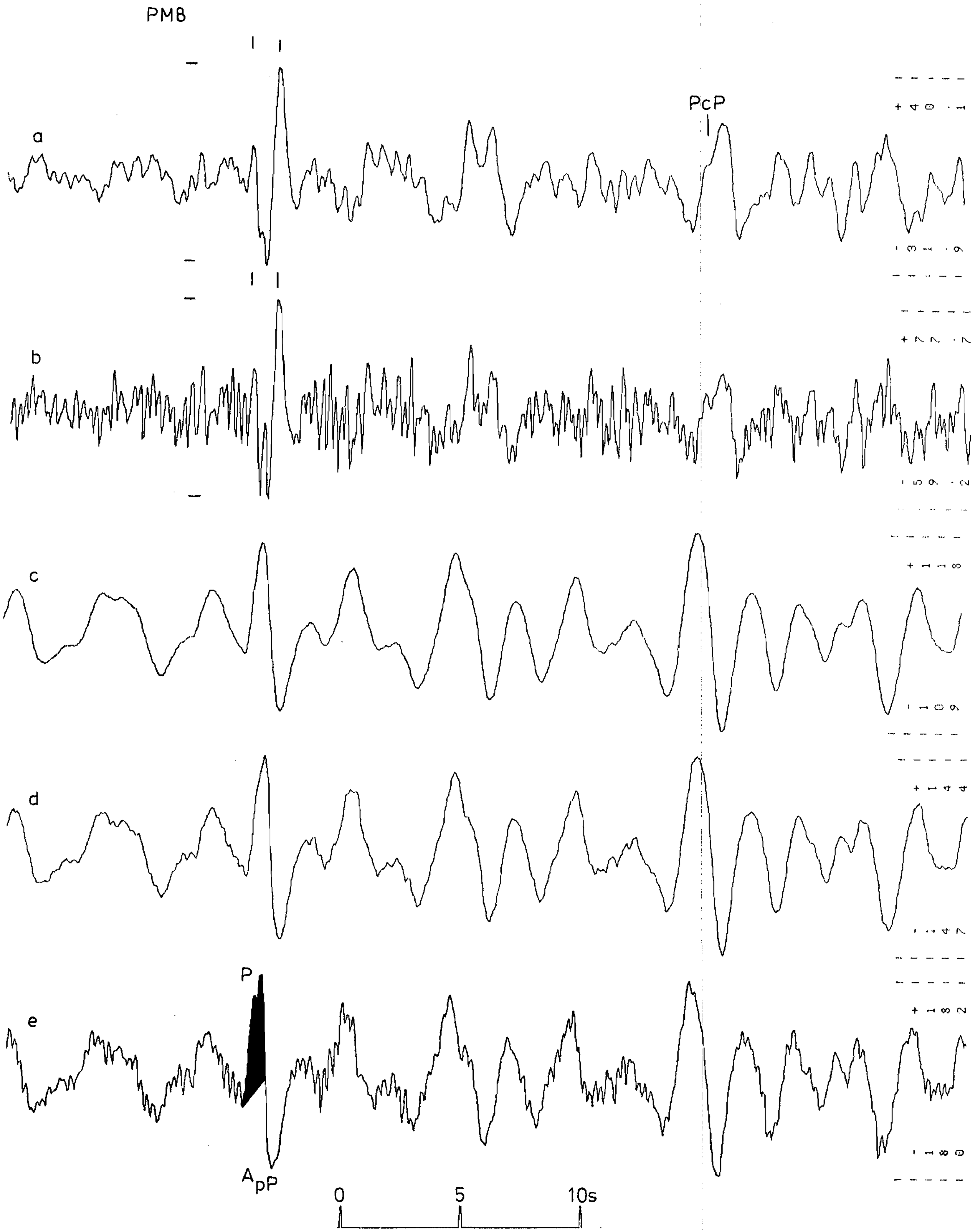

FIGURE 26. P SEISMOGRAMS RECORDED AT ESKDALEMUIR, SCOTLAND FROM NTS EXPLOSION PIPKIN

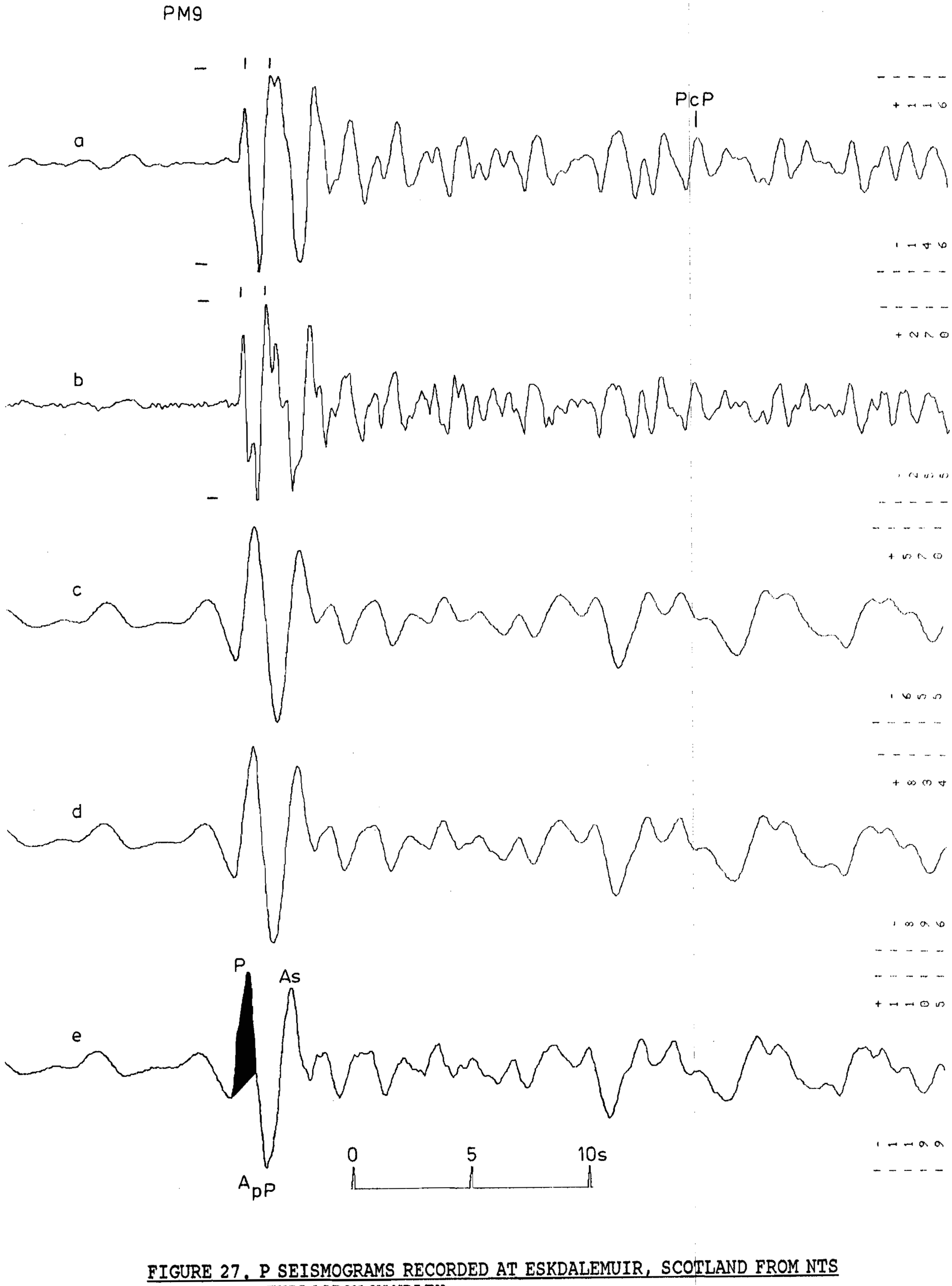

FIGURE 27. P SEISMOGRAMS RECORDED AT ESKDALEMUIR, SCOTLAND FROM NTS EXPLOSION HANDLEY

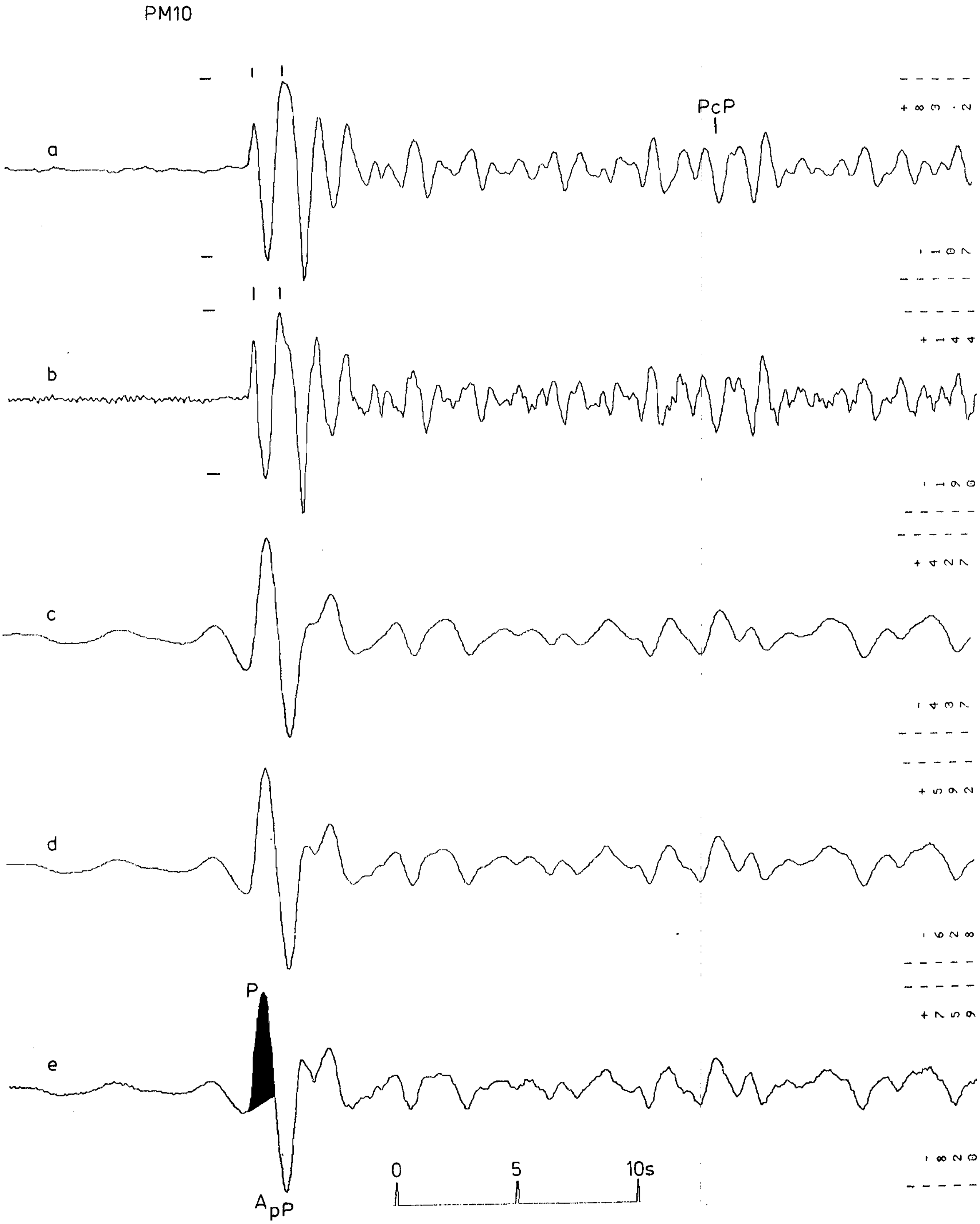

FIGURE 28. P SEISMOGRAMS RECORDED AT ESKDALEMUIR, SCOTLAND FROM NTS EXPLOSION ALMENDRO

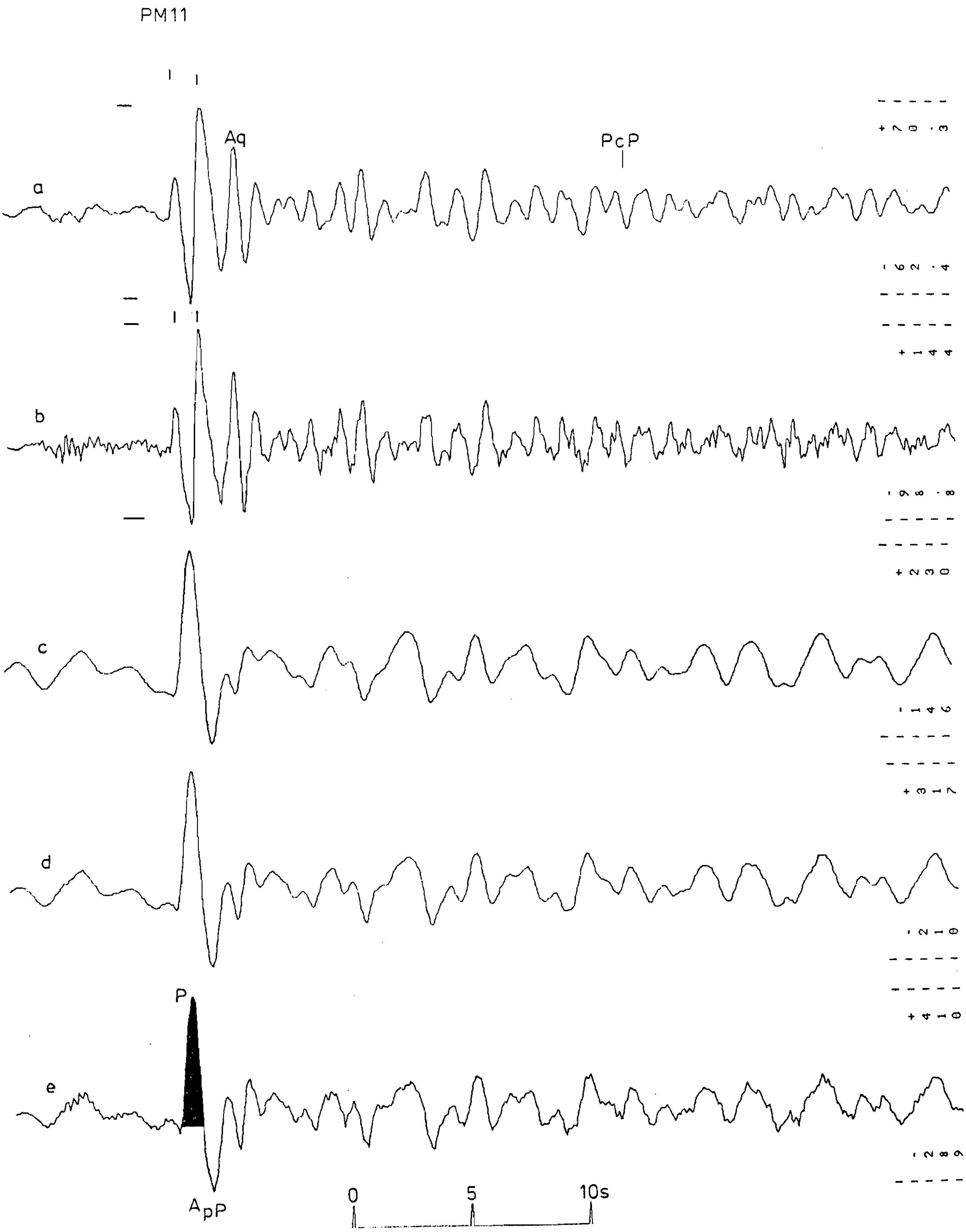

FIGURE 29. P SEISMOGRAMS RECORDED AT ESKDALEMUIR, SCOTLAND FROM NTS EXPLOSION TYBO

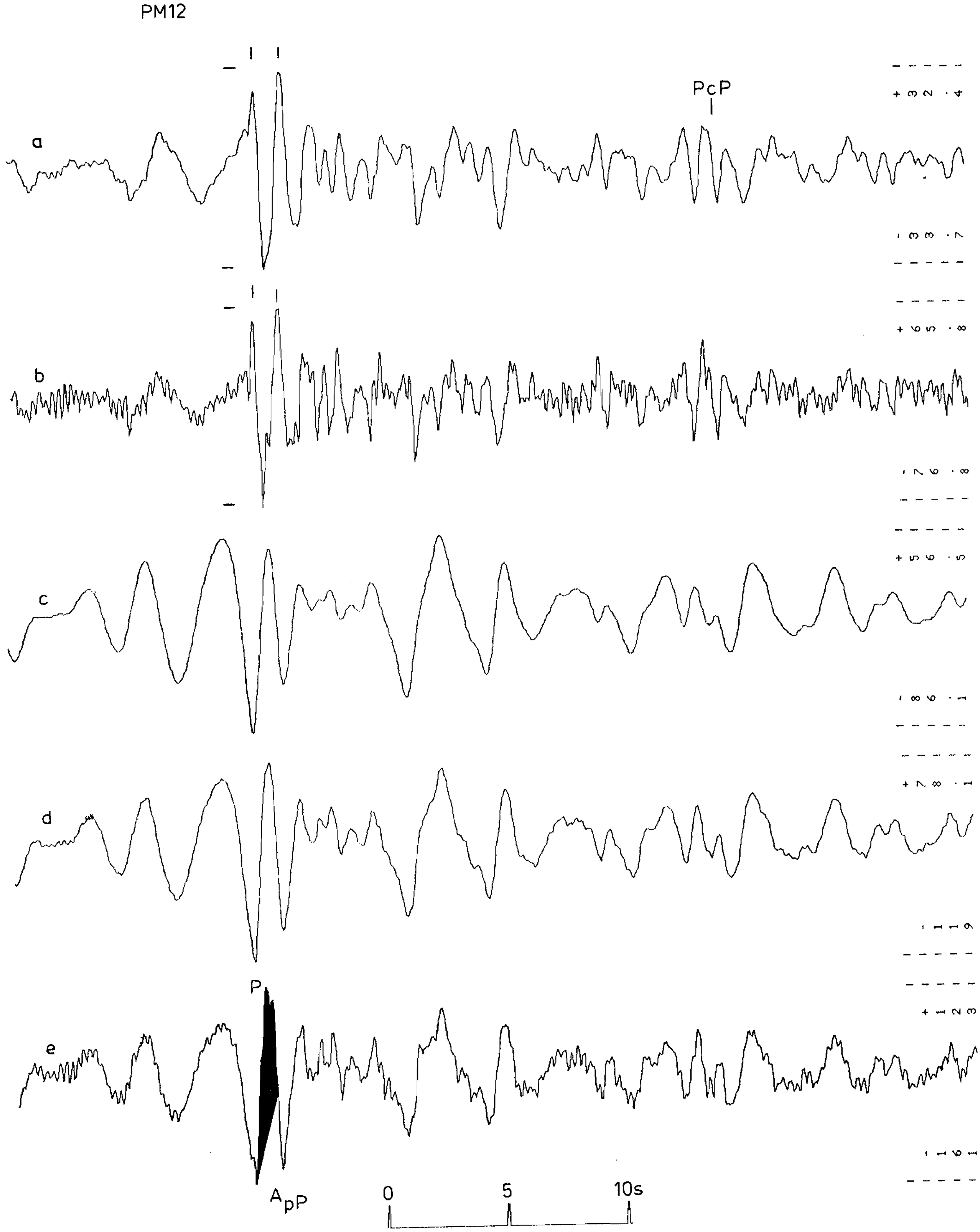

FIGURE 30. P SEISMOGRAMS RECORDED AT ESKDALEMUIR, SCOTLAND FROM NTS EXPLOSION STILTON

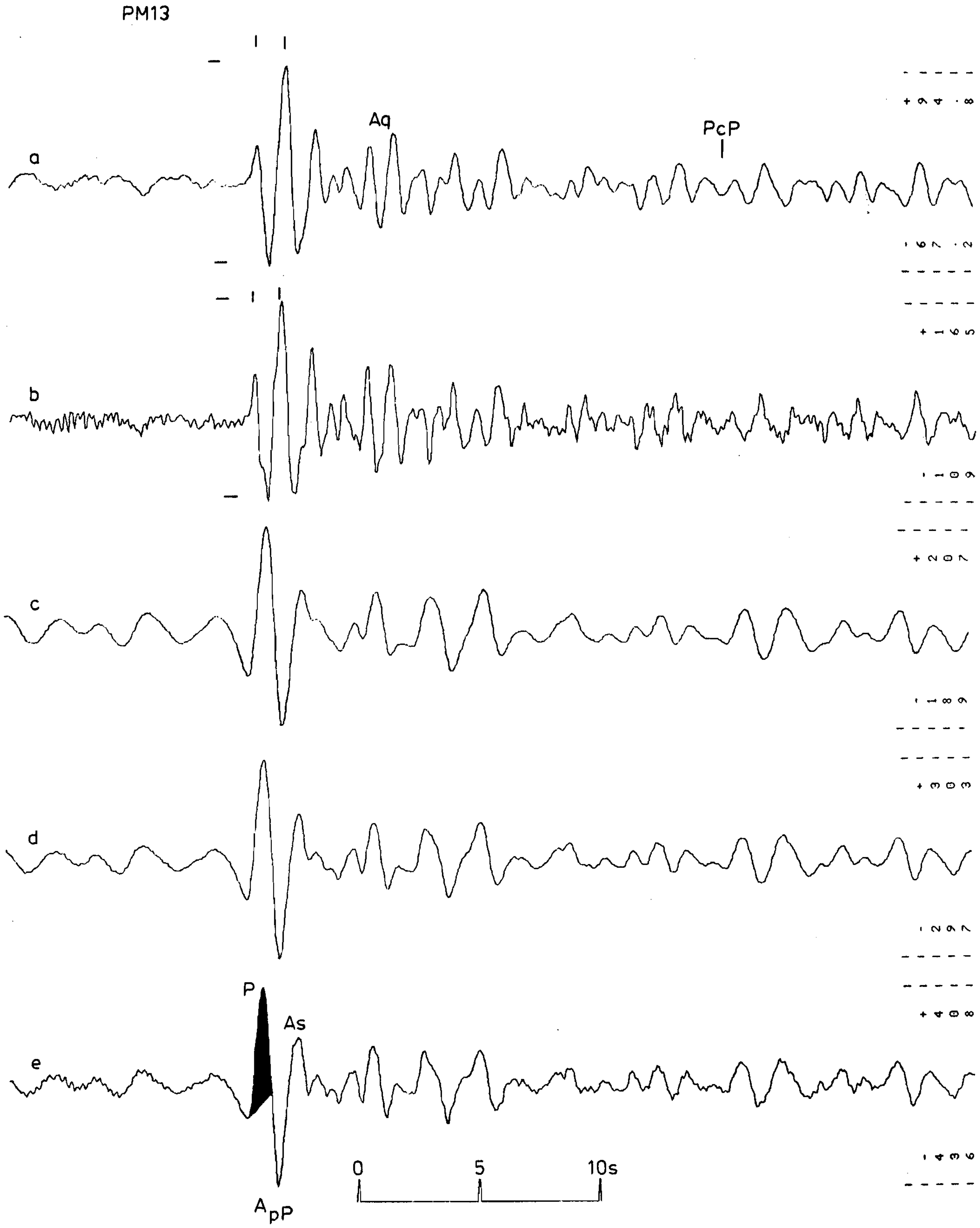

FIGURE 31. P SEISMOGRAMS RECORDED AT ESKDALEMUIR, SCOTLAND FROM NTS EXPLOSION MAST

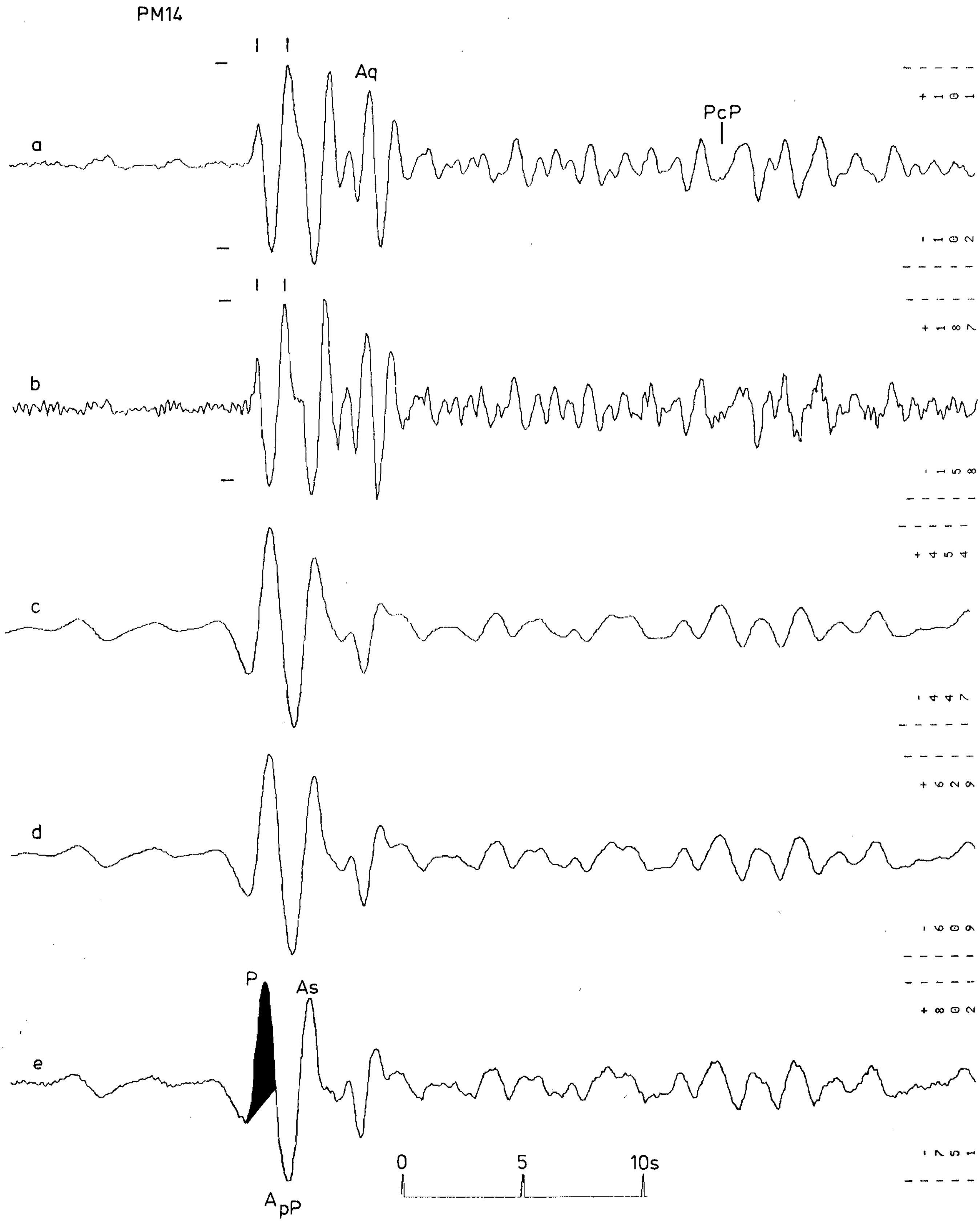

FIGURE 32. P SEISMOGRAMS RECORDED AT ESKDALEMUIR, SCOTLAND FROM NTS EXPLOSION CAMEMBERT

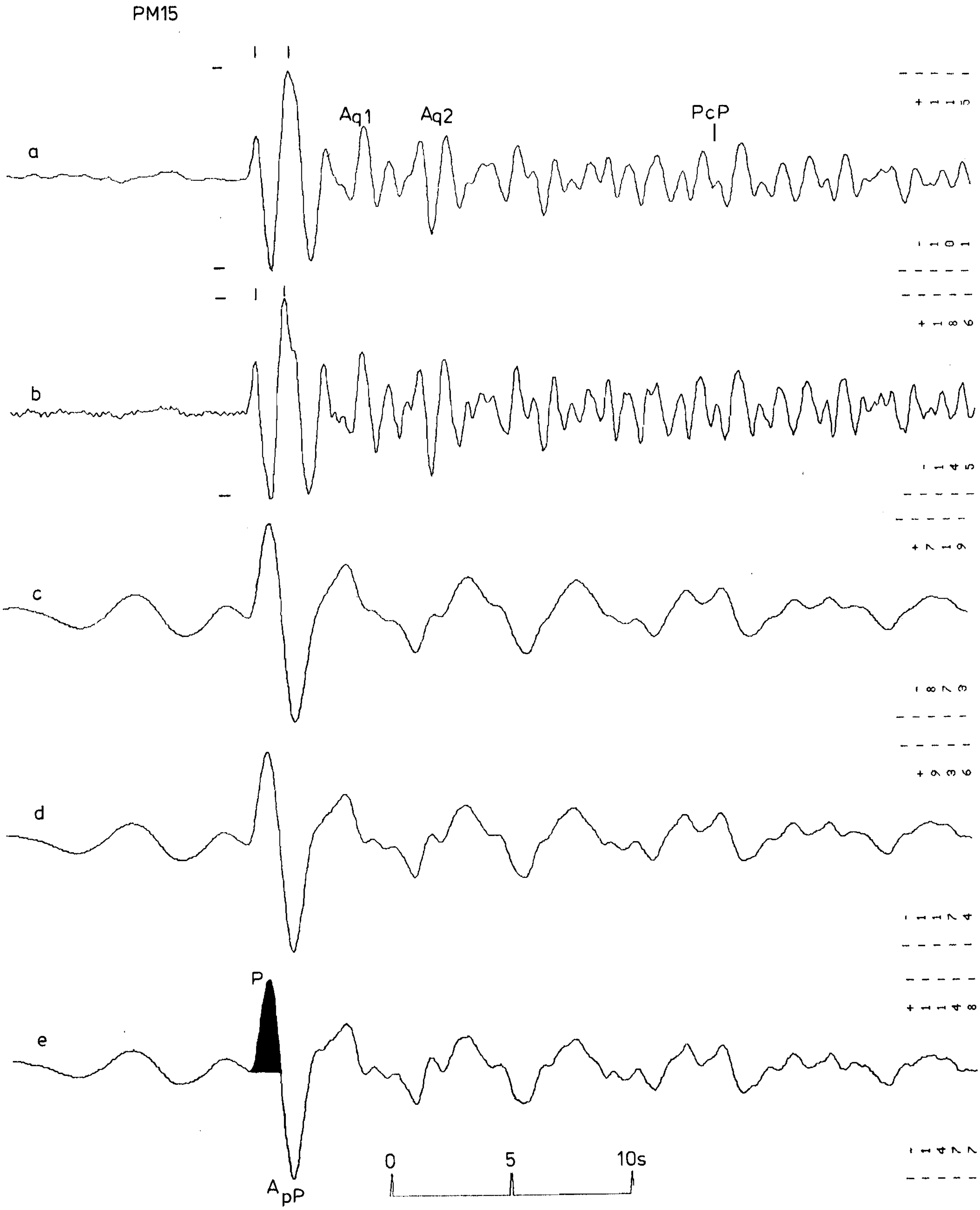

FIGURE 33. P SEISMOGRAMS RECORDED AT ESKDALEMUIR, SCOTLAND FROM NTS EXPLOSION KASSERI

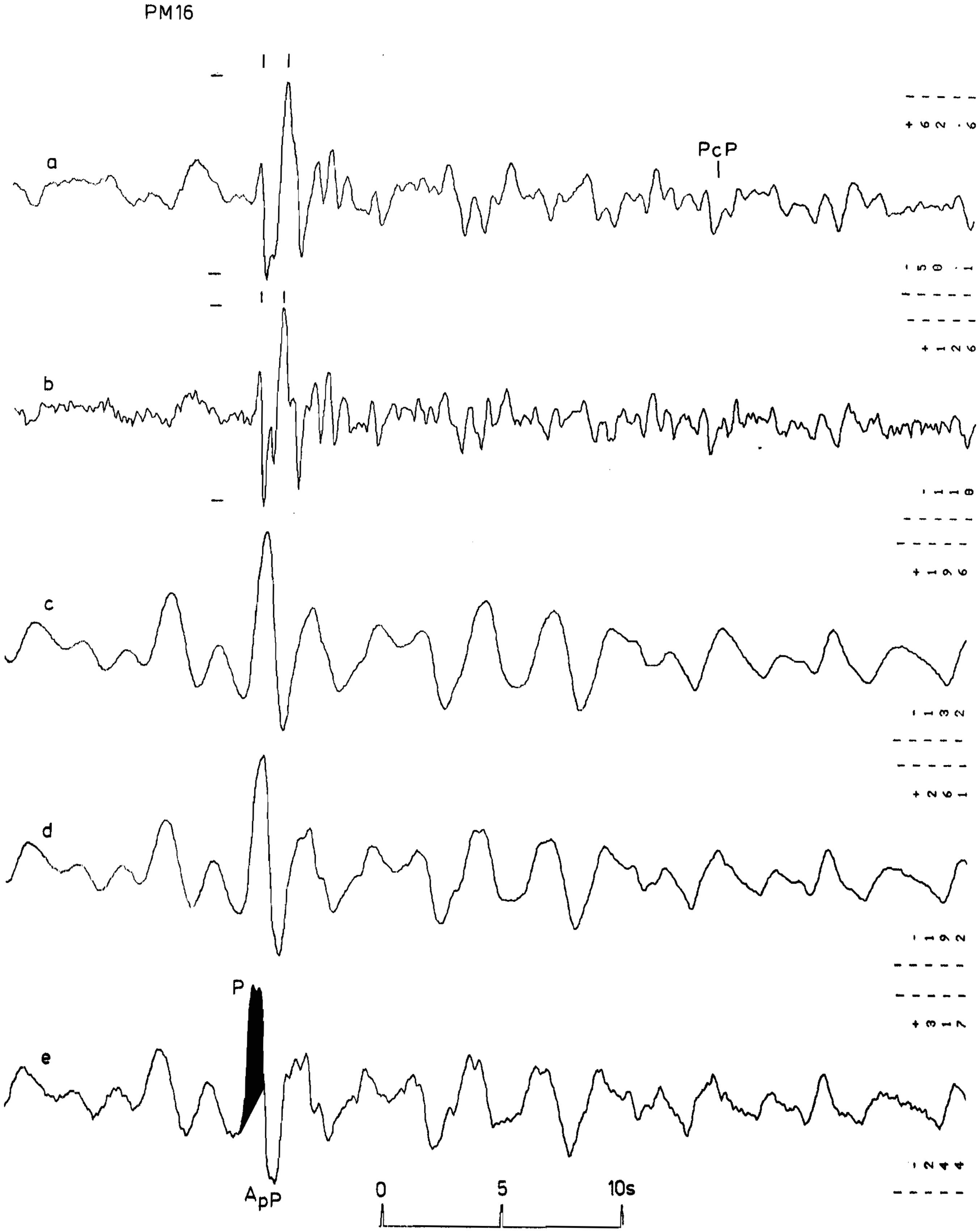

FIGURE 34. P SEISMOGRAMS RECORDED AT ESKDALEMUIR, SCOTLAND FROM NTS EXPLOSION INLET

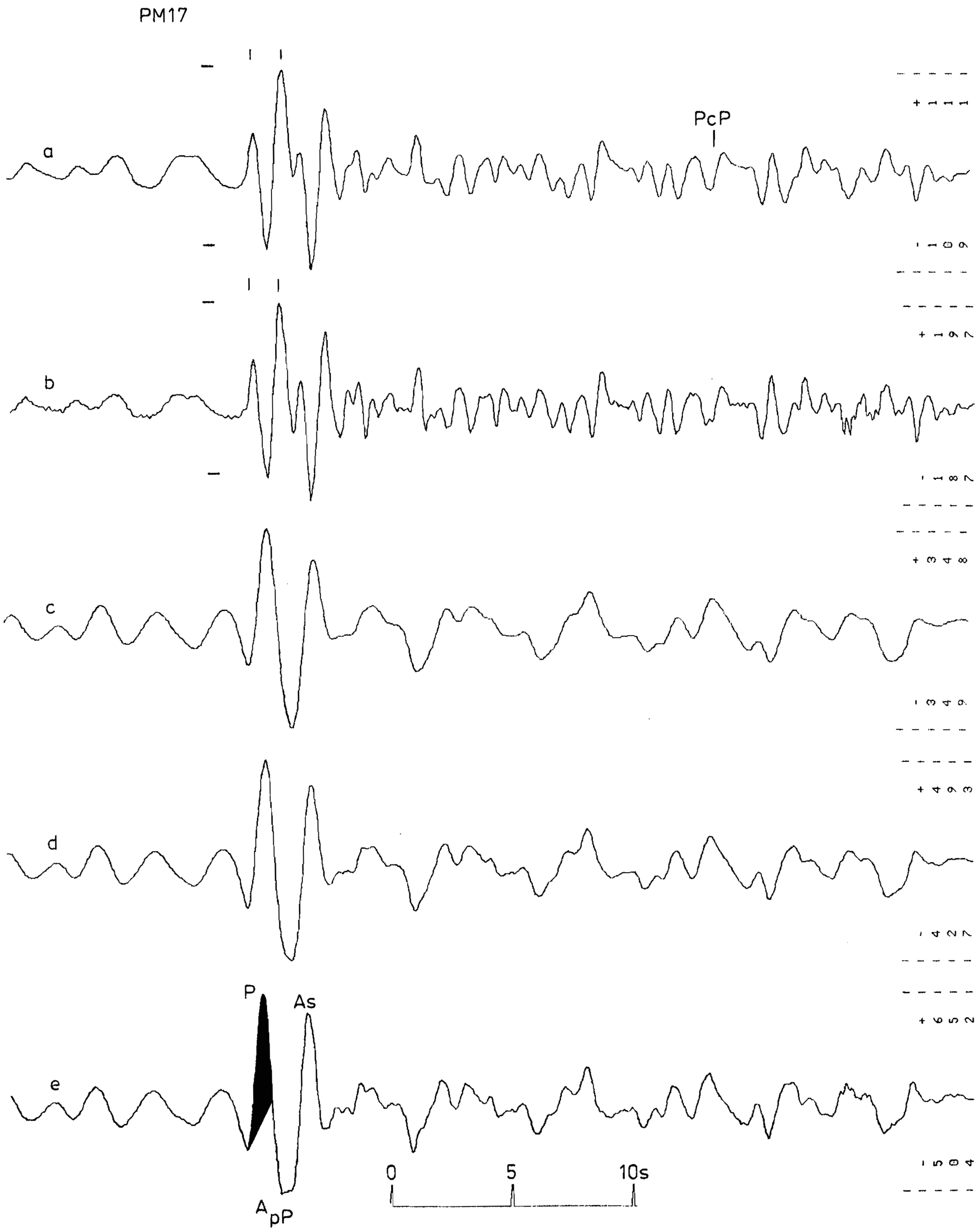

FIGURE 35. P SEISMOGRAMS RECORDED AT ESKDALEMUIR, SCOTLAND FROM NTS EXPLOSION MUENSTER

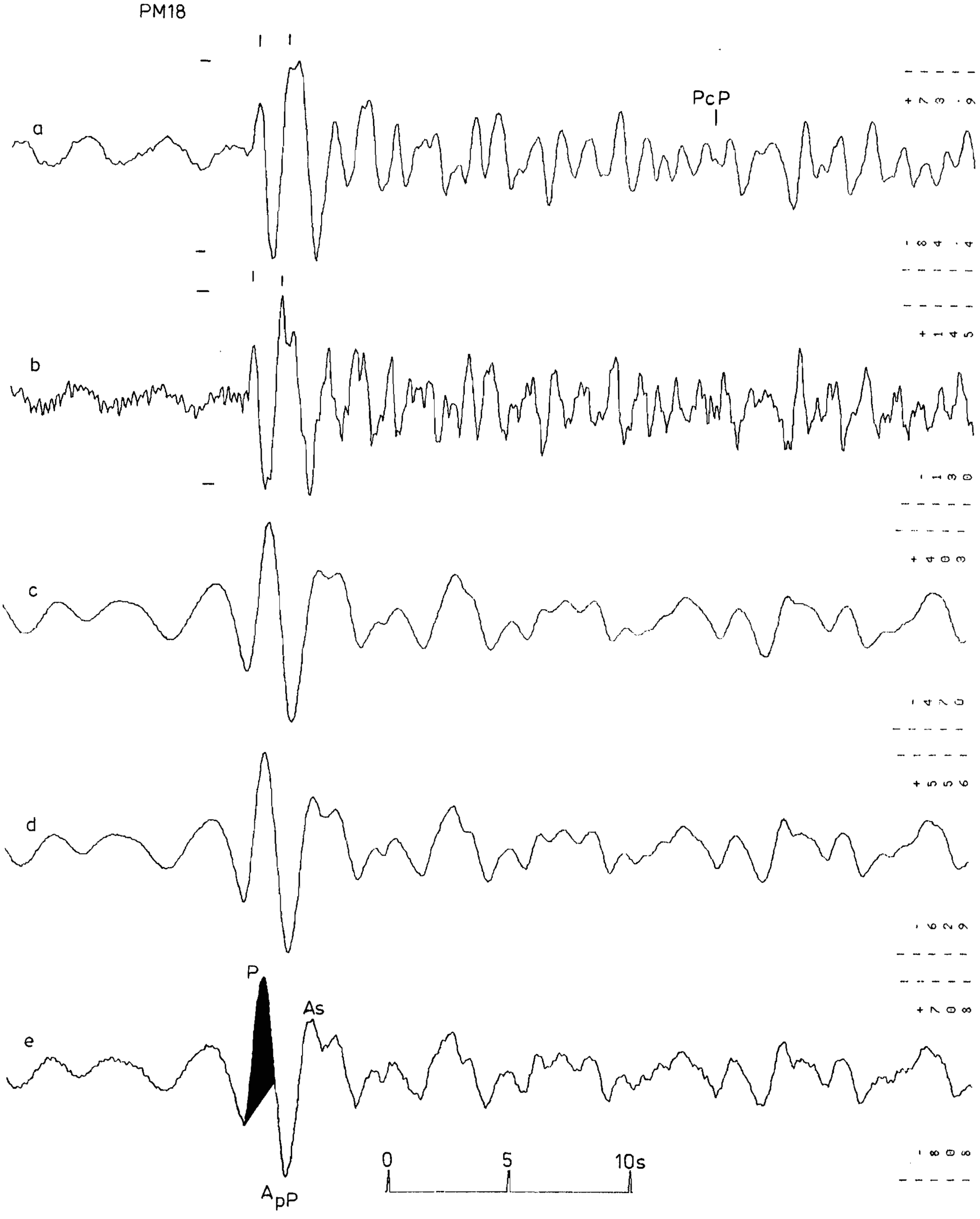

FIGURE 36. P SEISMOGRAMS RECORDED AT ESKDALEMUIR, SCOTLAND FROM NTS EXPLOSION FONTINA

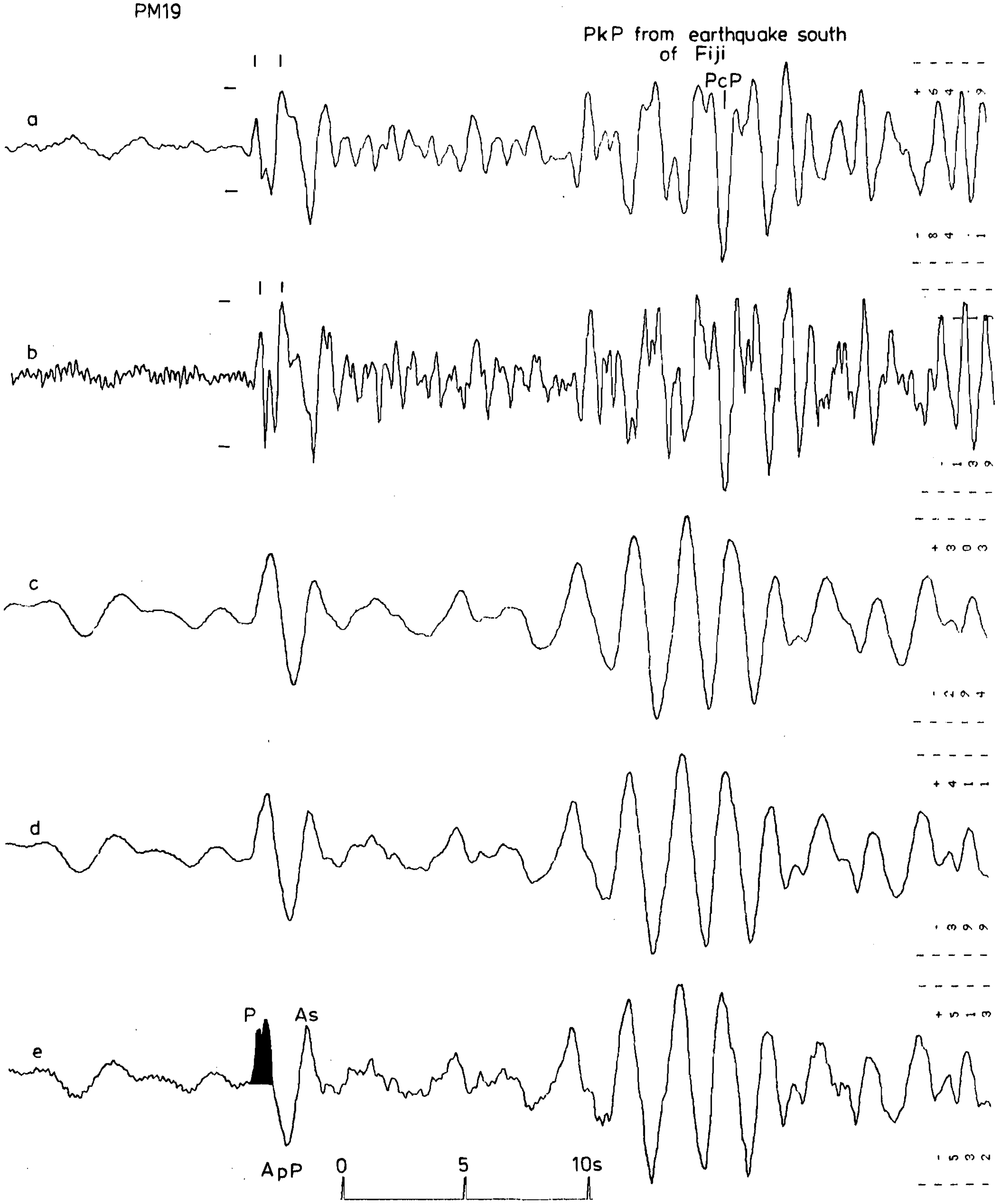

FIGURE 37. P SEISMOGRAMS RECORDED AT ESKDALEMUIR, SCOTLAND FROM NTS EXPLOSION CHESHIRE

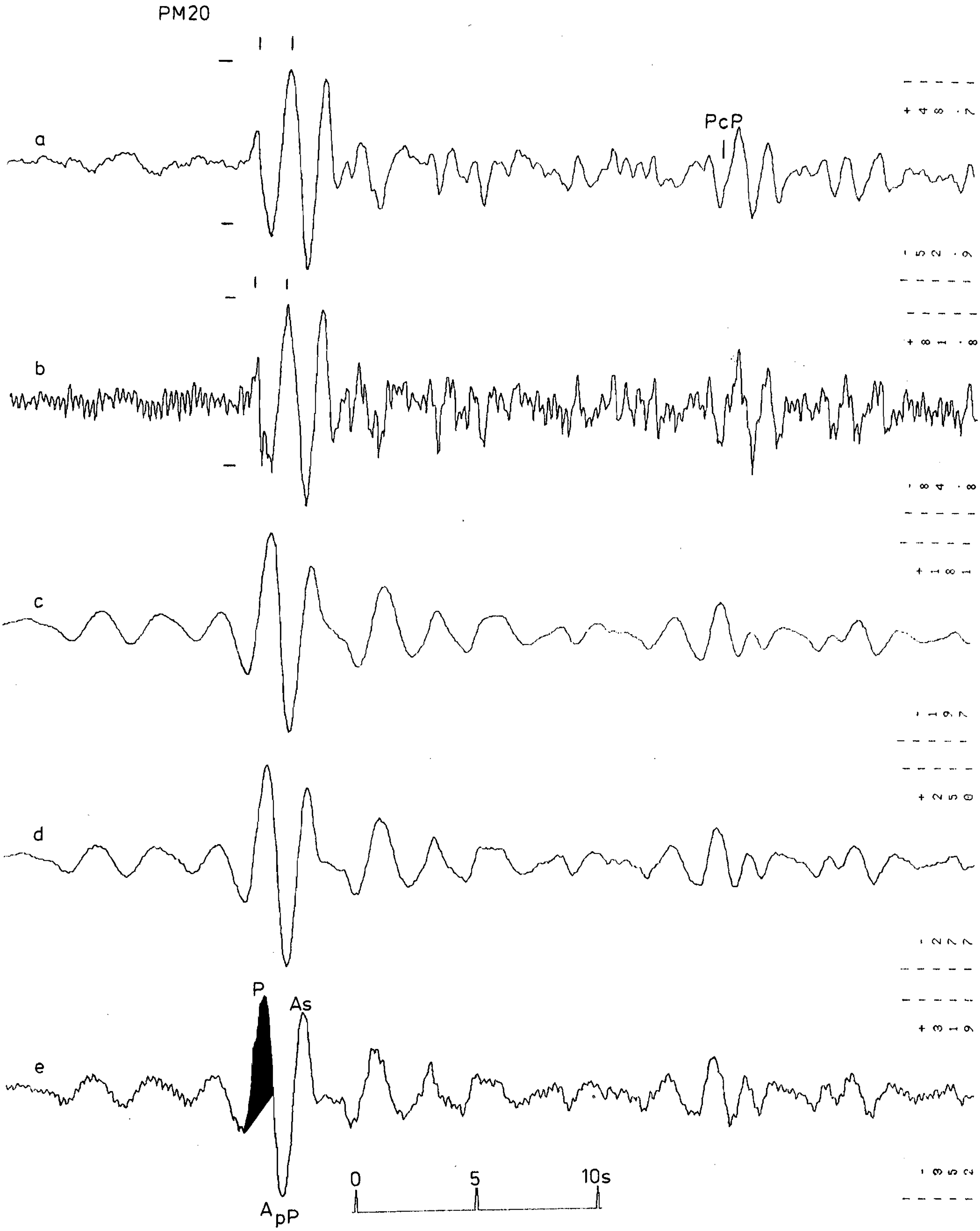

FIGURE 38. P SEISMOGRAMS RECORDED AT ESKDALEMUIR, SCOTLAND FROM NTS EXPLOSION ESTUARY

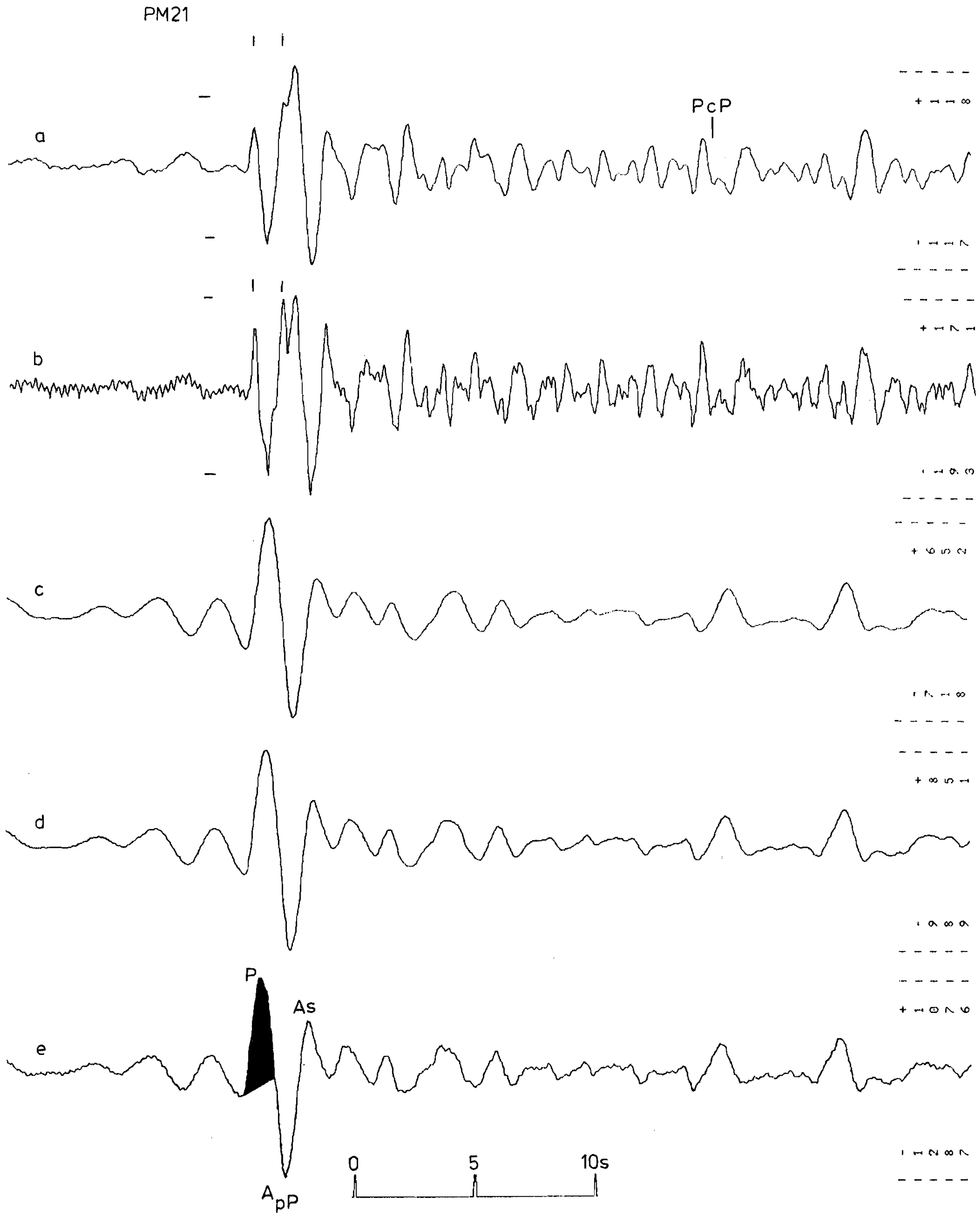

FIGURE 39. P SEISMOGRAMS RECORDED AT ESKDALEMUIR, SCOTLAND FROM NTS EXPLOSION COLBY

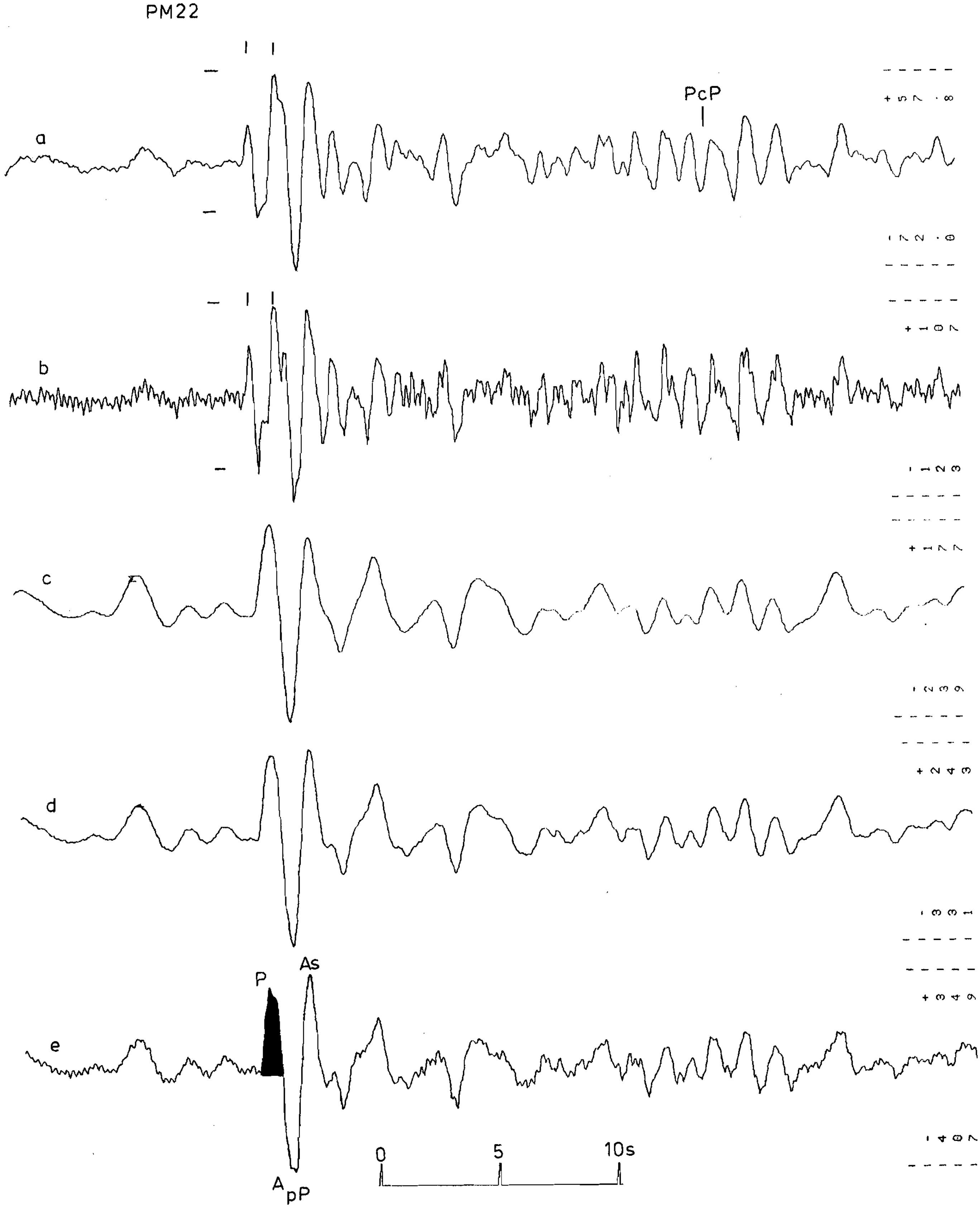

FIGURE 40. P SEISMOGRAMS RECORDED AT ESKDALEMUIR, SCOTLAND FROM NTS EXPLOSION POOL

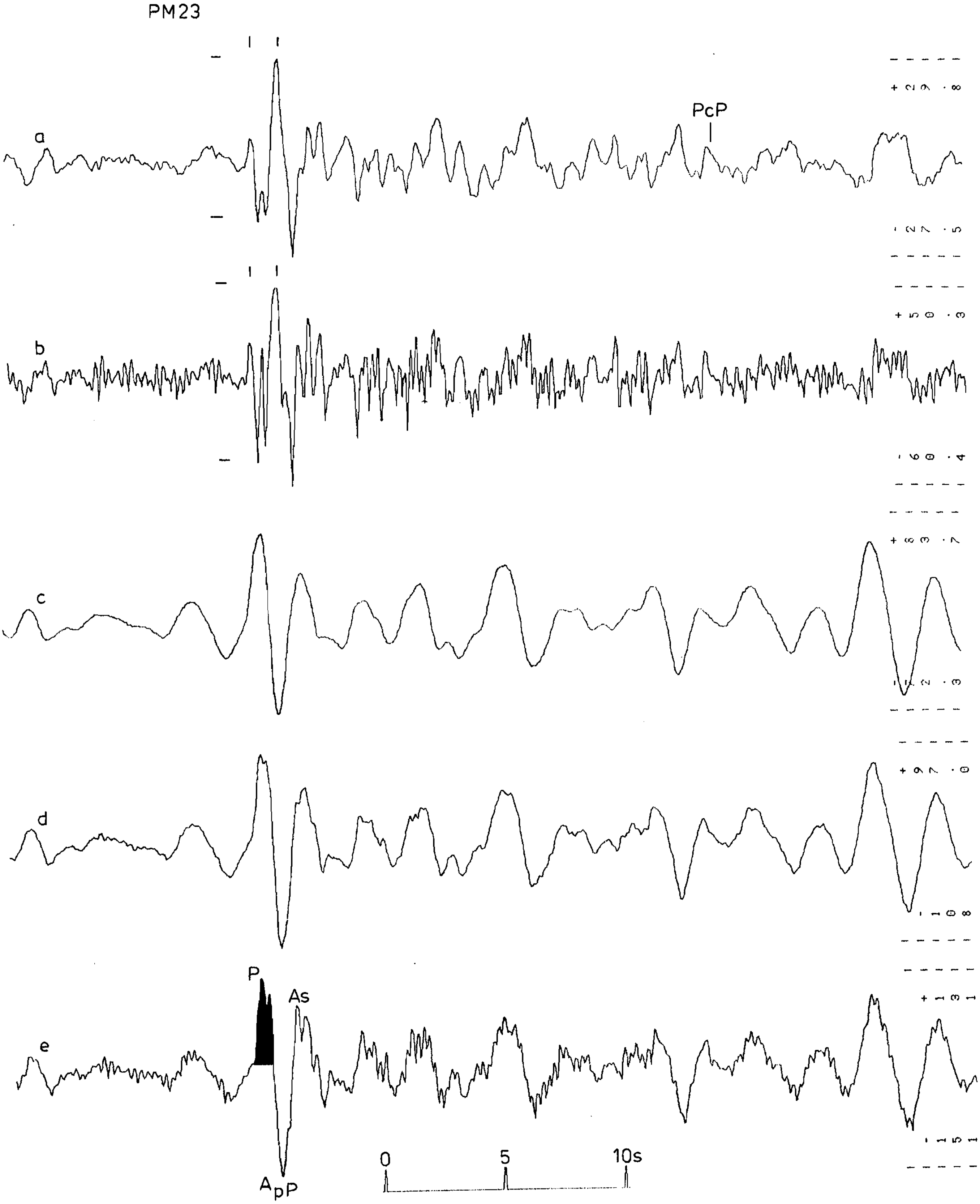

FIGURE 41. P SEISMOGRAMS RECORDED AT ESKDALEMUIR, SCOTLAND FROM NTS EXPLOSION BACKBEACH

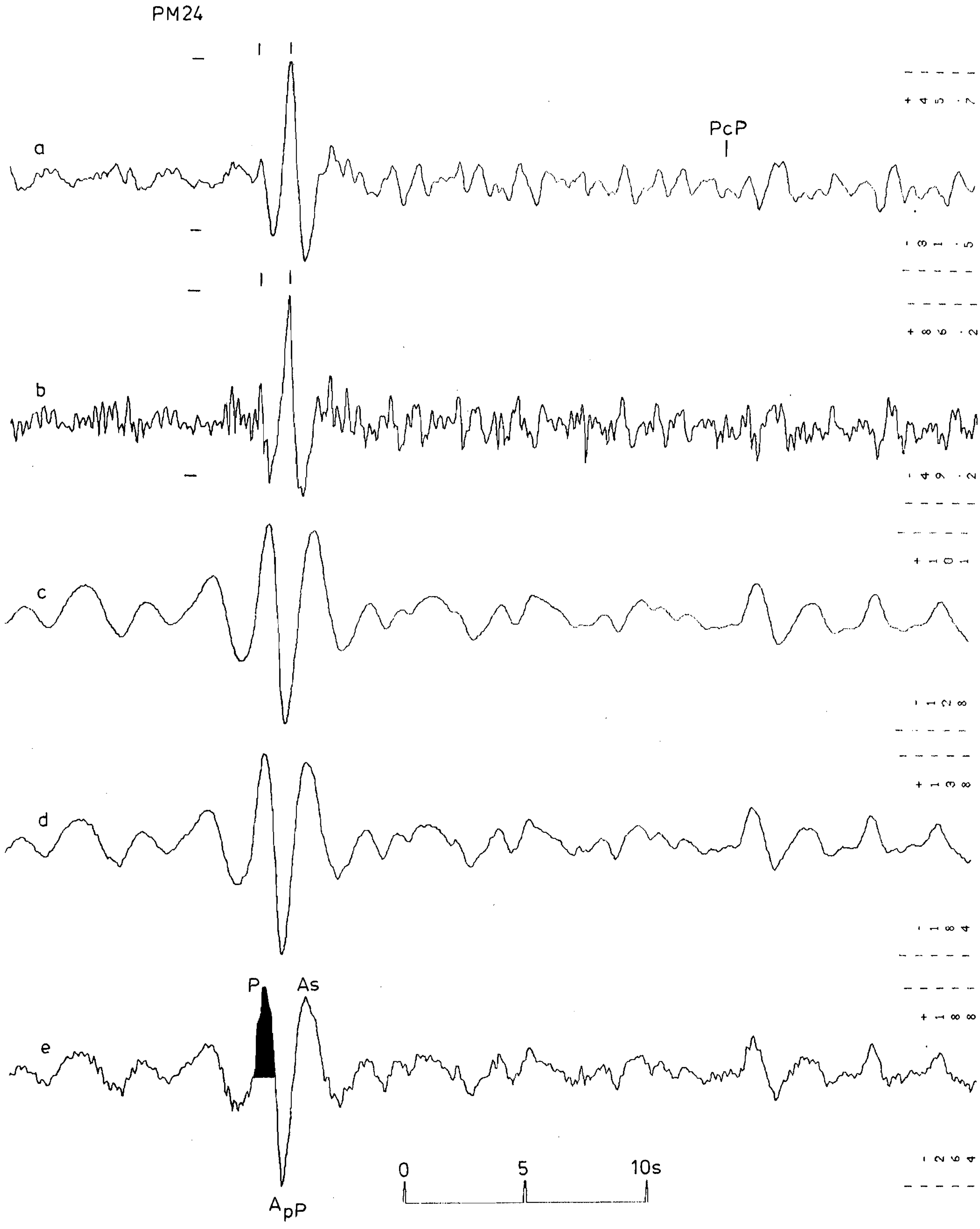

FIGURE 42. P SEISMOGRAMS RECORDED AT ESKDALEMUIR, SCOTLAND FROM NTS EXPLOSION PANIR

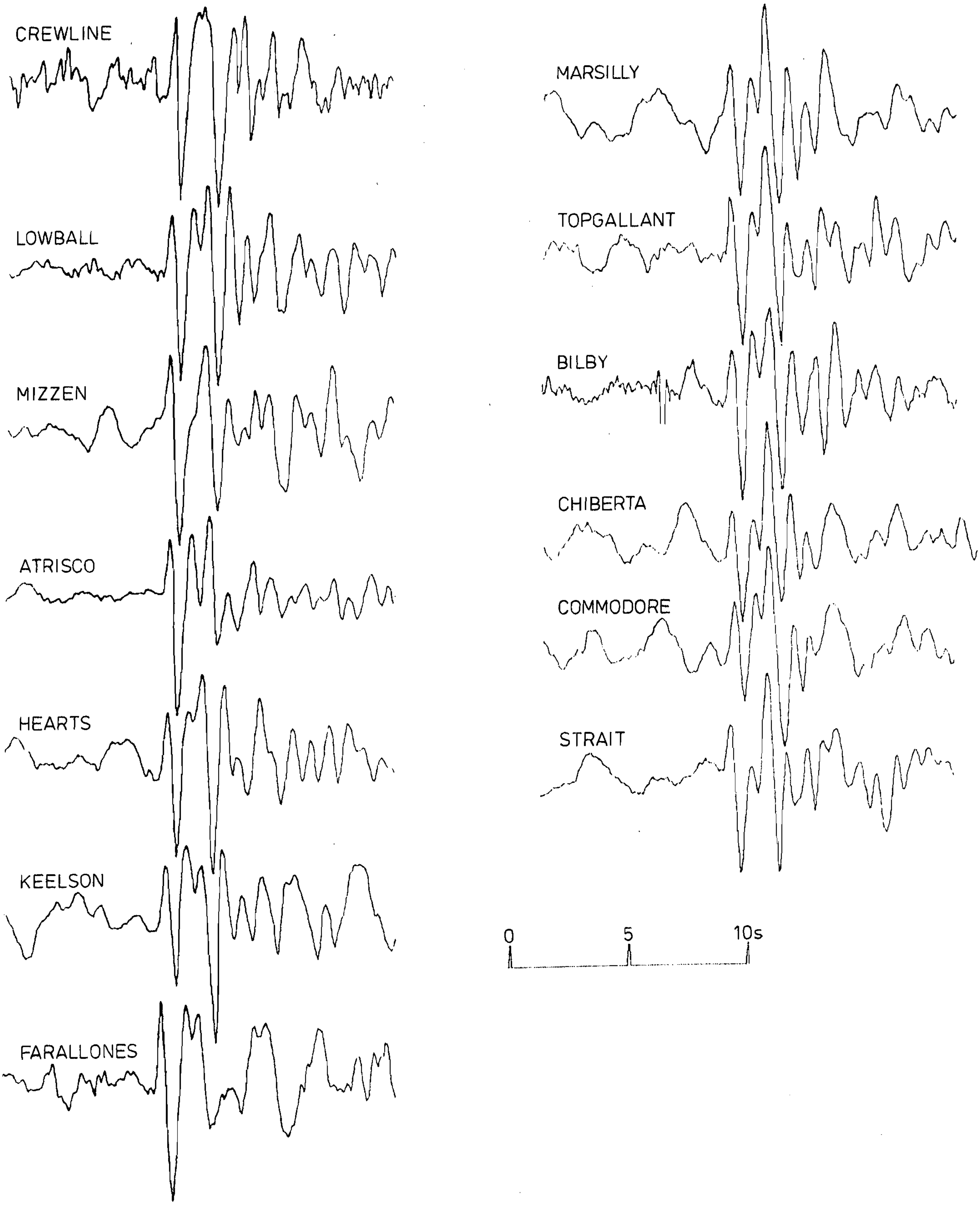

FIGURE 43. THE SHORT-PERIOD SEISMOGRAMS FOR THE YUCCA FLATS EXPLOSIONS ARRANGED IN ORDER OF DEPTH OF FIRING

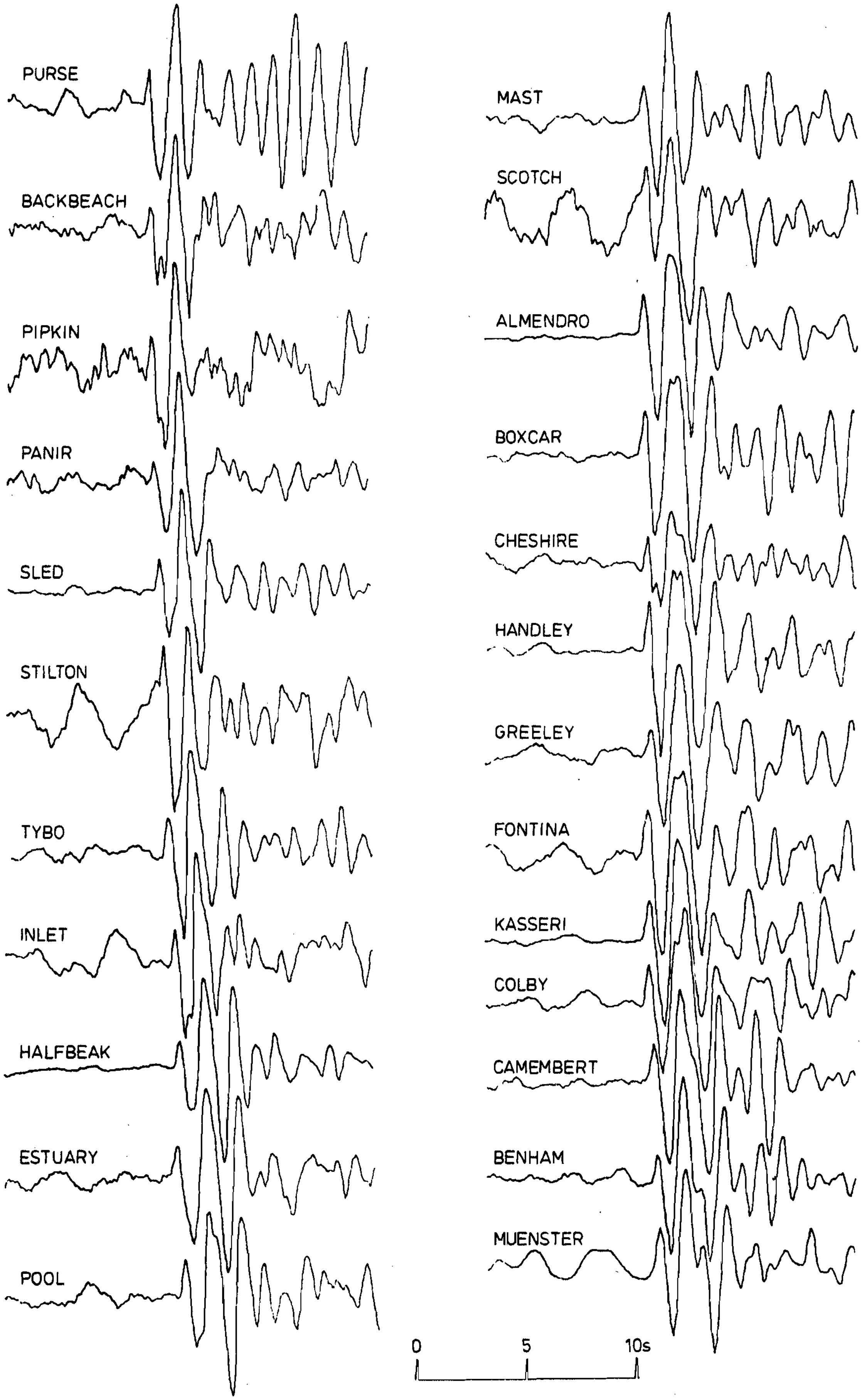

<u>FIGURE 44. THE SHORT-PERIOD SEISMOGRAMS FOR THE PAHUTE MESA EXPLOSIONS ARRANGED IN ORDER OF DEPTH OF FIRING</u>

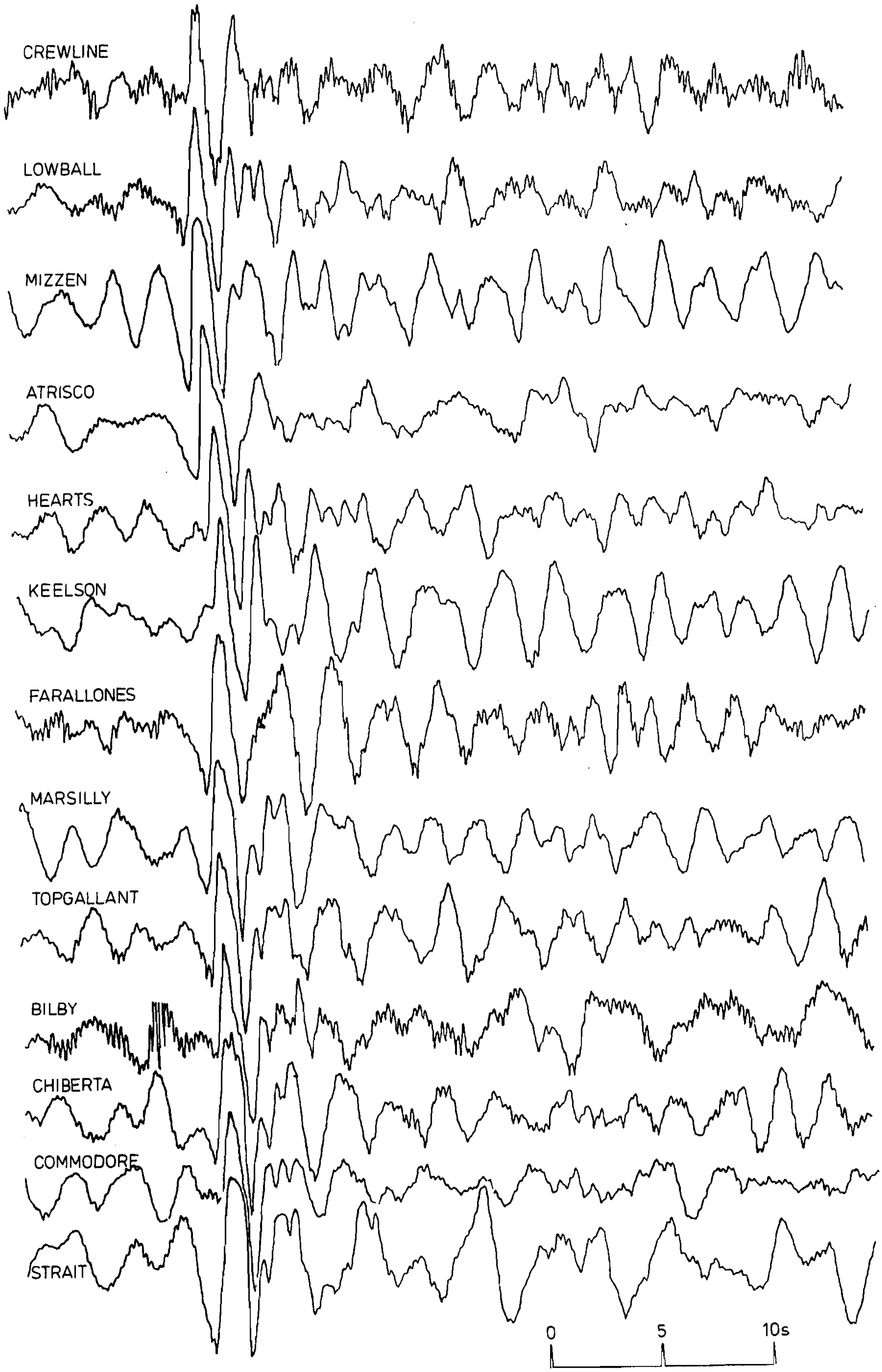

FIGURE 45. THE DECONVOLVED BB SEISMOGRAMS FOR THE YUCCA FLATS EXPLOSIONS ARRANGED IN ORDER OF DEPTH OF FIRING

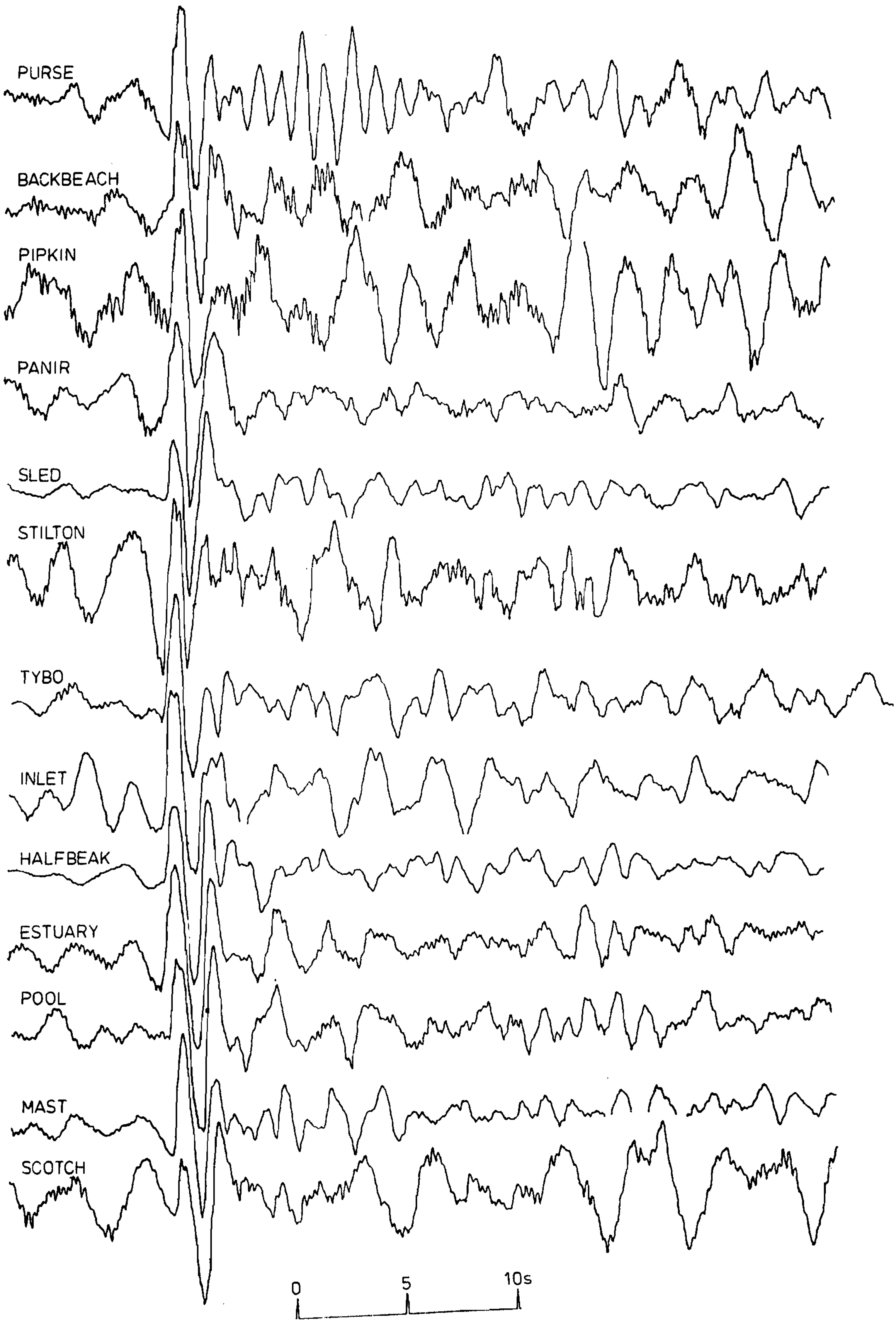

FIGURE 46. THE DECONVOLVED BB SEISMOGRAMS FOR THE PAHUTE MESA EXPLOSIONS ARRANGED IN ORDER OF DEPTH OF FIRING

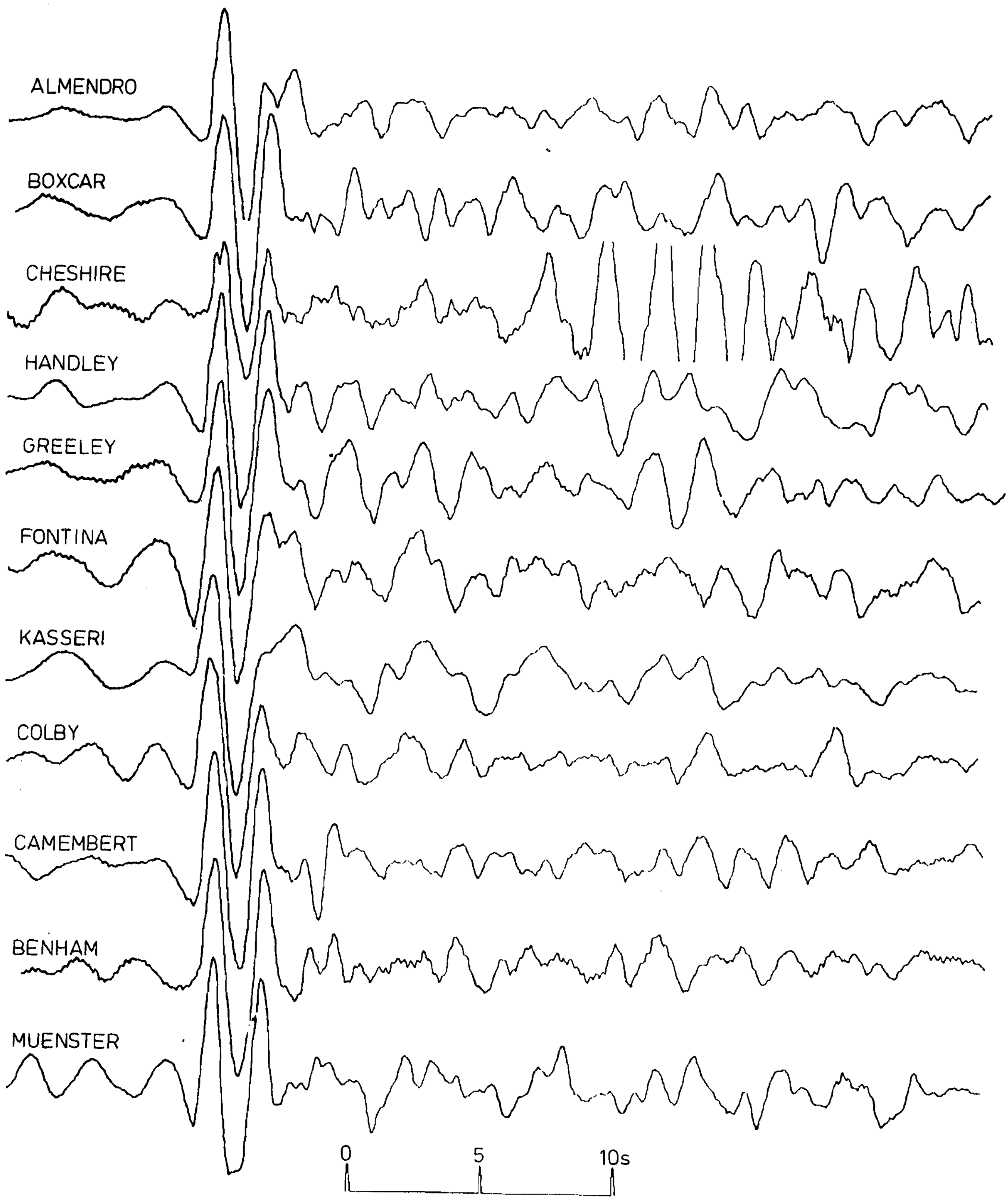

FIGURE 46. THE DECONVOLVED BB SEISMOGRAMS FOR THE PAHUTE MESA EXPLOSIONS ARRANGED IN ORDER OF DEPTH OF FIRING

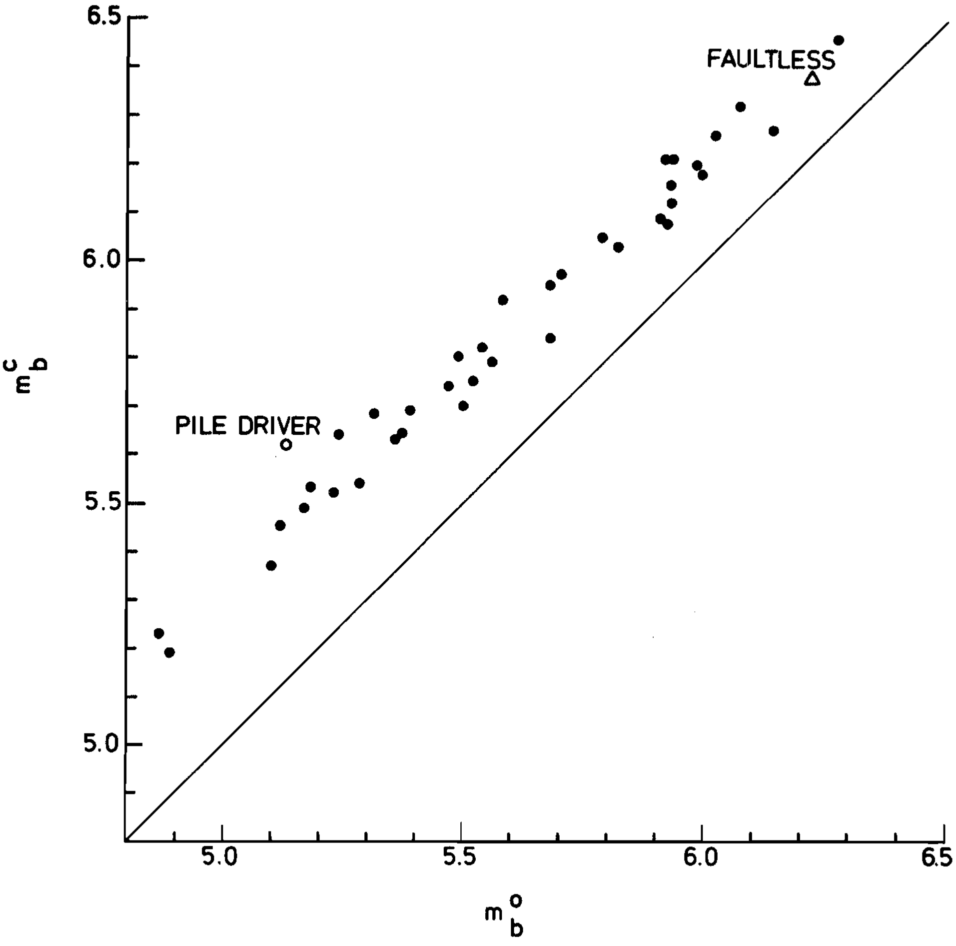

FIGURE 47. GRAPH OF m_b^c AGAINST m_b^o. m_b^c IS THE BODY WAVE MAGNITUDE COMPUTED FROM THE ESKDALEMUIR SP SEISMOGRAMS CORRECTED FOR ATTENUATION WITH $t^* = 0.2$ s. m_b^o IS THE BODY WAVE MAGNITUDE COMPUTED FROM THE OBSERVED SP SEISMOGRAMS (m_b^o AND m_b^c ARE LISTED IN TABLE 2)

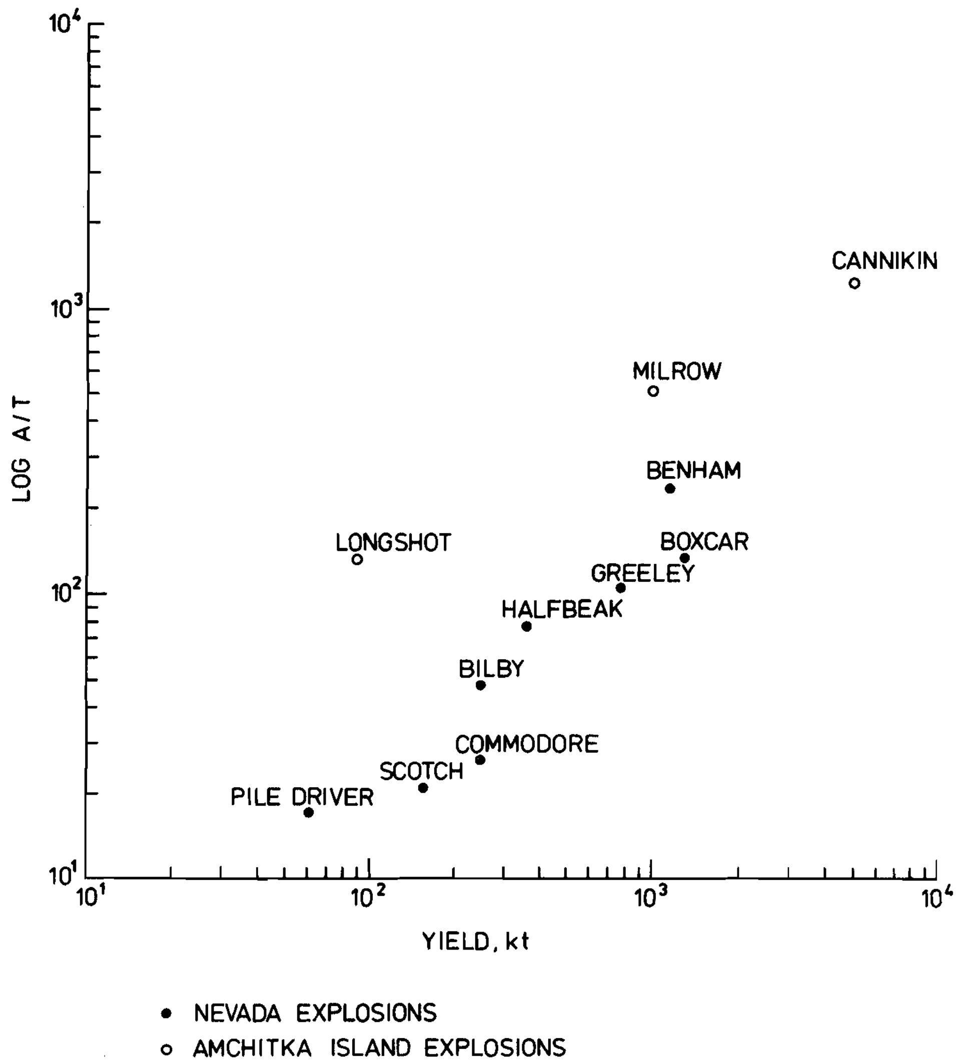

FIGURE 48. (a) PLOT OF $\psi^c(\infty)$ ESTIMATES AGAISNT YIELD FOR NEVADA EXPLOSIONS FOR WHICH YIELDS HAVE BEEN ANNOUNCED. $\psi^c(\infty)$ ESTIMATES FOR THE AMCHITKA ISLAND EXPLOSIONS ARE ALSO SHOWN.

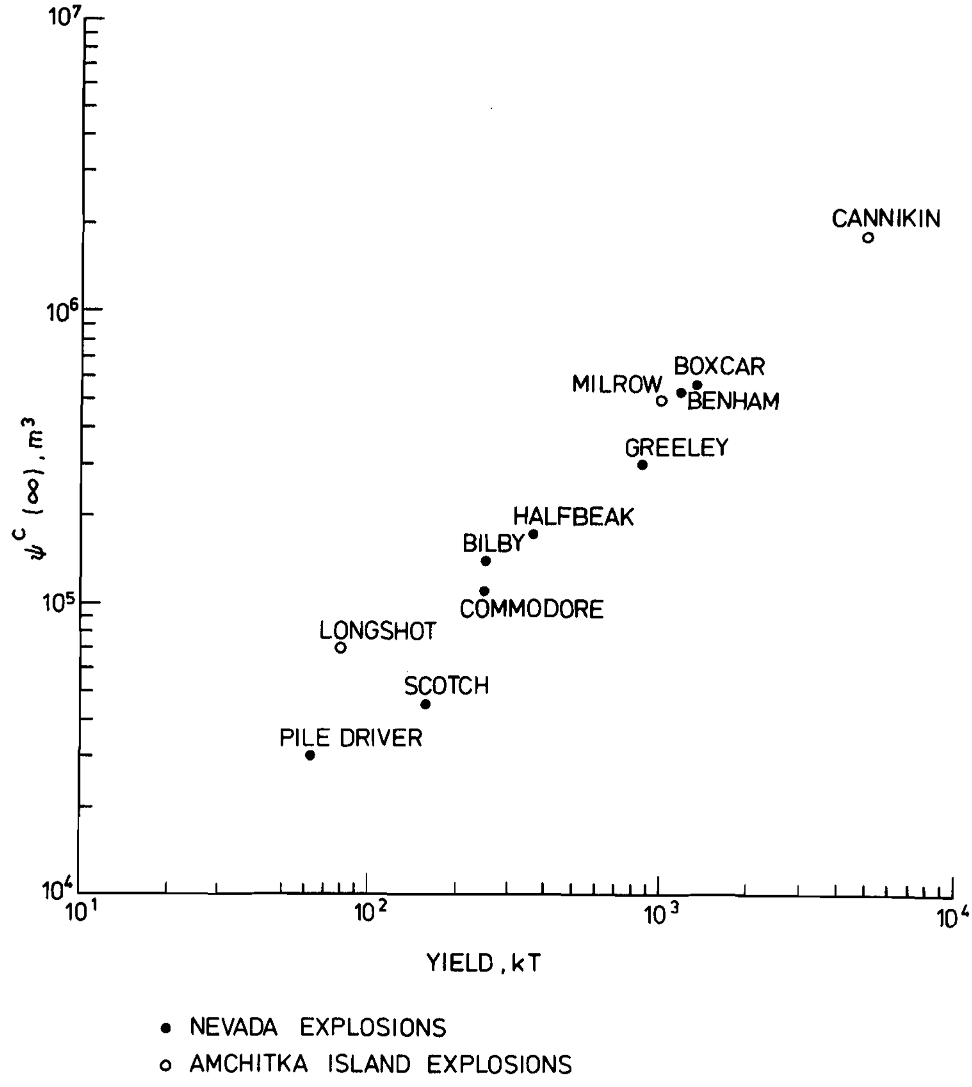

FIGURE 48. (b) PLOT OF LOG $^A/T$ AGAINST YIELD FOR NEVADA EXPLOSIONS FOR WHICH YIELDS HAVE BEEN ANNOUNCED. LOG $^A/T$ FOR THE AMCHITKA ISLAND EXPLOSIONS ARE ALSO SHOWN.

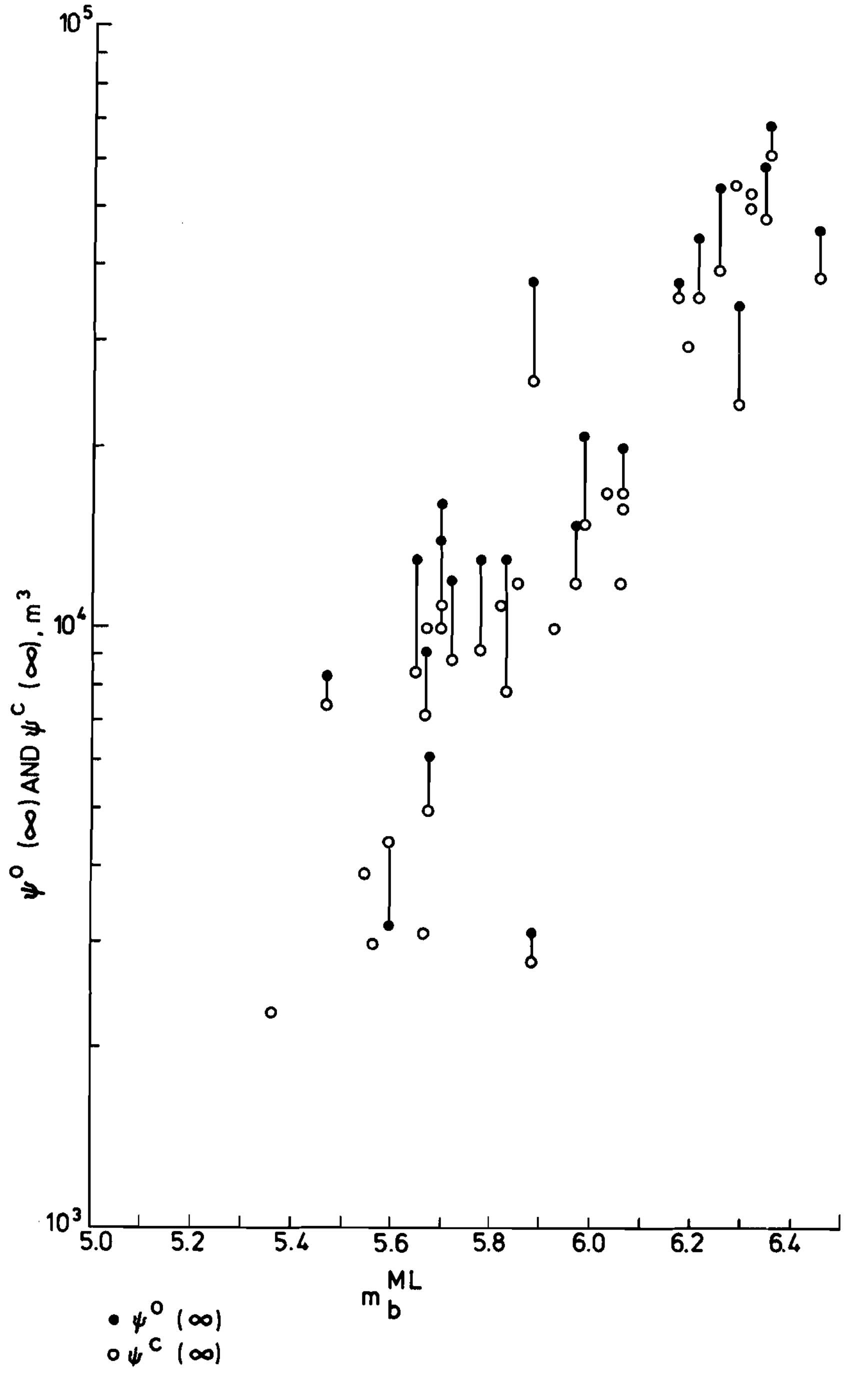

FIGURE 49. PLOT OF $\Psi(\infty)$ ESTIMATES PLOTTED AGAINST m_b^{ML}, THE MAXIMUM-LIKELIHOOD ESTIMATE OF THE BODY WAVE MAGNITUDE. (m_b^{ML} IS LISTED IN TABLE 2)

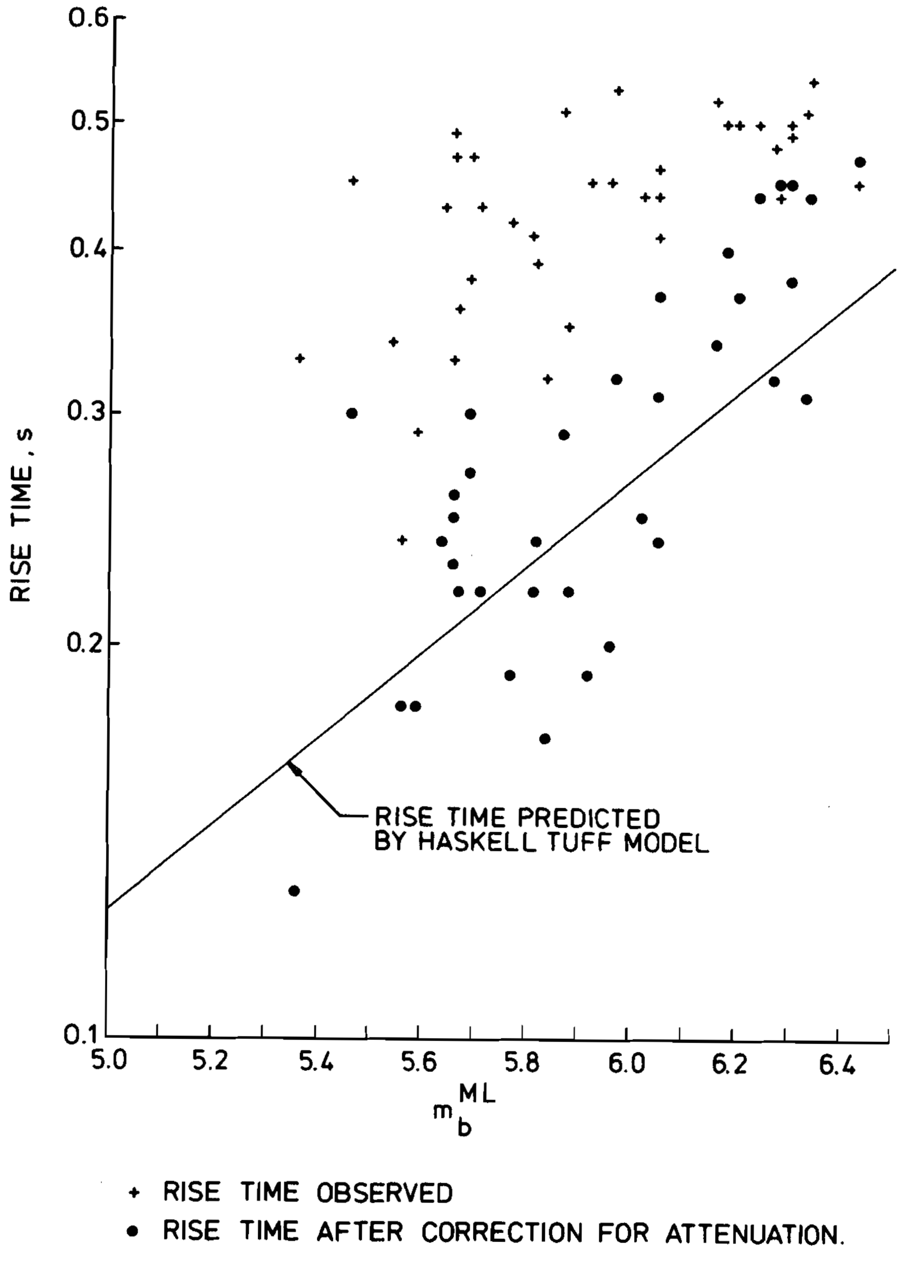

FIGURE 50. PLOT OF RISE TIMES AGAINST m_b^{ML} - THE MAXIMUM-LIKELIHOOD ESTIMATE OF BODY WAVE MAGNITUDES (m_b^{ML} IS LISTED IN TABLE 2)

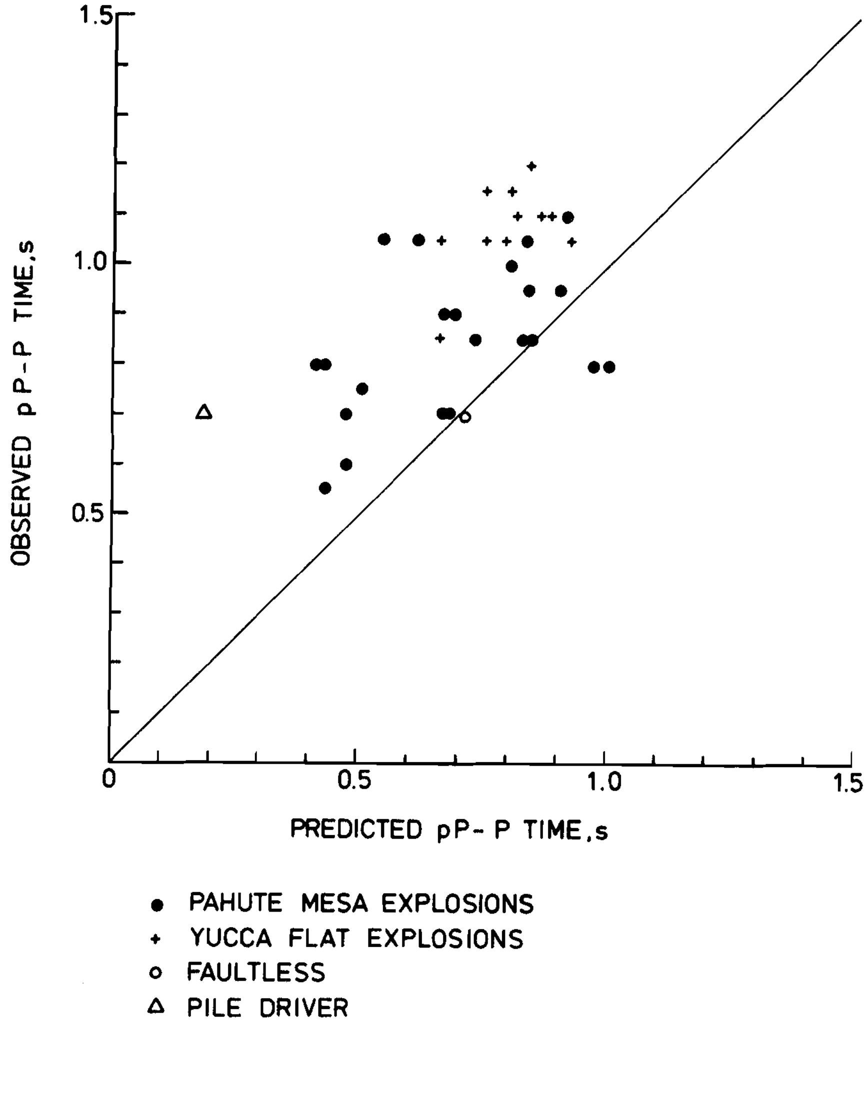

FIGURE 51. PLOT OF ESTIMATED pP-P TIME AGAINST PREDICTED TIME. (ESTIMATED AND PREDICTED TIMES ARE LISTED IN TABLE 2).

DOCUMENT CONTROL SHEET

Overall security classification of sheet ....Unclassified....

(As far as possible this sheet should contain only unclassified information. If it is necessary to enter classified information, the box concerned must be marked to indicate the classification eg (R), (C) or (S)).

1. DRIC Reference (if known)	**2. Originator's Reference**	**3. Agency Reference**	**4. Report Security Classification**
-	AWRE Report No. 010/86	-	UK Unlimited

5. Originator's Code (if known)	**6. Originator (Corporate Author) Name and Location**
-	Atomic Weapons Research Establishment, Aldermaston
5a. Sponsoring Agency's Code (if known)	**6a. Sponsoring Agency (Contract Authority) Name and Location**
-	-

7. Title
P Seismograms Recorded at Eskdalemuir, Scotland from Explosions in Nevada, USA.

7a. Title in Foreign Language (in the case of Translation)
-

7b. Presented at (for Conference Papers). Title, Place and Date of Conference
-

8. Author 1.Surname, Initials	**9a. Author 2**	**9b. Authors 3, 4 ....**	**10. Date**	**pp**	**ref**
Lyman N S	Douglas A	Marshall P D Young J B	November 86	84	24

11. Contract Number	**12. Period**	**13. Project**	**14. Other References**
-	-	-	-

15. Distribution Statement
See front cover

16. Descriptors (or Keywords) (TEST)
Seismic arrays
Proving grounds
Seismic waves
Seismographs
Seismology
Underground explosions

Abstract
The report presents the P seismograms recorded at the array station at Eskdalemuir, Scotland from 39 Nevada Test Site explosions. Five types of seismogram are shown for each explosion. Estimates are given of the body wave magnitudes and rise times of the initial P Pulse both before and after correction for attenuation. The advantages of deconvolved seismograms over SP P seismograms are demonstrated.